Title
Fracture Behavior of Advanced Structural Materials

Author
Lemberg, Joseph Aaron

Publication Date
2011

Peer reviewed|Thesis/dissertation

Fracture Behavior of Advanced Structural Materials

By

Joseph Aaron Lemberg

A dissertation submitted in partial satisfaction of the

requirements for the degree of

Doctor of Philosophy

in

Engineering – Materials Science and Engineering

in the

Graduate Division

of the

University of California, Berkeley

Committee in charge:

Professor Robert O. Ritchie, Chair

Professor Andrew Minor

Professor Thomas Devine

Professor Claudia Ostertag

Fall 2011

ABSTRACT

Fracture Behavior of Advanced Structural Materials

by

Joseph Aaron Lemberg

Doctor of Philosophy in Engineering – Materials Science and Engineering

University of California, Berkeley

Professor Robert O. Ritchie, Chair

Further development of ultra-high structural applications requires new materials that can withstand the extreme environments found in power-generation turbines. Highly refractory materials capable of high strength at temperatures in excess of 1100°C are either inherently brittle (Al_2O_3, Si_3N_4) or cannot survive at such temperatures in oxidizing atmospheres (Mo, Nb). Brittle materials may be toughened with the addition of a more ductile phase. Materials that do not form protective oxide layers can be alloyed with Si to form more protective silicate scales. A problem still remains as to how dissimilar materials like Al_2O_3 and Si_3N_4 can be joined. A brief discussion of the fracture behavior of ductile-phase-toughened nanocrystalline Al_2O_3 (Chapter 1) and functionally-graded material joints of Al_2O_3 and Si_3N_4 (Chapter 2) will precede an in-depth exploration of fracture in two Mo-Si-B intermetallic alloys (Chapters 3 & 4).

Chapter 1: Al_2O_3-based nanocomposites were fabricated and consolidated via spark plasma sintering. The influence on the fracture behavior of nanocrystalline Al_2O_3 of single-walled carbon nanotube (SWCNT) and Nb additions were examined by *in-situ* bend testing within a scanning electron microscope. The addition of 10 vol.% Nb to nanocrystalline Al_2O_3 provided substantial improvement of fracture toughness (6.1MPa√m)—almost three times that of unalloyed nanocrystalline Al_2O_3. Observation of cracks emanating from Vickers indents, as well as bend specimen fracture surfaces, reveal the operation of ductile phase toughening in the Nb–Al_2O_3 nanocomposites. Further addition of 5 vol.% SWCNTs to the 10 vol.% Nb–Al_2O_3 revealed a more porous structure and less impressive fracture toughness. The SWCNTs, initially added to form uncracked ligament bridges spanning the crack which would carry load and shield the crack tip from the full extent of the remotely-applied load, acted as

crack initiation sites and overwhelmed any toughness gains afforded by the ductile Nb grains.

Chapter 2: Nominally crack-free Al_2O_3- Si_3N_4 joints, comprised of 15 layers of gradually differing compositions of Al_2O_3/Si_3N_4, have been fabricated using SiAlON polytypoids as functionally graded materials (FGM) bonding layers for high-temperature applications. Using flexural strength tests conducted both at room and at elevated temperatures, the average fracture strength at room temperature was found to be 437 MPa; significantly, this value was unchanged at temperatures up to 1000°C. Scanning electron microscopy (SEM) observations of fracture surfaces indicated the absence of any glassy phase at the triple points. This result was quite contrary to the previously reported 20-layer Al_2O_3/Si_3N_4 FGM samples where three-point bend testing revealed severe strength degradation at high temperatures. Consequently, the joining of Al_2O_3 to Si_3N_4 using functional gradients of SiAlON polytypoids can markedly improve the suitability of these joints for high-temperature applications.

Chapters 3 & 4: New alloys based on borosilicides of molybdenum have been considered as potential replacements for current Ni-base superalloys, as they show promise as highly oxidation- and creep-resistant materials while still maintaining a moderate level of damage tolerance. Two alloys, each composed of Mo-3Si-1B (wt.%) with nominally similar fine-grained microstructures, have been developed utilizing markedly differing processing routes. Here, we study the influence of processing route on the fracture toughness of alloys containing ~55 vol.% ductile α-Mo and ~45 vol.% brittle intermetallics (Mo_3Si and Mo_5SiB_2 (T2)). The room-temperature toughness of these two alloys is significantly lower than that previously evaluated coarser-grained Mo-Si-B alloys with similar composition; however at 1300°C, the crack-initiation toughness of the fine- and coarse-grained alloys are nearly identical. At lower temperatures, the current finer-grained materials behave in a brittle manner as the smaller grains do not provide much impediment to crack extension; cracks can advance with minimal deflection thereby limiting any extrinsic toughening. Plastic constraint of ductile α-Mo grains from the hard intermetallic grains also serves to lower the toughness. At 1300°C, the increased ductility of α-Mo allows for significant plasticity; the correspondingly much larger contribution from intrinsic toughening results in significantly enhanced toughness, such that the finer grain morphology becomes less important in limiting crack-growth resistance. Optimization of these alloys is still required, however, to tailor their microstructures for the mutually-exclusive requirements of oxidation resistance, creep resistance and damage tolerance.

Table of Contents

Table of Figures

List of Tables

Acknowledgements

I would like to acknowledge several years of graduate student support from a National Defense Science and Engineering Graduate (NDSEG) Fellowship. I would also like to acknowledge the support and guidance of my research advisor, Dr. Robert Ritchie. Without his guidance, this work would never have come to fruition.

Chapter 1: This research was supported by a grant (# W911NF-04-1-0348) from the Army Research Office. Fabrication of the nanocrystalline Al_2O_3 beams and all indentation toughness testing was performed at the University of California, Davis by Katherine Thomson, Dongtao Jiang and Dr. Amiya Mukherjee. Thanks are due to Dr. Kurt Koester for his assistance and expertise with the *in-situ* bending experiments.

Chapter 2: This work was supported by National research foundation of Korea Grant funded by the Korean Government (2009-0087380). Fabrication of the Si_3N_4-Al_2O_3 joints and the room temperature fracture strength experiments were performed by Dr. Caroline Lee, D.G. Cho and J.Y. Roh at Hanyang University in Gyeonggi-do, the Republic of Korea. Thanks are also due to Sae-Hee Ryu and Jong-Ha Park from Samsung for their support. Funding for the high temperature fracture strength testing at Lawrence Berkeley National Laboratory was provided by the Director, Office of Science, Office of Basic Energy Sciences, Materials Sciences and Engineering Division, of the U.S. Department of Energy under Contract No. DE-AC02-05CH11231.

Chapters 3 & 4: This work was supported at the Lawrence Berkeley National Laboratory by the Director, Office of Science, Office of Basic Energy Research, Division of Materials Sciences and Engineering of the U.S. Department of Energy under contract No. DE-AC03-76SF00098. The processing of the Middlemas alloy was performed at Georgia Institute of Technology (by Drs. Michael Middlemas and Joe Cochran) and supported by the Office of Naval Research under contract no. N00014-08-1-0507. The Auger spectroscopy was performed at Karlsruhe Institute of Technology by Tobias Weingärtner. Thanks are due to Dr. Martin Heilmaier and Plansee of Reutte, Tirol, Austria, for supplying the ULTMAT alloy, and Dr. Craig Tewell and Miles Clift at Sandia National Laboratory, Livermore, CA, for help with additional Auger spectroscopy measurements. I would also like to thank Dr. Bernd Gludovatz at Lawrence Berkeley National Laboratory for helpful discussion and proofreading this section.

Dedication

First and foremost, my thanks go to my wife, Mary Turnipseed for supporting me through what must have seemed to be an interminable graduate career. I would also like to thank my family: parents Bill and Carole and sister Rebecca for their never-ending love and support, even when I moved 3,000 miles away. Lastly, I would like to thank my daughter Annabelle for providing love and distractions when I needed them. I would not have thought that my favorite birthday meal would be the hospital food I had the night after you were born. I love you, Banana.

Chapter 1 : *In-situ* bend testing of Nb-reinforced Al_2O_3 nanocomposites with and without the addition of single-walled carbon nanotubes

1.1 Introduction

Recently, controversy has grown over whether the addition of carbon nanotubes to nanocrystalline alumina (Al_2O_3) benefits the brittle ceramic's mechanical properties, specifically its fracture toughness.[1-4] However, it is clear that the addition of carbon nanotubes can add electrical and thermal conductivity to an otherwise insulating material. The carbon nanotubes that primarily reside at the grain boundaries of Al_2O_3 provide an effective matrix of conducting pathways.[5] If the fracture toughness can be improved, ceramic matrix composites hold great promise for use in structural and load bearing applications. Ceramic matrix composites possess superior chemical inertness, higher hardness, and lower densities than metals and their alloys. Furthermore, ceramic matrix composites with nanocrystalline matrices have superior strength and hardness properties over their microcrystalline counterparts. Unfortunately, the monolithic fracture toughness of the nanocrystalline ceramic matrices is significantly less than those in the microcrystalline regime. For example, microcrystalline Al_2O_3 has an intrinsic fracture toughness of ~3.3 MPa√m—as compared to about 2.3 MPa√m for nanocrystalline Al_2O_3.[6]

The addition of ductile phases such as metals to ceramic matrices has been proven to be an effective toughening mechanism.[7] The potential toughening benefits are twofold. The *intrinsic* (crack initiation) toughness of the material is increased as energy is dissipated from the propagating crack through two different phenomena: crack blunting at the ductile particle and/or absorption of energy through the deformation of the ductile phase. Both phenomena relieve the stress field around the crack tip. The *extrinsic* (crack growth) toughness of the material can be increased if uncracked ductile regions are left in the crack wake. These uncracked bridges can carry load and serve to shield the crack tip from the full extent of the remotely applied stress field. As will be elaborated upon in Chapters 3 & 4, the accumulation of uncracked ligaments with crack extension leads to a phenomenon known as rising R-curve behavior. A growing crack leaves an increasing number of uncracked ligaments, each which serves to carry some load and shield the crack tip from the remotely applied stress.

One of the motivations for adding carbon nanotubes to nanocrystalline Al_2O_3 is the potential for fracture toughness gains which arise from fiber bridging. Toughening is achieved when the fibers either shed load from the crack tip while remaining intact, debonding between the fiber and the matrix followed by fiber pullout, and/or fracture of the individual fibers followed by energy absorption through pullout of the broken fiber. Another toughening mechanism that is quite common in fiber-reinforced composites is crack deflection.[8] This occurs in situations in which the fiber is significantly stronger than the matrix and the fiber is favorably oriented as to allow for the crack propagation direction to proceed away from the axis of highest stress. Crack growth then becomes a competition between the direction of maximum driving force and the preferred microstructural pathway.[9] Commonly, the crack deflects to a less efficient cleavage plane directed by the longitudinal direction of the fiber. This scenario leads to increased fracture energy through increased surface area and lower driving forces due to the reduced resolved normal stresses at the crack tip.[10] As a result, the extrinsic toughness of these materials can be increased. However, for this mechanism to be truly effective, the fibers must be highly aligned. It should be noted that extrinsic mechanisms are the only way to increase the toughness of brittle materials, as materials such as Al_2O_3 lack the capability for significant plasticity (and thus intrinsic toughening).

Here, the mechanical properties of nanocrystalline Al_2O_3 reinforced with Nb, both with and without single-walled carbon nanotubes (SWCNTs), are examined. Mechanical bend testing conducted within an SEM, as well as *ex-situ* indentation testing, was used to reveal the extent of ductile phase toughening afforded by the addition of 10 vol.% Nb to nanocrystalline Al_2O_3. In addition, these same methods were used to study the failure mechanisms present when 5 vol.% SWCNTs was introduced to the Nb-Al_2O_3 system. The powder processing and spark plasma sintering processes used by Thomson, *et al.*[11] to manufacture samples for mechanical testing are summarized below.

1.2 Experimental procedures

1.2.1 Powder processing of Nb/Al_2O_3 and Nb/SWCNT/Al_2O_3 nanocomposite powders

As-received Al_2O_3 powder (α and γ phases, 45 nm, Baikowski International Corp.), the appropriate amount of 90 wt.% Nb (99.85% purity, 74 μm, Goodfellow)-10 wt.% Al (99.5% purity, 45 μm, Johnson Matthey Electronics) alloy to yield a 10vol.% Nb/Al_2O_3 composition, and 1 wt.% polyvinyl alcohol (PVA) were mixed by hand prior to high-energy ball milling (HEBM). Al was

added to reduce the surface oxide of the Nb particles and PVA was added to prevent severe powder agglomeration. This powder mixture was placed in a tungsten-carbide (WC) vial and HEBMed for 24 h using one WC ball. The composite powder was heat treated (at 350 °C for 3 h in vacuum) to remove the PVA before further processing was performed.

The Nb/Al_2O_3 composite powder was ultrasonicated for 15 minutes in 500 ml of ethanol. The slurry was then added to a polypropylene bottle with 280 g (33 vol.%) of zirconia ball media and wet-milled (130 rpm) for 24 hours. For the composites containing carbon nanotubes, the appropriate amount of SWCNTs (~90% purity, Carbon Nanotechnologies Inc., Texas) was weighed out. The SWCNTs were produced by the HiPco process and had diameters of 0.8–1.7 nm and length of up to 1μm. During final minutes of the previously mentioned wet milling, 8 ml of Nanosperse (an organic surfactant made by NanoLab) was stirred into 150 ml of deionized water. The SWCNTs were added to this solution and ultrasonicated for 5 minutes. The wet-milled slurry was slowly added to the dispersed carbon nanotube solution while ultrasonicating. The resulting mixture was added back into the polypropylene bottle and wet-milled for an additional 24 hours.

In both cases, the Nb/Al_2O_3 and $Nb/SWCNT/Al_2O_3$ slurries were taken off the wet-mill, ball media separated, sieved through a 150 μm mesh, and placed into medium sized glass beaker. A magnetic stir bar was added and the slurry was dried on a stirring hotplate. Once dry, the agglomerates were broken up with a mortar and pestle and sieved through 150 μm mesh. In the case of the $Nb/SWCNT/Al_2O_3$ powders, the dispersant was baked off at 450 °C for 4 hours.

1.2.2. Spark plasma sintering (SPS)

Consolidation was performed under vacuum in a Dr. Sinter 1050 SPS machine. The following processing parameters were used: 105 MPa of applied pressure, and "on" pulse of 12 cycles of 2 ms each and a "off" interval between pulses of 2 cycles, a maximum pulse settings of 5000A and 10V, and a pressure of 105MPa. An optical pyrometer was used to measure temperature and a heating rate of 125 K/min was used from room temperature to 600 °C. From 600 °C to the desired final set point (1200–1300 °C in this study), heating rates ranged from 150 K/min to 233 K/min. SPS consolidation yielded fully dense (98 + %TD) samples fit for microstructural characterization and mechanical testing. Density was determined via Archimedes method and consolidated samples had dimensions of 19 mm in diameter and 3 - 4 mm in thickness.

1.2.3. Mechanical testing and characterization

Samples were polished to 0.5μm surface finish and cut into beams having dimensions of 3 mm × 4 mm × 19 mm. The beam samples were pre-notched using a diamond saw, followed by an automated razor blade with 1 μm diamond paste to (*a*/*W*) ratio of 0.25–0.5 with a radius of curvature a the notch root of ~ 5 μm. The extreme brittleness of the material frustrated fatigue pre-cracking. As a result, the toughness values reported will be slightly elevated. Sample preparation procedures were made in general accordance with ASTM STP 1409, excepting for the use of a radiused micro-notch instead of a fatigue pre-crack.[12] The pre-notched beams were tested in three-point bending within a Hitachi S-4300SE/N scanning electron microscope using a Gatan Microtest 2000 test assembly. Crack propagation was observed under a 0.55 μm/s loading rate and the breaking load was recorded. Fracture surfaces were analyzed in a FEI XL-30 SFEG scanning electron microscope. For comparison, the fracture toughness of the nanocomposites was also calculated using the indentation method using a standard Tukon microhardness tester equipped with a diamond Vickers indenter and 2.28 kN load. A Buehler light microscope and ANALYSIS program was used to measure the cracks emitted from the indentations. While Vickers indentation fracture testing does not provide particularly accurate toughness data,[13] the tests are useful for studying crack propagation mechanisms in ceramic matrix composites.

1.3. Results and Discussion

To establish a baseline for comparison, a pure Al_2O_3 sample (slightly larger grain size of 1.4 μm) was fabricated and tested using identical procedures. In three-point bending, the fracture toughness was 3 MPa√m. The matrix grain size greatly decreases when Nb and/or SWCNTs are added, as frequently observed in ceramic matrix composites.[14, 15]

1.3.1 10 vol.% Nb-Al_2O_3 nanocomposites

Vickers indentation revealed a hardness of 22.9 GPa. Observation of the indents made in the 10–Al_2O_3 show that the Nb regions are effective at stopping propagating cracks. Crack blunting can be seen on the right corner of the indent in Fig. 1.1 where the crack intersects a Nb particle. This result is consistent with ductile phase toughening theory, as explained in more detail in Chapters 3 & 4. Clearly, HEBM produces a large size distribution of Nb particles—many much finer but others close to the as-received 74 μm particle size. Residual porosity is also apparent in some regions.

Although stable crack growth was not observed in the *in-situ* bend testing, the K_{IC} value obtained from the breaking load was 6.1 MPa√m. This initiation toughness value is likely somewhat inflated as a result of using a notched sample.[16] Analyses of the post-mortem fracture surfaces indicate two distinct failure modes of the Nb particles, both of which are apparent on the Nb particle in Figure 1.2. First, some of the Nb regions completely debonded from the brittle Al_2O_3 matrix. In some cases, imprints of the small Al_2O_3 grains can be seen in the region of debonding. Second, it is apparent that the majority of the Nb particles tended to fracture in a brittle manner as is typical at room temperature for body-centered cubic, high melting point metals such as Nb. Cleavage fracture and the presence of river lines indicate that the Nb particles ultimately failed without much plasticity. However, the resulting bend fracture toughness of 6.1 MPa√m indicates that the Nb regions did indeed absorb some energy from the propagating crack. Since this energy was not used to plastically deform the Nb, the crack propagation resistance is attributed to crack blunting and crack bridging. Such crack-tip shielding toughening mechanisms were also observed by other investigators in Nb/Nb_3Al composites.[17]

The justification for *in-situ* testing was to directly observe Nb particles bridging the crack wake as the crack extended. Stable crack growth was not observed in any of the notched samples, partially the result of no fatigue pre-crack. Therefore, a half-chevron-notched sample (the crack grows into an increasing wedge of material and thus a decreasing *K*-field situation) was produced and tested under identical conditions. Even in this extreme scenario, no stable crack growth was observed. Comparison of the last image taken before fast fracture and the image of the broken sample indicated that the crack that resulted in failure was on the order of a few microns. Thus, any R-curve behavior occurs within the first few microns of crack growth and could not be resolved in this experiment.

1.3.2. 10 vol.% Nb-5 vol.% SWCNT-Al_2O_3

Measurement of the cracks emanating from the indents made in 10 vol.% Nb-5 vol.% SWCNT-Al_2O_3 was much more difficult due to the increased porosity (~1.5 vol.%) and the dark color of the carbon nanotube agglomerates. Scanning electron microscopy (SEM) analysis revealed that the majority of carbon nanotube agglomerates were sub-micron with sizes ranging from a single nanotube bundle to larger agglomerates with widths of ~1μm. A representative indent is shown in Figure 1.3. Measurements of the indents revealed a lower hardness (19.3 GPa) than the 10 vol.% Nb-Al_2O_3 system.

It is possible that nanotube agglomerates were mistaken for a continuing crack. This is the disadvantage of using the indentation method to determine the fracture toughness of a composite and one of the reasons for discrepancies in literature. In comparison of Figs. 1.2 and 1.3, it appears that the Nb regions played less of a role in stopping the propagating cracks in the system in which the carbon nanotubes were introduced. The reason for this difference is unclear, though it is likely that the much smaller Nb particles near the indent in Fig. 1.3 were much less effective at retarding crack propagation.

In-situ bend testing revealed a fracture toughness of 3.3 MPa√m. Comparison of both the indentation and bend test fracture toughness of pure Al_2O_3 and the Nb-SWCNT-Al_2O_3 nanocomposite reveals little or no improvement of fracture toughness with the addition of both Nb and carbon nanotubes. In fact, the addition of carbon nanotubes appeared to negate any toughening by Nb seen in the Nb-Al_2O_3 system. The very brittle SWCNTs, which act as crack initiation sites, cause the decline in toughness. Of note is the increased porosity surrounding the carbon nanotube agglomerates. While this porosity would serve to lower the strength of the material, increased porosity could improve the intrinsic toughness of the material by blunting an advancing crack. A crack which penetrated a pore would need to reinitiate on the opposite side of the pore, thus raising the toughness.

The distribution of pores is closely tied to the distribution of carbon nanotubes. Consequently, a more uniform dispersion of carbon nanotubes would result in a more homogeneous distribution of pores. This porosity seems to be unavoidable because of the limitation of SPS temperature due to the presence of carbon nanotubes. Previous work revealed that the structure of carbon nanotubes begin to break down at SPS temperatures above 1150 °C.[18] Thus, in order to obtain as dense a specimen as possible, the hold time at 1200 °C was extended to 5 minutes, resulting in only a 98.5% dense sample.

The fracture surfaces of the 10 vol.% Nb-5 vol.% SWCNT-Al_2O_3 nanocomposites show a slightly larger grain size than the Nb-Al_2O_3 system due to the increase in SPS hold time (Figure 1.4). The carbon nanotubes are present in the Al_2O_3 grain boundaries as well as between the Nb particles and the Al_2O_3 matrix. Agglomerates of carbon nanotubes ranged from tens of nanometers to a few micrometers in width. As with the Nb-Al_2O_3 material, brittle failure of the Nb particles was also observed this system. The majority of cracks and pores were seen at the Al_2O_3-carbon nanotube interfaces and crack bridging was seen in only very few circumstances.

A number of factors limit the toughening capability of these nanocrystalline composites, especially in the case of those composites containing SWCNTs. Agglomerates of SWCNTs and the associated porosity are very detrimental. While small amounts of porosity are particularly not harmful on their own (as they serve as defacto crack blunting events), coupled with the easy crack reinitiation afforded by the brittle agglomerates of SWCNTs (which act as very brittle carbide inclusions), residual porosity within the material negates any increases in toughness. Were the SWCNTs aligned along the loading direction, and more finely dispersed, some degree of fiber bridging would be possible, but at present, SWCNTs limit the toughness of these composites.

Another factor limiting the toughness of these nanocomposites is plastic constraint at the crack tip. As will be further discussed in Chapters 3 & 4, a high volume fraction of hard Al_2O_3 limits the ability of the ductile Nb inclusions to plastically deform. As a result, crack blunting and especially ductile ligament bridging are severely limited.[19] In such situations, the toughness exhibited by the material can be considerably less than would be expected by a simple rule of mixtures calculation.

1.4 Summary

Al_2O_3-based nanocomposites containing Nb with and without carbon nanotubes were synthesized with advanced powder processing techniques and consolidated via spark plasma sintering. The fracture toughness was measured using both indentation and three-point bend techniques. Nanocrystalline Al_2O_3 has a very low fracture toughness of ~2.5 MPa√m. The largest degree of toughening occurred when 10 vol.% Nb was added to nanocrystalline Al_2O_3, raising the bend fracture toughness to 6.1 MPa√m. However, when 5 vol.% SWCNTs were added to this system the bend fracture toughness fell to 3.3 MPa√m. The decrease in fracture toughness is attributed to the increase in potential crack initiation sites in the carbon nanotube-containing nanocomposite. The 10 vol.% Nb-Al_2O_3 system holds promise for load bearing applications. On the other hand, the carbon nanotube-containing system would be ideal if a conductive ceramic without degraded fracture toughness is desired. *In-situ* bend testing was conducted with the premise of observing stable crack growth and obtaining the R-curve of toughened Al_2O_3 nanocomposites. Even in an extremely bias-notched sample, no stable crack growth was observed. Analysis of the last SEM image taken before catastrophic failure of the 10 vol.% Nb-Al_2O_3 bias-notched sample suggested that the crack that caused failure was on the order of a

few microns. Therefore, if any R-curve behavior exists, it is within the first few microns of crack growth.

1.5 References

1. S. I. Cha, K. T. Kim, K. H. Lee, C. B. Mo, and S. H. Hong: 'Strengthening and toughening of carbon nanotube reinforced alumina nanocomposite fabricated by molecular level mixing process', *Scripta Materialia*, 2005, **53**(7), 793-797.
2. R. W. Siegel, S. K. Chang, B. J. Ash, J. Stone, P. M. Ajayan, R. W. Doremus, and L. S. Schadler: 'Mechanical behavior of polymer and ceramic matrix nanocomposites', *Scripta Materialia*, 2001, **44**(8-9), 2061-2064.
3. X. Wang, N. P. Padture, and H. Tanaka: 'Contact-damage-resistant ceramic/single-wall carbon nanotubes and ceramic/graphite composites', *Nature Materials*, 2004, **3**(8), 539-544.
4. G. D. Zhan, J. D. Kuntz, J. L. Wan, and A. K. Mukherjee: 'Single-wall carbon nanotubes as attractive toughening agents in alumina-based nanocomposites', *Nature Materials*, 2003, **2**(1), 38-42.
5. G. D. Zhan and A. K. Mukherjee: 'Carbon nanotube reinforced alumina-based ceramics with novel mechanical, electrical, and thermal properties', *International Journal of Applied Ceramic Technology*, 2004, **1**(2), 161-171.
6. R. S. Mishra and A. K. Mukherjee: 'Processing of high hardness-high toughness alumina matrix nanocomposites', *Materials Science and Engineering A*, 2001, **301**(1), 97-101.
7. W. H. Tuan and R. J. Brook: 'The toughening of alumina with nickel inclusions', *Journal of the European Ceramic Society*, 1990, **6**(1), 31-37.
8. H. Suemasu, A. Kondo, K. Itatani, and A. Nozue: 'A probabilistic approach to the toughening mechanism in short-fiber-reinforced ceramic-matrix composites', *Composites Science and Technology*, 2001, **61**(2), 281-288.
9. R. O. Ritchie: 'Mechanisms of fatigue-crack propagation in ductile and brittle solids', *International Journal of Fracture*, 1999, **100**, 55-83.
10. J. B. Wachtman: 'Mechanical Properties of Ceramics'; 1996, New York City, John Wiley & Sons, Inc.
11. K. E. Thomson, D. Jiang, J. A. Lemberg, K. J. Koester, R. O. Ritchie, and A. K. Mukherjee: '*In-situ* bending of niobium-reinforced alumina nanocomposites with and without single-walled carbon nanotubes', *Materials Science and Engineering A*, 2008, **493**, 256-260.
12. J. J. Kubler: 'Fracture toughness of ceramics using the SEVNB method: From a preliminary study to a standard test method', in 'ASTM STP 1409', (eds. J. A. Salem, et al.), 2002, West Conshohocken, PA, ASTM.

13. J. J. Kruzic and R. O. Ritchie: 'Comments on "Measurement of the microstructural fracture toughness of cortical bone using indentation fracture"', *Journal of Biomechanics*, 2008, **41**(6), 1379-1380.
14. Z. Chen, T. Takeda, K. Ikeda, and T. Murakami: 'The influence of powder particle size on microstructural evolution of metal-ceramic composites', *Scripta Materialia*, 2000, **43**(12), 1103-1109.
15. C.-L. Fan and M. N. Rahaman: 'Factors controlling the sintering of ceramic particulate composites: I, conventional processing', *Journal of the American Ceramic Society*, 1992, **75**(8), 2056-2065.
16. R. O. Ritchie, R. H. Dauskardt, W. K. Yu, and A. M. Brendzel: 'Cyclic fatigue-crack propagation, stress-corrosion, and fracture-toughness behavior in pyrolytic carbon-coated graphite for prosthetic heart-valve applications', *Journal of Biomedical Materials Research*, 1990, **24**(2), 189-206.
17. C. Bencher, A. Sakaida, K. Rao, and R. Ritchie: 'Toughening mechanisms in ductile niobium-reinforced niobium aluminide (Nb/Nb_3Al) in situ composites', *Metallurgical and Materials Transactions A*, 1995, **26**(8), 2027-2033.
18. D. Jiang, K. Thomson, J. D. Kuntz, J. W. Ager, and A. K. Mukherjee: 'Effect of sintering temperature on a single-wall carbon nanotube-toughened alumina-based nanocomposite', *Scripta Materialia*, 2007, **56**(11), 959-962.
19. K. S. Chan and D. L. Davidson: 'Delineating brittle-phase embrittlement and ductile-phase toughening in Nb-based in-situ composites', *Metallurgical and Materials Transactions A*, 2001, **32**, 2717-2727.

1.6 Figures

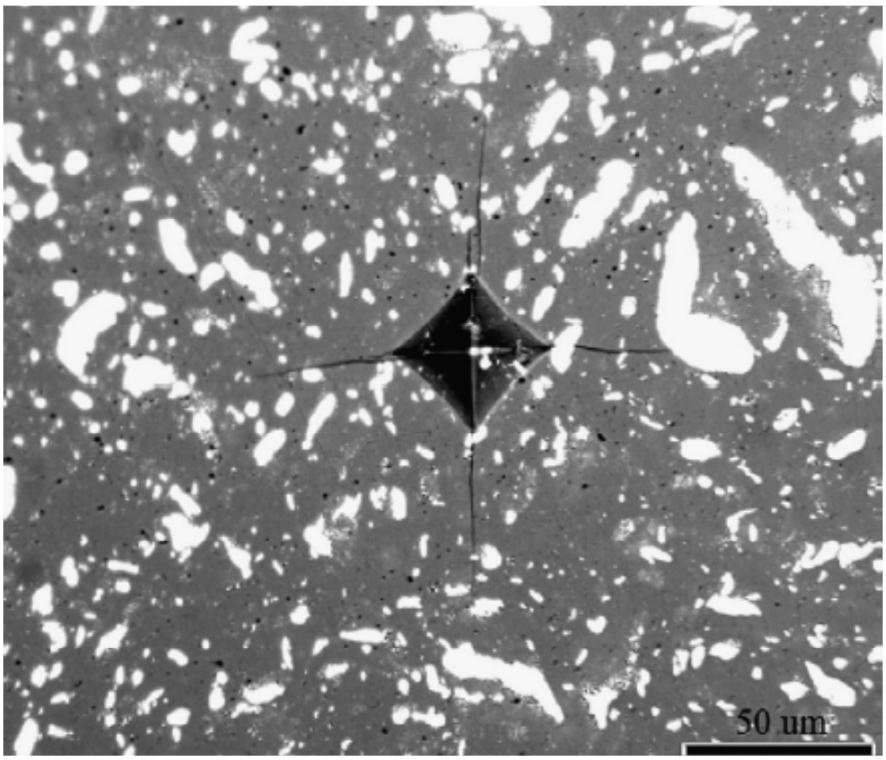

Fig. 1.1: Optical micrograph of an indent on 10 vol.% Nb-Al_2O_3 surface showing the effectiveness of the Nb regions (white) at stopping crack propagation. Two methods of toughening are visible: uncracked ligament bridging (*extrinsic* toughening mechanism) and crack blunting (*intrinsic* toughening mechanism).

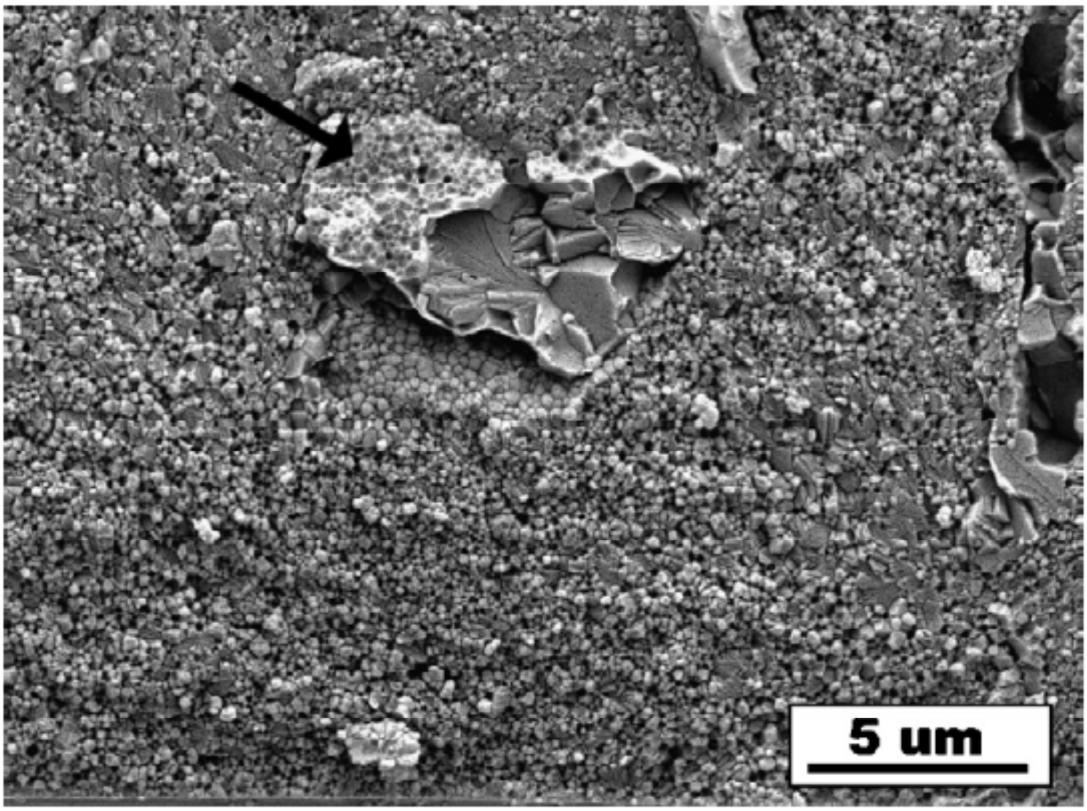

Fig. 1.2: SEM image of 10 vol.% Nb-Al_2O_3 fracture surface (Au-coated) displaying two modes of failure: particle debonding (arrow) and cleavage fracture. The crack grew from the bottom of the image towards the top. The initial notch can be seen at the very bottom of the image.

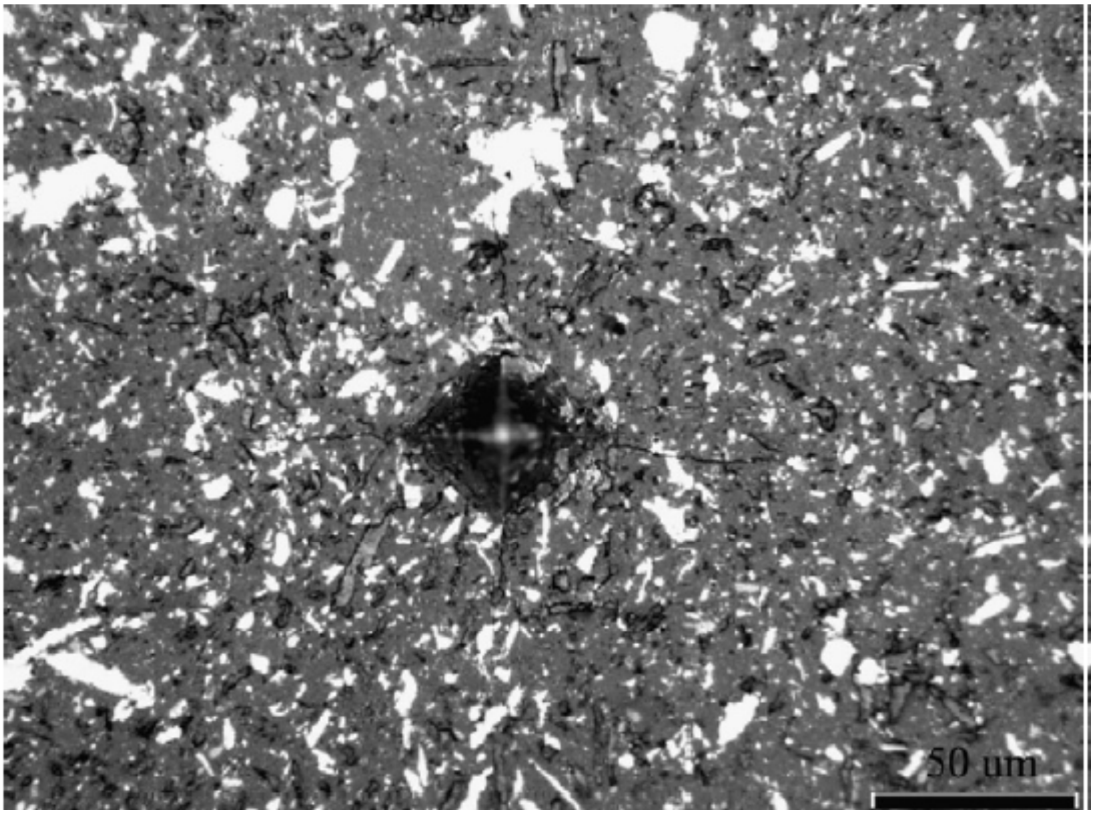

Fig. 1.3: Optical micrograph of an indent on 10 vol.% Nb-5 vol.%SWCNT-Al_2O_3 surface. Measurement of the cracks emanating from the indent was complicated by the presence of the black nanotube bundles. The much smaller Nb particles (white) in the region around this indent are much less effective at trapping the crack. The advancing crack is able to pass through or deflect around the small Nb grains without a large increase in energy. This behavior highlights the importance of microstructure for developing toughness in these materials.

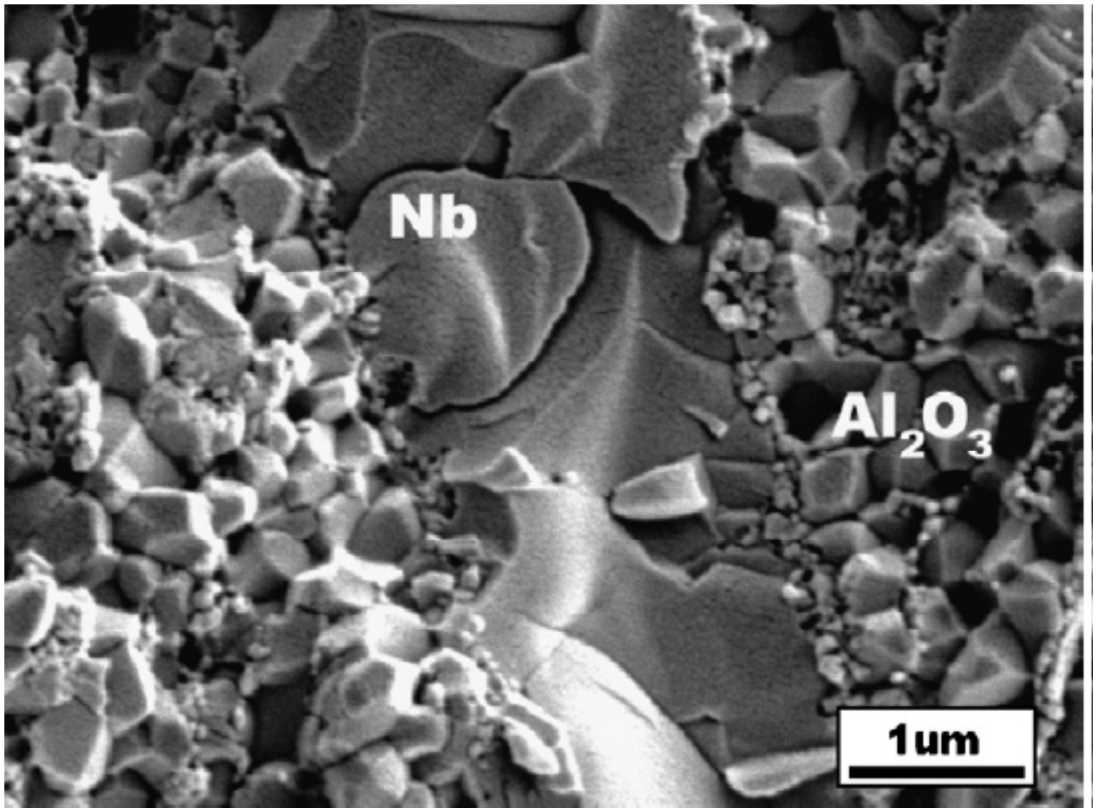

Fig. 1.4: SEM image of 10 vol.% Nb-5 vol.% SWCNT-Al_2O_3 fracture surface (Au-coated) revealing similar brittle failure of a Nb particle and carbon nanotubes (appear as small particles) at the Al_2O_3 grain boundaries.

Chapter 2 : Mechanical properties of Si_3N_4-Al_2O_3 functionally graded materials (FGM) joints with 15 layers for high-temperature applications

2.1 Introduction

Although there are numerous joining techniques, achieving sound bonds between dissimilar materials using the functionally graded materials (FGM) method is commonly used because it achieves a gradual compositional change from one type of joint element to the other, thereby avoiding a singularity at the interface. Functionally graded materials consist of a spatially-varying composite microstructure designed to optimize performance through a corresponding property distribution.[1] A graded interface can minimize the differences in properties from one material to another. Minimizing such property differences between two joining materials becomes especially pertinent for brittle materials where the tolerance for property mismatch is negligible. Since ceramic materials invariably display little or no plastic deformation, small differences in the coefficient of thermal expansion (CTE) can result in cracking during processing and premature failure of the joint. To mitigate this problem, FGM joining techniques can be used to create a quasi-continuous change in composition from one side of a joint to the opposite side, with an accompanying gradient of thermal expansion properties. Consequently, the use of such a graded junction, rather than an abruptly changing bond layer, presents a feasible method for the effective joining of dissimilar ceramics with widely differing CTEs.

To date, the concept has been successfully demonstrated with the SiAlON polytypoid functional gradient joining of Al_2O_3 and Si_3N_4, using 20 individual Al_2O_3/Si_3N_4 layers of gradually varying composition.[2] Across this composition gradient, a phase transformation takes place in the SiAlON polytypoids nearest to the Al_2O_3-rich area. A transformation from the 12H structure (a repeating unit of 12 hexagonally-packed layers) to the 15R structure (a repeating unit of 15 rhombohedrally-packed layers) serves to relieve lattice mismatch stresses. These polytypoids are physically and chemically compatible with both Si_3N_4 and Al_2O_3, and form in wurtzite-like structures.[3] Since metal–nitrogen bonding is in general more covalent than metal-oxygen, there is freedom to vary the covalent:ionic bonding ratios in a variety of structures.[4] The relationships between Si–Al–O–N condensed phases are represented by the quaternary phase diagram (Fig. 2.1); any point in the square diagram Si_3N_4-Al_4O_6-Al_4N_4-Si_3O_6 represents a

combination of 12^+ and 12^- valences where the components adopt their usual valance states (*i.e.* Si^{4+}, Al^{3+}, N^{3-} and O^{2-}). A polytypoid is defined as a faulted structure in which the fault periodicity depends on composition through the cation/anion ratio. Differing fault periodicities (and thus layer stacking sequences) lead to changes in the polytypoids' cation/anion ratios, and also result in different coefficients of thermal expansion.

Relieving the lattice mismatch has resulted in a macroscopically crack-free FGM.[2,5] The mechanical properties of these crack-free FGM joints have been tested at room and high temperature. As materials, ceramics are widely used for many applications that require high melting temperatures, high-temperature strength, good wear resistance, and chemical stability.[6] For structural applications, ceramics often display only minimal degradation in strength and fracture resistance at temperatures up to, and often above, 1000 °C. This behavior is in sharp contrast to most metallic structural materials, which invariably soften at higher temperatures. It is this retention of mechanical properties at elevated temperatures which identifies ceramics as preferred candidate materials for many structural applications, although their limited ductility and toughness at lower temperatures often frustrates their actual use.

Si_3N_4 ceramics have often been the preferred candidates for such structural applications owing to their high strength and particularly high toughness relative to most other ceramic materials. To join Si_3N_4 to other ceramics, specifically Al_2O_3, SiAlON polytypoidal functional gradients can be used since SiAlON polytypoids are physically and chemically compatible with both materials;[7] moreover, SiAlON polytypoids are attractive joining materials since they have CTE values between those for Si_3N_4 and Al_2O_3. It was the objective of the work presented here to use such FGM joining techniques to bond Si_3N_4 to Al_2O_3 and specifically to evaluate the strength of the corresponding dissimilar ceramic joints, both at room (25 °C) and elevated (1000 °C) temperatures.

The room and high-temperature strengths of FGM Al_2O_3/Si_3N_4 joints which have been optimized through thermodynamic simulation are compared with previously reported results for these two materials where the FGM joining techniques were not optimized. The ultimate aim is to discern whether such FGM bonding procedures can actually produce Al_2O_3/Si_3N_4 joints suitable for high-temperature structural applications, where high strength and moderate toughness are required.

2.2 Experimental Procedures

2.2.1 Material fabrication of optimized joint

The processing and characterization methods used to generate the layered FGM Al_2O_3/Si_3N_4joints were similar to those described in detail by Lee, *et al.*[5] A powder stacking method was used to produce 15 layers with varying Al_2O_3/Si_3N_4 composition and thickness, prior to hot pressing to sinter the multilayered FGM's. The optimal thickness of each layer was determined using simulation results.[8] 6 wt.% Y_2O_3 and 2 wt.% Al_2O_3 were added as sintering additives to aid in the sintering of Si_3N_4; 3 wt.% Y_2O_3 was used as a sintering additive for the polytypoid powders.[7] Si_3N_4 powders from Grand C&M with a particle size ranging from 0.3 to 0.5 μm were used, together with Al_2O_3 powders from Tamicron industries with a particle size ranging from 0.16 to 0.3 μm; 12H SiAlON polytypoid powders were obtained from Novel Technologies. Powders of each composition were mixed in a solvent of isopropanol then agitated using an ultrasonicator to prevent agglomeration. The powders were dried, sieved then stacked layer by layer in a cylindrical 25-mm diameter mold. The green body was pressed using a cold press to 38 MPa for 8 min. The green body was sintered using a hot press at 1700 °C for 2 h at a pressure of 38 MPa in flowing nitrogen gas to prevent decomposition of the Si_3N_4. A schematic of the experimental setup is shown in Fig. 2.2.

Simulations were performed to determine the optimum thickness of each layer necessary to minimize residual stresses and CTE mismatch across the FGM joint.[8] The composition and thickness of each layer is presented in Table 3.1. As a result of this optimization, the Si_3N_4–polytypoids–Al_2O_3 FGM could be processed crack free (Figure 2.3). Transmission electron microscopy (TEM) [JEM-3010, used voltage at 300 keV] was used to examine the microstructures, specifically to identify different phases at the various regions along the interface of the dissimilar ceramic joint.

2.2.2 Strength Characterization

Three-point bend tests were conducted at room (25 °C) and high temperatures (1000 °C) to determine the strength of the joint as a function of temperature. The test jig was designed specifically for testing unnotched rectangular cross-section beam specimens which were 3 mm × 4 mm × 10 mm and employed an upper loading span length of 8 mm (Figure 2.4). Loading was

performed in displacement control at constant displacement rates of 0.6 mm/min and 6 mm/min with an MTS 810 computed-controlled servo-hydraulic testing machine equipped with a Centorr Testorr furnace. Elevated temperature tests were conducted in an overpressure of gaseous argon to prevent degradation of the Si_3N_4. Samples were heated at 10 °C/min, and held at 1000 °C for 1 h to allow for thermal homogenization in the sample. Five separate samples were evaluated for each data set. All measured strength data were compared with those for the previous 20-layered FGM Al_2O_3/Si_3N_4 samples.[2] After testing, all fracture surfaces were observed using a scanning electron microscopy (SEM) [Hitachi S-4800, secondary electron mode].

2.3 Results and Discussion

2.3.1 The optimized crack-free joint

Figure 2.3 shows an optical image of the optimized crack-free joint with 15 layers. TEM images of this FGM sample are shown in Figure 2.5 (a) and (b). In the Si_3N_4-rich region, only Si_3N_4 and 12H polytypoid were found, whereas in the Al_2O_3-rich region, only Al_2O_3 and 15R polytypoid were found. The average size of a 12H polytypoid grain is approximately 0.3 μm in width and 1.3 μm in length. The average size of a Si_3N_4 grain is ~0.3 μm in width and ~1 μm in length, similar to that of the 12H polytypoid. In the Al_2O_3-rich areas, the average size of a 15R polytypoid grain is ~0.1–0.2 μm in width and 1 μm in length, as shown in Figure 2.5(b). These micrographs indicate that no undesirable reaction took place between the Si_3N_4, the Al_2O_3 or the polytypoids, which agrees with the behavior expected from the Si–Al–O–N quaternary phase diagram.[5] As shown in Fig. 2.1, 15R is the most chemically similar polytypoid to Al_2O_3 and the most similar polytypoid to Si_3N_4 is 12H. This trend in the polytypoid transformation from 12H to 15R as the ratio of cation to anion for those polytypoids decreases is exactly as predicted from the phase diagram (Fig. 2.1). The present approach can be applied to a wide range of ceramic systems including superconductors.[9] The center of the FGM sample where 12H/15R interface is located (A–B line from Figure 2.1), may in fact be mixtures of these polytypoids. Therefore, a sharp interface at the center of the FGM could not be resolved. Table 2.I shows the composition and layer thickness of sintered FGM joint.

Table 2.I: Composition and layer thickness for FGM joint

Layer Composition	Layer Thickness (μm)
100%Si_3N_4	1056

75%Si_3N_4/25%12H	956
50%Si_3N_4/50%12H	1000
25%Si_3N_4/75%12H	1111.1
20%Si_3N_4/80%12H	667
10%Al_2O_3/90%12H	440
20%Al_2O_3/80%12H	390
30%Al_2O_3/70%12H	330
40%Al_2O_3/60%12H	330
50%Al_2O_3/50%12H	330
60%Al_2O_3/40%12H	330
70%Al_2O_3/30%12H	330
80%Al_2O_3/20%12H	330
90%Al_2O_3/10%12H	440
100%Al_2O_3	440

2.3.2 Strength Characterization

The average measured strength in three-point bending at room temperature at a displacement rate of 0.6 mm/min was found to be 437 MPa; this was unchanged at 1000 °C for the same displacement rate (Table 2.II). This result is contrary to the findings of Lee, *et al.*[2] on their unoptimized 20-layer FGM joints where they found a 50% reduction in fracture strength at high temperatures caused by softening at glassy triple junctions (Table 2.III).

Table 2.II: Fracture strength, as a function of temperature, of optimized 15-layered FGM joint

Temperature	Strength (MPa)
Room temperature (25°C) (loading rate 0.6 mm/min)	437± 102

High temperature (1000°C) (loading rate 0.6 mm/min)	437 ± 50
High temperature (1000°C) (loading rate 6 mm/min)	380 ± 20

Table 2.III: Strength test results, as a function of temperature, for 20-layered FGM joint.[2]

Temperature	Strength (MPa)
Room temperature (25°C)	581± 60
High temperature (1000°C) (loading rate 0.6 mm/min)	262± 20

Fractures at both room- and elevated temperature occurred within the interface between 20% Si_3N_4/80% 12H polytypoid and 25% Si_3N_4/75% 12H polytypoid which is approximately in the middle of the sample. This result agrees with the modeling result where calculated residual stresses in each layer do not exceed the critical strength for failure but axial stress in the joint is the highest in the middle of the sample (Fig. 2.6). This explains how the 15-layered FGM sample came out macroscopically crack free but has the weakest point in the middle of the sample.

Although investigating the weakest part of an FGM joint is best accomplished using four-point bending, size limitations prevented the use of this technique. As a result, three-point bending was employed. Modeling of the joint was used to calculate the weakest points in the sample which were found to be at the interfaces near the center of the sample.[8] In this situation, three-point bending yields useful results for comparison of fracture strengths. It is apparent that the joints presented here maintained their strength at high temperatures, while the unoptimized joints tested previously did not.[2] However, it should be noted that the stresses in a three-point bending sample are highest directly below the single loading pin. Only in situations where the strength of an interface away from the center of the sample is severely deteriorated would a sample fracture at any interface outside the center of the sample. As a result, the data presented here should be used with caution, as it only truly compares the strengths of the interfaces between the 20% Si_3N_4/80% 12H polytypoid and 25% Si_3N_4/75% 12H polytypoid layers.

In the unoptimized, 20-layer joints studied previously, glassy phases were found at grain boundaries and triple points.[2] Softening of these glassy phases can increase the fracture strength of ceramic materials if grain pullout is a dominant failure mechanism; however, the temperature range at which these samples were tested is likely a region where grain pullout is not as dominant.[10] At intermediate temperatures (*i.e.* ~1000 °C for Si_3N_4), softened grain boundaries increase the incidence of transgranular fracture, lowering the fracture strength.[10] As the temperature increases further (1200-1400 °C), grain-boundary sliding again becomes an important strengthening mechanism. The flow stress of the softened grain-boundary glassy phase is low enough that grains can readily slide, leading to grain pullout and an increase in intergranular fracture. The strength increases achievable by this method have their limit, as continued softening of the grain-boundary phase at ultra-high temperatures contributes to rapid degradation of the strength of the joint. The same effect can be achieved by increasing the strain rate at a given temperature (Fig. 2.7).

Fig. 2.8 and Fig. 2.9 show a mixture of intergranular and transgranular fracture for failures at both room and high temperatures. In the present system (Fig. 2.8), no glassy phases or glassy triple junctions could be detected, consistent with the lack of any observed strength degradation at high temperatures. However, it should be noted that the room temperature fracture strength of the 20-layer joint was significantly higher, implying that grain pullout may be a dominant strengthening mechanism for these joints (Fig. 2.10). As expected, the fracture strength for the optimized, 15 layer joints at 1000 °C is lower for a faster displacement rate, but again the drop-off is much less dramatic than for the 20-layer FGM joint. This result also confirms that no softening of intergranular glassy phases took place for this optimized, crack-free joint. Therefore, the current optimized, 15-layer crack-free joint possessed a significantly reduced amount of glassy phases such that no strength degradation was observed at high temperature, in contrast to the severe degradation observed in 20-layered FGM as shown in Fig. 2.11. This difference might be due to the reduction in number of layers in the Si_3N_4-rich area. It was reported that Si_3N_4 sintered with Al_2O_3 + Y_2O_3 has grain boundaries with poor resistance to softening at 1000 °C.[11,12] In these liquid-phase sintered ceramics, grain boundaries and triple junctions often contain an amorphous phase which can soften, resulting in grain-boundary sliding and cavitation. In the current work, 5 layers were removed from the Si_3N_4-rich area to make a 15 layer, optimized joint. As removing 5 layers in the Si_3N_4-rich area reduces the amount of Al_2O_3 and Y_2O_3 used in the FGM fabrication, the strength degradation caused by these sintering additives was minimized. Indeed, previous high-resolution TEM studies by Vantendeloo, *et*

al.[13] on polytypoids in AlN–SiO_2 also showed no glassy phase on the grain boundaries between two polytypoid grains. It is clear that polytypoids allow for glass-free interfaces, which account for greater strength retention at high temperatures.

2.4 Conclusions

Macroscopic crack-free joining of heterogeneous Si_3N_4 and Al_2O_3 ceramics has been optimized to 15 layers by the use of SiAlON polytypoids as functionally graded materials (FGM), as defined by the phase diagram for the system Si_3N_4–Al_2O_3. Lattice mismatch was accommodated by transformation of the polytypoids to better match the properties of the material with which they were in contact. Moreover, this trend in the polytypoid transformation from 12H to 15R as the ratio of cations to anions decreases (*i.e.* the transition from Si_3N_4 to Al_2O_3), is exactly as predicted from the phase diagram (Fig. 2.1). The thickness and compositions of each layer of the Si_3N_4–Al_2O_3 joint were controlled to minimize residual stresses. This result was confirmed by three-dimensional modeling of the residual stresses caused by differential shrinkage, which showed that the calculated residual stresses did not exceed the critical strength for failure of the joint. The average fracture strength was found to be 437 MPa at room temperature, with no reduction at high temperatures (1000°C). A mixture of transgranular and intergranular fractures occurred at both temperatures within the 20%Si_3N_4/80%12H polytypoid and 25% Si_3N_4/75%12H polytypoid interfaces, which is approximately in the middle of the sample. The retention of the strength at 1000 °C showed that the optimized FGM joint had been successfully fabricated and that the FGM-based bonding could be considered as a suitable technique for joining dissimilar ceramic materials for high-temperature structural applications.

2.5 References

1. M. L. Pines and H. A. Bruck: 'Pressureless sintering of particle-reinforced metal-ceramic composites for functionally graded materials: Part I. Porosity reduction models', *Acta Materialia*, 2006, **54**(6), 1457-1465.
2. C. S. Lee, L. C. De Jonghe, and G. Thomas: 'Mechanical properties of polytypoidally joined Si_3N_4-Al_2O_3', *Acta Materialia*, 2001, **49**(18), 3767-3773.
3. C. B. Carter and M. G. Norton: 'Polymorphs, polytypes and polytypoids', in 'Ceramic Materials: Science and Engineering', 96-98; 2007, New York, NY, Springer Science & Business Media.
4. K. H. Jack: 'Sialons', *Materials Research Bulletin*, 1978, **13**(12), 1327-1333.

5. C. S. Lee, X. F. Zhang, and G. Thomas: 'Novel joining of dissimilar ceramics in the Si_3N_4-Al_2O_3 system using polytypoid functional gradients', *Acta Materialia*, 2001, **49**(18), 3775-3780.
6. J. Lu, L. Gao, J. Sun, L. Gui, and J. Guo: 'Effect of nickel content on the sintering behavior, mechanical and dielectric properties of Al_2O_3/Ni composites from coated powders', *Materials Science and Engineering A*, 2000, **293**(1-2), 223-228.
7. H. X. Li, W. Y. Sun, and D. S. Yan: 'Mechanical properties of hot-pressed 12H ceramics', *Journal of the European Ceramic Society*, 1995, **15**(7), 697-701.
8. S. H. Ryu, J. H. Park, C. S. Lee, J. C. Lee, S. H. Ahn, J. H. Chae, and D. H. Riu: 'Optimization of crack-free polytypoidally joined Si_3N_4-Al_2O_3 functionally graded materials (FGM) using 3-dimensional modeling', *Advanced Material Research*, 2008, **47-50**, 494-498.
9. R. Ramesh, G. Thomas, S. Green, C. Jiang, Y. Mei, M. L. Rudee, and H. L. Luo: 'Polytypoid structure of Pb-modified Bi-Ca-Sr-Cu-O superconductor', *Physical Review B*, 1988, **38**(10), 7070.
10. I. W. Chen, S.-Y. Liu, and D. Jacobs: 'Effects of temperature, rate, and cyclic loading on the strength and toughness of monolithic ceramics', *Acta Metallurgica Et Materialia*, 1995, **43**(4), 1439-1446.
11. M. K. Cinibulk, G. Thomas, and S. M. Johnson: 'Grain boundary phase crystallization and strength of silicon nitride sintered with a Y-SiAlON glass', *Journal of the American Ceramic Society*, 1990, **73**(6), 1606-1612.
12. G. Thomas: 'Designing for improved high temperature strength, creep, oxidation, and fatigue resistance in Si3N4′, Proceedings of the Conference on Critical Issues in the Development of High Temperature Structural Materials, 1993, TMS, 349-364.
13. G. Vantendeloo, K. T. Faber, and G. Thomas: 'Characterization of AlN ceramics containing long-period polytypes', *Journal of Materials Science*, 1983, **18**(2), 525-532.
14. K. H. Jack: 'Sialon ceramics: Retrospect and prospects', *Mater. Res. Soc. Symp. Proc.*, 1993, **287**.

2.6 Figures

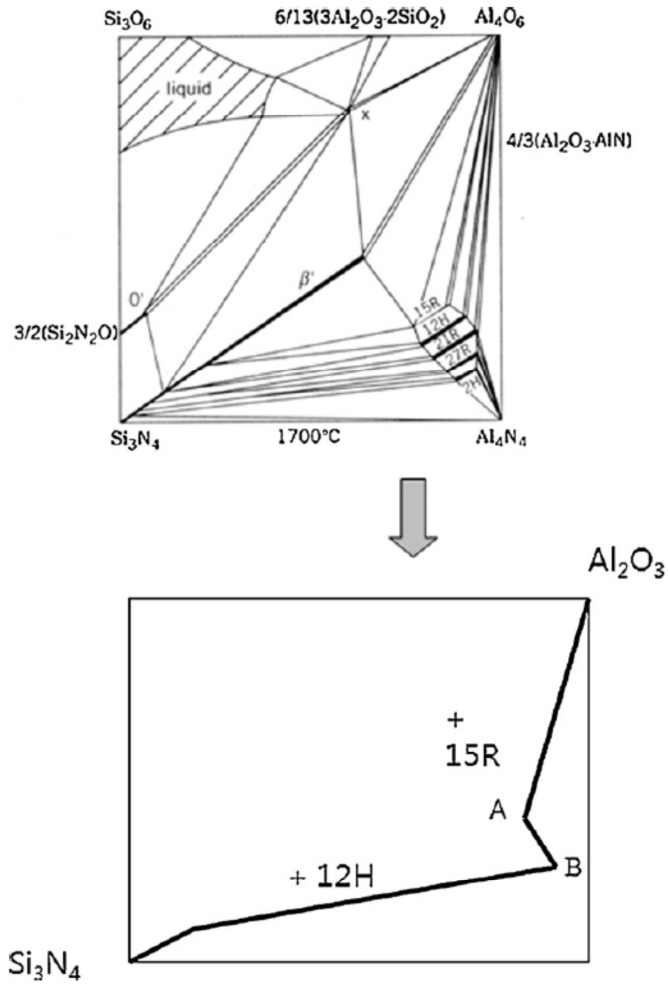

Fig. 2.1: The Si-Al-O-N system (1700°C).[14] The diagram below the quaternary phase diagram shows an equilibrium line path of Si_3N_4-12H-15R-Al_2O_3. A-B line refers to the 12H/15R "interface" at the center of the FGM.

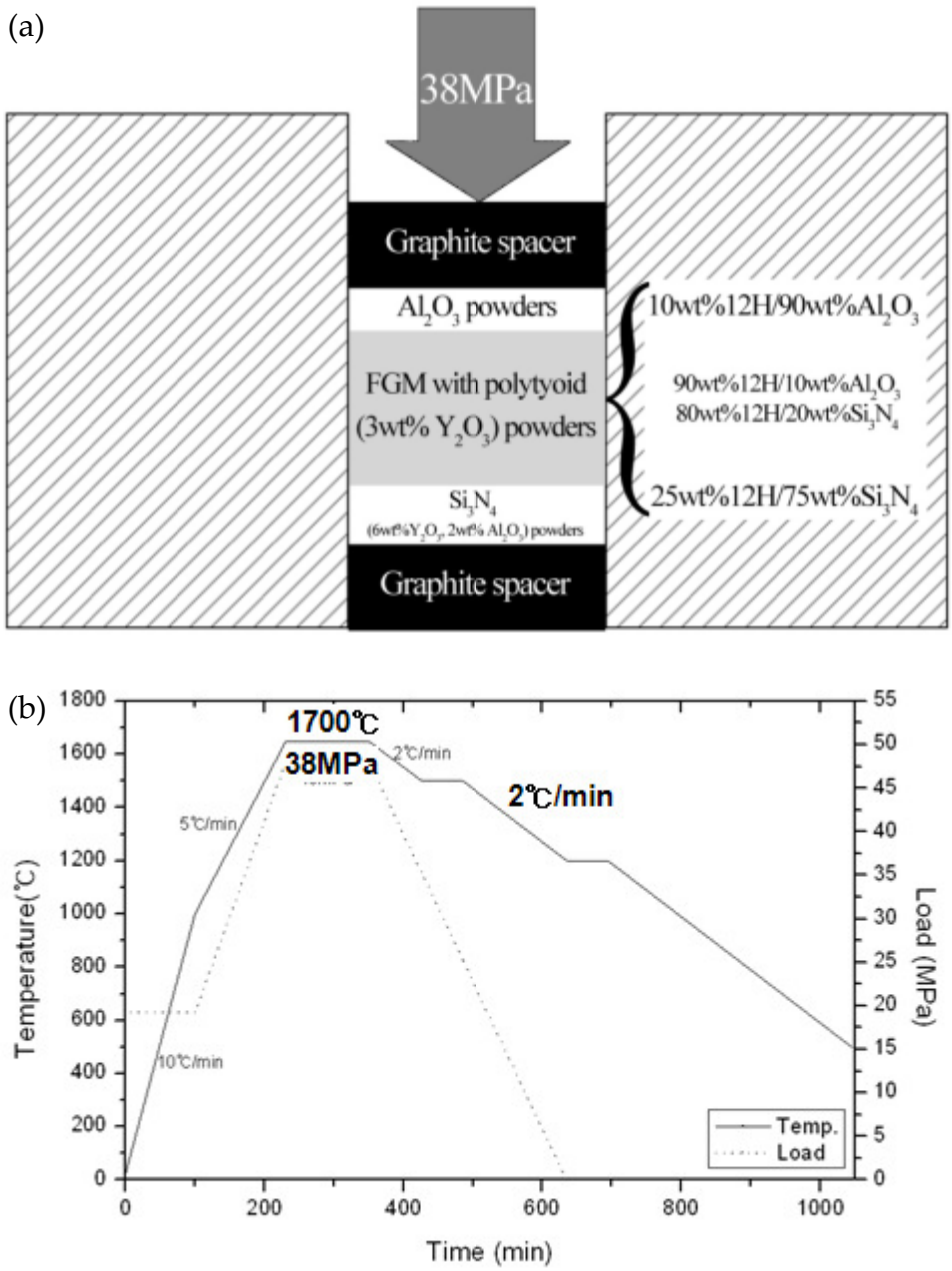

Fig. 2.2: (a) Experimental setup used to fabricate the crack-free joints using hot pressing. (b) Temperature and loading cycle used in such hot pressing procedures.

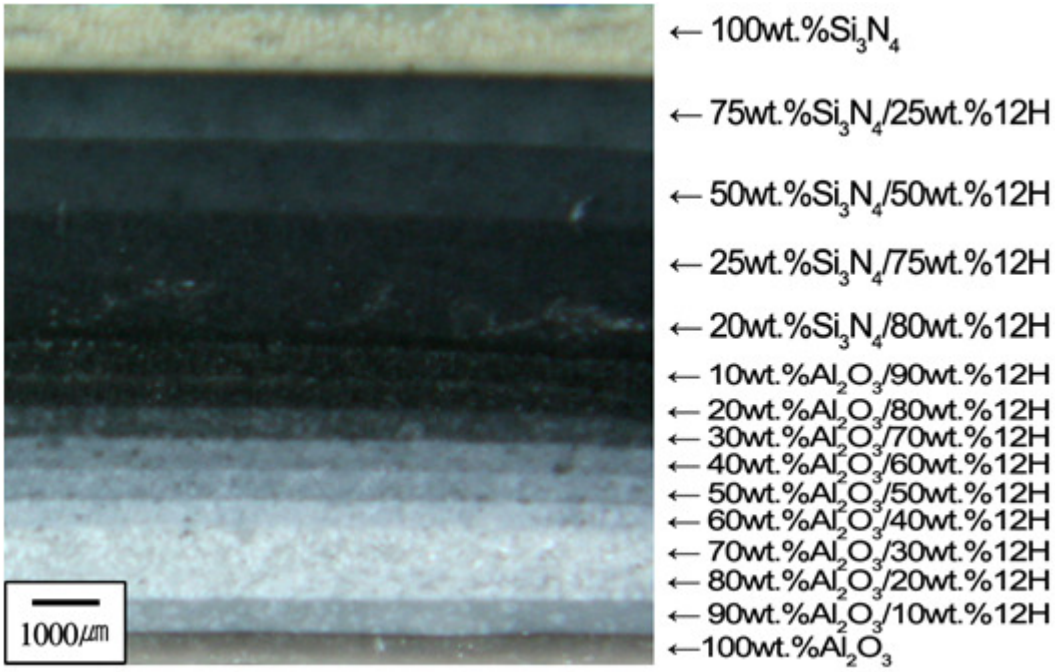

Fig. 2.3: Optical microscopy image of the crack-free FGM structure. The layer thicknesses are given in Table 2.I

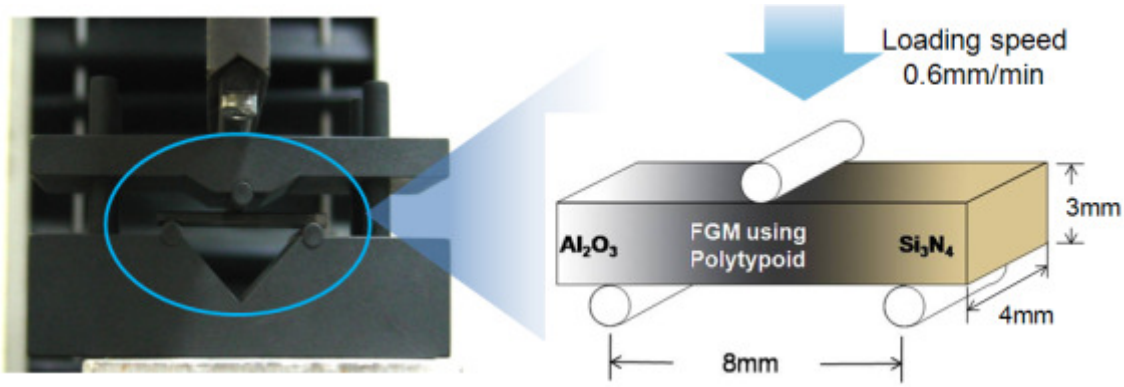

Fig. 2.4: Sample position and test jig geometry used for three-point bend testing. Tests at room temperature were performed at a displacement rate of 0.6 mm/min, while tests at 1000°C were performed both at 0.6 mm/min and 6 mm/min.

(a) (b)

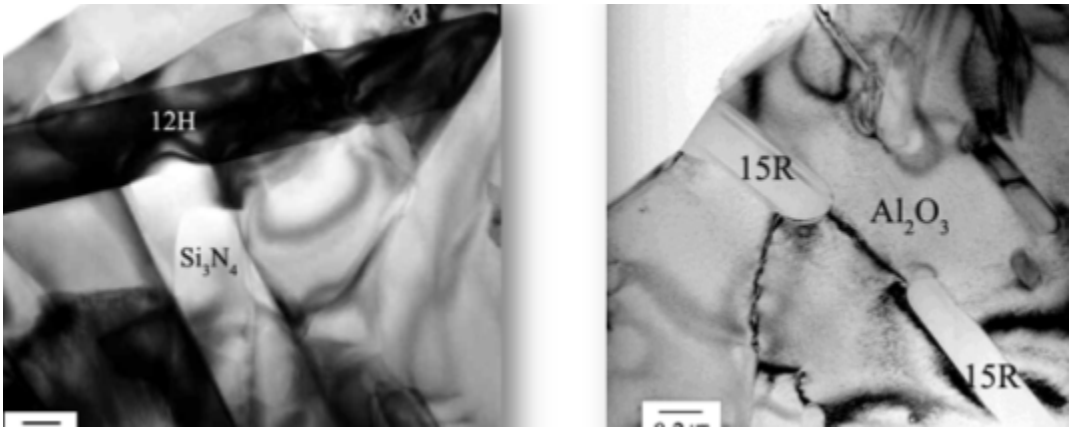

Fig. 2.5: (a) TEM image of the microstructure in the Si_3N_4-rich side of the FGM joint. Only the Si_3N_4 and 12H phases were detected. (b) TEM image of the microstructure in the Al_2O_3-rich side of the FGM joint. Only Al_2O_3 and 15R phases were detected.

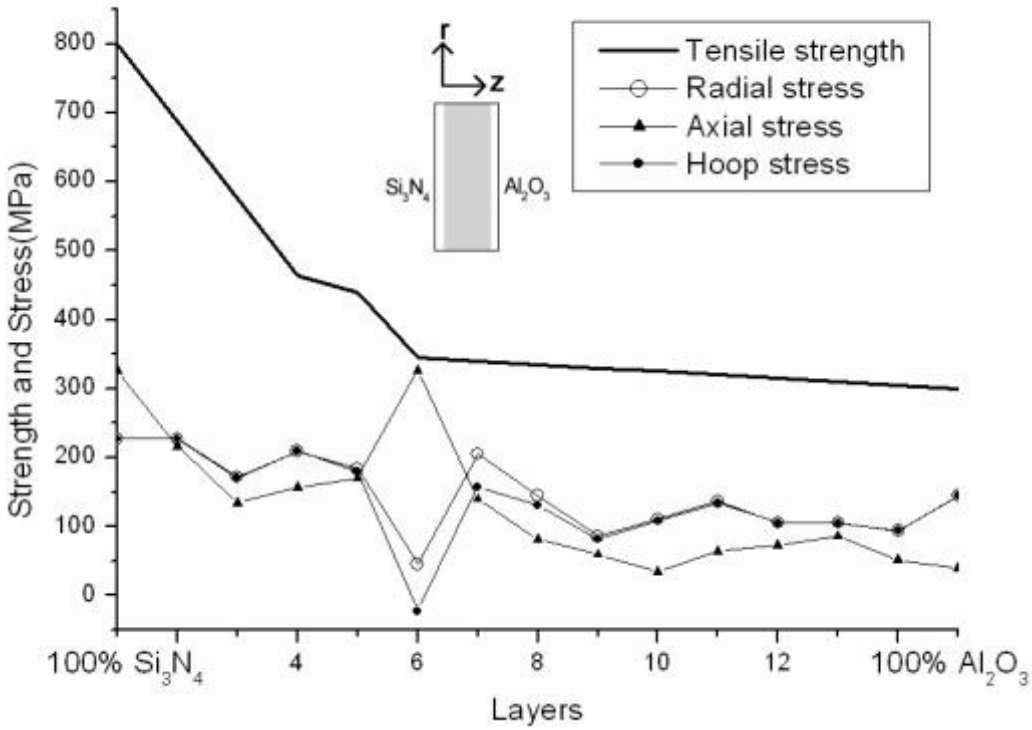

Fig. 2.6: Comparison of the computed radial, axial and hoop stresses with critical failure strength for crack-free FGM sample calculated by the numerical analysis method.

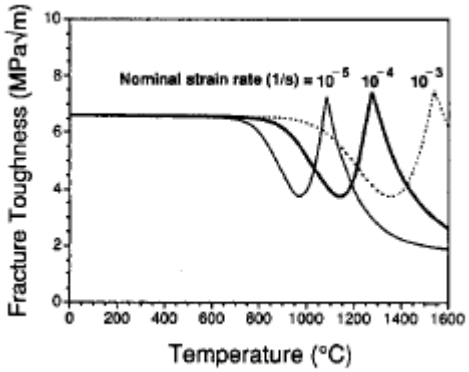

Fig. 2.7: Fracture toughness of Si_3N_4 as a function of temperature and strain rate. Grain pullout is a dominant strengthening mechanism at low and high (1200-1400°C), but softening of glassy grain boundaries leads to a decrease in toughness. Though the data presented measures toughness, an analogous argument can be made for the effects of temperature and strain rate on strength. After Chen, *et al.*[10]

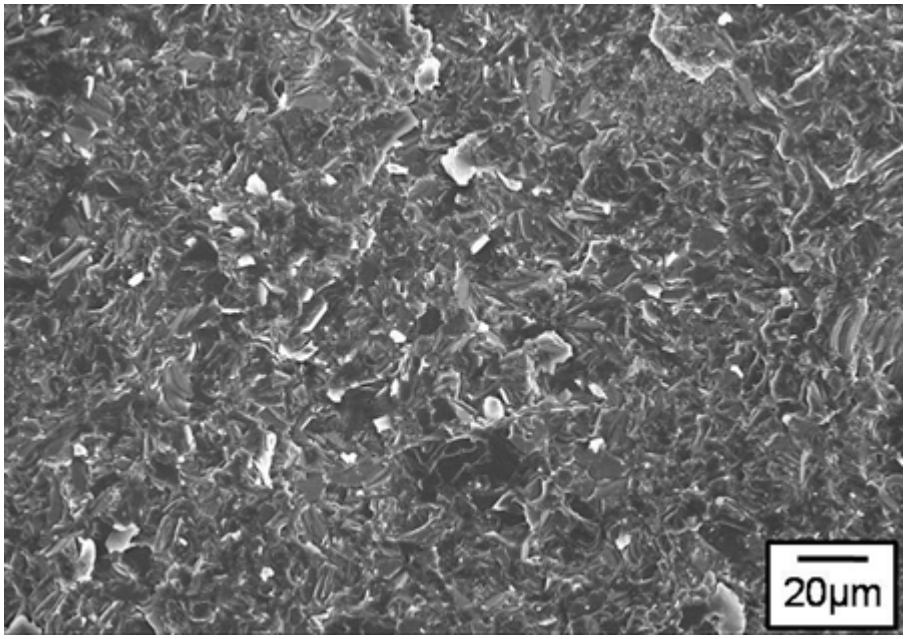

Fig. 2.8: SEM image of room temperature fracture surface of a 15-layered FGM sample.

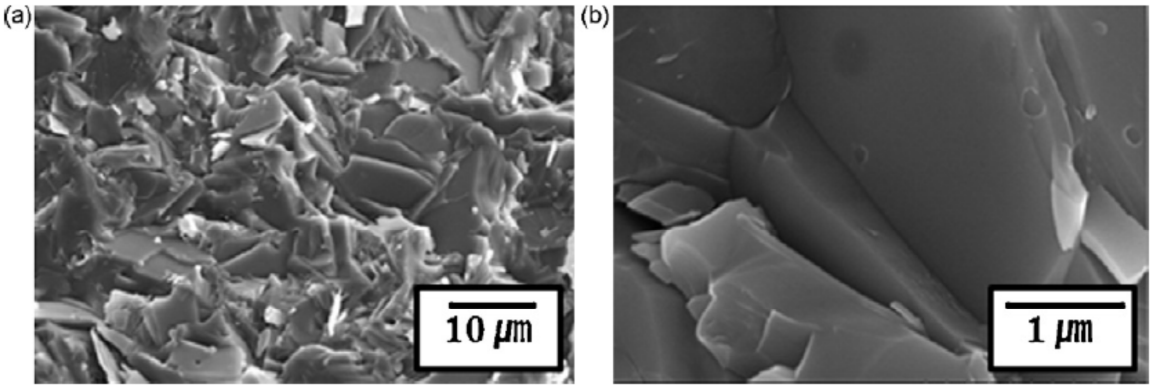

Fig. 2.9: (a) SEM image of the fracture surface of a 15-layered FGM sample tested at a temperature of 1000°C; (b) SEM image at the grain boundary used to detect the presence, if any, of any deformed intergranular phases. The image shows no presence of glassy phase at the boundary.

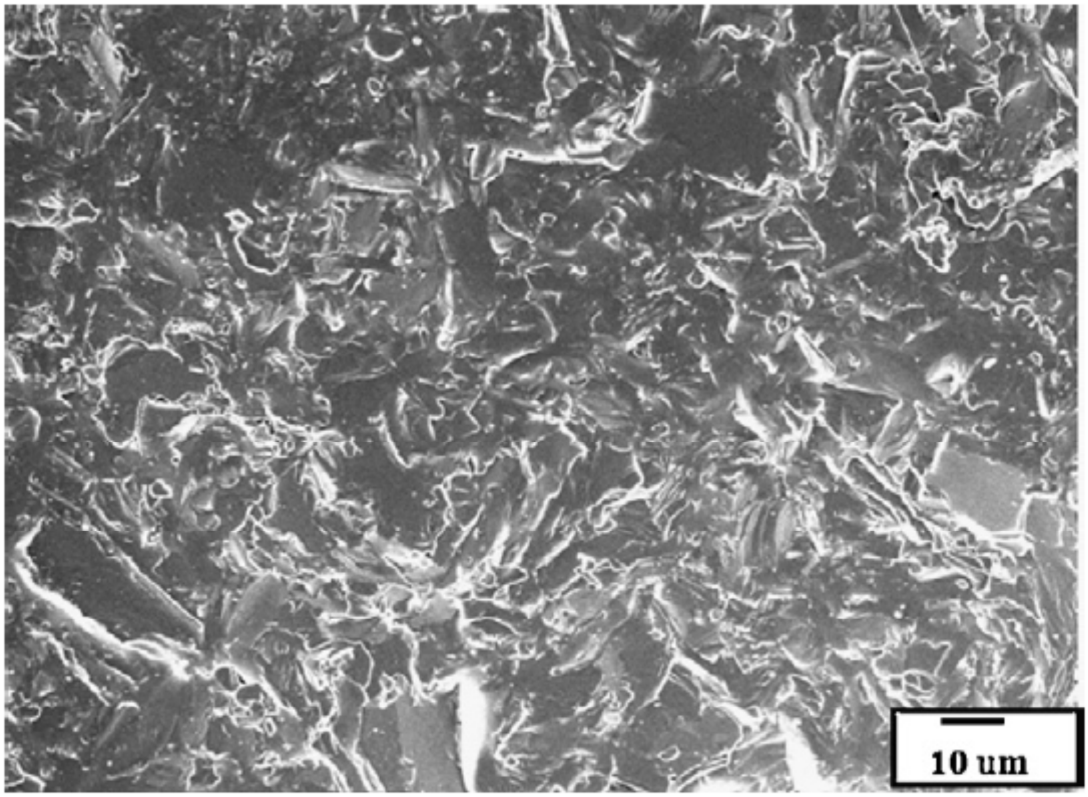

Fig. 2.10: SEM image of the room temperature fracture surface of an unoptimized 20 layer FGM structure.[2]

Chapter 3 : Literature Review for Mo-Si-B Ultra-high Temperature Alloys

3.1 Introduction

The quest for new, ultrahigh temperature structural materials is principally driven by the ever present need to improve the efficiency of aerospace and power-generation gas-turbine engines by operating at higher temperatures. Currently, turbine blades made from single-crystal nickel-base superalloys can function at temperatures nearing 1150°C, *i.e.*, close to 90% of their melting points.[1] Using complex cooling systems and thermal barrier coatings, these materials can exist in the hottest regions of a turbine engine where temperatures can approach 1500°C. However, the necessity for coatings and forced-air cooling greatly reduces the efficiency gained from operating at the higher temperatures, as shown in Fig. 3.1. To combat growing inefficiency losses, a preferred solution is the development of new ultrahigh temperature structural materials; one such class of materials which shows potential in this regard is based on the silicides of refractory metals, in particular involving the Mo-Si-B system. A number of reviews have been published regarding Mo-Si-B alloys since the early 1990s,[1-12] but many of these works either focused solely on one alloy system[3, 4, 9-11] or on one property of the alloys.[8] The only truly comprehensive review of the research on Mo-Si-B alloys was published in 2007 by Perepezko, *et al.*,[2] but that review does not contain information about the cutting-edge processing techniques which have been developed since its publication.

Here, we will review the development of Mo-Si-B alloys from the initial work of Nowotny, *et al.*[13] who developed the first phase diagram for the Mo-Si-B ternary system, to the most recent work[14, 15] studying ultra-fine grained Mo-3Si-1B alloys. We will highlight the processing methods used to produce Mo-Si-B alloys, as well as their oxidation and mechanical response. We will focus on alloys in the α-Mo-Mo_3Si-Mo_5SiB_2 and Mo_3Si-Mo_5Si_3-Mo_5SiB_2 phase regimes, but other systems will be discussed. We will undertake a brief discussion of the thermodynamics and phase stability of this system, but Perepezko, *et al.*[2] provide an excellent review of the research in this area and readers are directed to that work for a more in-depth discussion.

3.1.1. Single Phase Properties

Before undertaking a study of the behavior of multi-phase Mo-Si-B alloys, we will review the properties of individual phases within the Mo-Si-B system. Unless otherwise noted, all quantities are expressed as weight per cent. Fig. 3.2 shows the Mo-rich portion of the 1600°C isotherm of the Mo-Si-B phase diagram, as developed by

Nowotny, *et al.*[13] and later refined by Nunes, *et al.*[16] We will focus on the properties of α-Mo, Mo_3Si, Mo_5Si_3 (T1) and Mo_5SiB_2 (T2).

3.1.1.1 Molybdenum and α-Mo solid solutions

Pure molybdenum cannot be used in oxidative environments above ~ 500°C as a result of the rapid formation and volatilization of MoO_3.[17] Thus it is necessary to limit the α-Mo content for the best oxidation performance. As will be elaborated upon Section 5.2, α-Mo is required for any measure of damage tolerance, as the intermetallic phases are inherently brittle[a]. One strategy to limit the amount of α-Mo is to improve the room temperature ductility of α-Mo. In that way, the same damage tolerance can be afforded by less α-Mo (thus improving the oxidation resistance of the alloy).

The strength and ductility of body-centered cubic molybdenum is strongly influenced by impurities and solid solution strengthening. Silicon is well known[18-20] as a solid solution strengthener of Mo. Silicon has been shown to segregate to dislocation cores[18] and grain boundaries,[19-22] leading to embrittlement of α-Mo based alloys. Numerous strategies have been employed to combat this embrittlement, including alloying with zirconium[9, 10, 21-23], rhenium[24] (which realized significant gains in ductility, but required nearly equal weights of molybdenum and rhenium), or $MgAl_2O_4$ spinel.[25-30]

Sturm, *et al.*[20] investigated the influence of Si on the ductility and toughness of Mo. They saw a marked drop in room temperature ductility, to nearly zero, with the addition of only 0.1 wt.% Si. While dramatic increases in yield strength were realized with small amounts of Si additions (Fig. 3.3), the yield strength of each alloy was insensitive to grain size. The authors ascribe this behavior to a failure of the underlying assumption of a single dislocation pile-up in the Hall-Petch model in the case of these alloys.[20] While the yield strength of these alloys greatly increased with increasing Si content, the authors saw a precipitous drop in the room temperature toughness from ~ 24 MPa√m with no silicon to ~ 4 MPa√m with the addition of only 1 wt.% Si.[20] A weakening of the grain boundaries by Si segregation, as indicated by a transition to intergranular fracture, is blamed for this significant reduction in fracture toughness.

Zirconium has been shown[21, 22] to be an effective ductilizing agent in molybdenum alloys. Miller, *et al.*[21] showed a marked increase in the ductility of Mo weldments and a transition from an intergranular to a transgranular fracture mode. They attributed this increase in ductility to the presence of small amounts of Zr (0.16

[a] Damage-tolerance here represents resistance to crack propagation or more generally a tolerance to the presence of cracks. An essential requirement of almost all structural materials, it is afforded by the often mutually exclusive mechanical properties of strength combined with ductility and toughness.

at.%) which was added to getter oxygen and nitrogen impurities, as well as small (< 100 appm) C and B additions meant to strengthen the grain boundaries. These additions prevented the segregation of oxygen to the grain boundaries, where oxygen is a well-known embrittling agent. Miller and Bryhan[22] elaborated on this effect. Again, Zr was shown to segregate to grain boundaries, where it competed with O, and possibly N and Si for grain boundary sites, and a significant increase in the ductility of Mo weldments was noted.

Building on the works of Miller, *et al.*, a number of recent publications[9, 10, 23] have concentrated on Zr additions as a means to prevent Si grain boundary segregation in Mo-Si alloys (and thus the α-Mo phase in Mo-Si-B alloys). Saage, *et al.*[23] added 1 at.% Zr to mechanically-alloyed Mo-1.5Si (at.%). They saw a reduction in grain size of approximately 50% with the addition of Zr. Even without added Zr, Saage *et al.*[23] saw a reduction in grain size of more than an order of magnitude for their mechanically alloyed material as compared to a traditional blended-powder alloy. Bend tests of their alloys revealed limited ductility at room temperature in the Zr-added material, while the Mo-Si alloy and an alloy containing 0.7 vol.% Y_2O_3 (added to reduce the grain size below 1 μm) exhibited no ductility even at 538°C. At higher temperatures, the Y_2O_3-added material did exhibit ductility, but the strength of this alloy was diminished compared to the Zr-added material. Their results are reproduced as Fig. 3.4. The authors attributed these effects to increased grain boundary cohesion and a reduction in grain size, both resulting from the addition of Zr [23]. Their Auger electron spectra of the grain boundaries of their Zr-added material show a depletion of Si at the grain boundaries, which they attribute to a competition between Zr and Si for residence within grain boundaries[23], confirming the earlier work of Miller, *et al.*[21, 22]. Saage, *et al.* also reported a significant increase in the amount of transgranular cleavage with the addition of Zr,[23] an indication of increased grain boundary strength.

Another additive which has been shown to increase the ductility of Mo alloys is $MgAl_2O_4$.[25-29] Scruggs, in his 1967 patent,[27] attributed this increased ductility in Mo and Cr alloys to gettering of oxygen by the brittle spinel particles, much in the same way that Zr is thought to act as a gettering agent.[21-23] An increased ductility was verified for Cr alloys by Brady, *et al.*[30] with the addition of $MgCr_2O_4$ spinel, but the impurities (nitrogen) did not directly incorporate into the spinel. Instead, nitrides precipitated at the Cr/spinel boundaries. They found similar behavior for non-spinel-forming additions, and claim that the impurity segregation behavior is not unique to spinels.

With this understanding, Sun[25] studied the thermomechanical response of Mo alloys containing fine dispersions of $MgAl_2O_4$ spinel and MgO. She found that the spinel distribution and particle size was an important factor in the ductility of her alloys. Smaller spinel particles led to higher ductilities, though no explanation was

given as to why this might be the case except to quote the work of Scruggs.[27] She also claimed that processing time was critical for developing ductility, as longer processing times would lead to stronger bonding between the spinel and matrix. She used the work of Schneibel, *et al*.[28] as a basis for comparison, as their alloy had nearly the same composition, but was hot-pressed for four times as long.

Lee[26] expanded upon Sun's work, and saw a marked increase in surface microcracking for alloys containing spinel after thermal cycling. He attributed this cracking to the differing coefficients of thermal expansion for Mo and $MgAl_2O_4$. Microcracks were seen to emanate from large spinel particles, with fewer microcracks visible in samples containing a finer distribution of spinel. He also noted an increase in brittle failure with "excessive" spinel inclusions, mirroring the results of Sun.[25] Lee blames gettering of "excessive" amounts of MoO_x for the decreased ductility of the high spinel content alloys, though there is little proof provided for this argument. More likely, the brittle spinel particles act as crack initiation sites and fail prematurely. Lee[26] showed evidence of particle/matrix decohesion after thermal cycling in air at 650°C and 1000°C. He credits oxygen gettering by the spinel particle, leading to the formation of MoO_x which then volatilized, for the formation of the gaps between the spinel and matrix phases. What is a more likely phenomenon is absorption of oxygen from the air atmosphere during the thermal cycling test. The gaps between spinel particles and the matrix are formed as the bonds between the particles and matrix are broken by thermal stresses.

Schneibel, *et al*.[28] showed an increase in ductility for a Mo alloy containing 2.5 vol.% $MgAl_2O_4$ spinel, but the ductility subsequently decreased as more spinel was added. While the authors felt an increase in ductility caused by oxygen gettering could not be discounted, they claimed that grain size refinement was likely a larger contributor to ductility. They claim that the ductility gains outweigh the increase in crack initiation sites (the brittle spinel particles), at least at low spinel contents. As the spinel content is raised, eventually the embrittling nature of the spinel particles will overtake the ductilization afforded by a refined grain size.

This effect was proven by Gunter, *et al*.[29] who showed that the increased ductility afforded by spinel additions was not accompanied by an increase in fracture toughness. In fact, the fracture toughness of alloys containing as little as 0.1 vol.% and as much as 5 vol.% spinel was identical. As depletion of oxygen at grain boundaries is known to increase crack blunting, [31] an increase in the fracture toughness is expected if oxygen gettering is taking place. Since no toughening with increased spinel content was observed, oxygen gettering was not the cause of increased Mo ductility with the addition of spinel. Instead, Gunter *et al*.[29] proposed that grain refinement, and the subsequent ductility increase, can be achieved via alternate means without

embrittlement. Spinel inclusions act as crack initiation sites, much in the same way as the Y_2O_3 particles studied by Saage, *et al.*[23] and Brady, *et al.*[30] In fact, Brady *et al.*[30] do not provide any grain sizes for their materials, so it is possible that some of the ductility gains they realized were caused by grain refinement. Ti additions did not improve the ductility of Cr,[30] lending credence to a grain refinement mechanism in that system as well; that Zr limits oxygen segregation (and acts as a gettering agent) has been shown,[23] but some of the ductility achieved by Saage, *et al.* was likely attributable to the accompanying grain refinement observed with the addition of Zr. However, Saage, *et al.*[23] also showed that grain refinement alone is not enough to allow for room temperature ductility in α-Mo solid solutions. Silicon and oxygen in the grain boundaries are highly detrimental, and any ductilizing agent added to Mo must prevent their segregation, as well as refine the grain size in order to be truly useful.

Jain, *et al.* and Jain and Kumar have studied the high temperature compressive,[32] tensile[19] and tensile creep[18] responses of Mo-0.9Si-0.15B alloys developed to mimic the expected composition of the solid solution phase in two- or three-phase Mo-Si-B alloys. Their arc-melted, cast, extruded and forged alloy consisted of a saturated α-Mo solid solution with minor (3-5 vol.%) Mo_5SiB_2 inclusions. Jain, *et al.*[32] reported a significant increase in the compressive yield strength at 1000°C and a strain rate of 10^{-4} s^{-1} for their solid solution alloy (550 MPa compared to 170 MPa for pure Mo). They also observed gradual work hardening for their solid solution alloy, while pure Mo exhibited no work hardening. However, Jain and Kumar[19] found that the composition of the samples tested by Jain, *et al.*[32] varied along the extruded direction. As a result, the dissolved Si level varied from sample to sample. In the two single phase materials tested, the Si content varied from 1 at.% to 2 at.% in a bimodal distribution. Tensile tests at 1200°C and 10^{-4} s^{-1} revealed a yield strength in the 2 at.% Si samples (220 MPa) that was twice that of the 1 at.% Si samples (110 MPa). Long anneals at both 800°C and 1200°C were unable to relieve the microsegregation present in these alloys. However, it should be noted that the Si content of these alloys is much lower than that actually found in the α-Mo phase in two- or three-phase alloys.[19]

From constant load creep tests Jain and Kumar[18] were able to determine a creep rate equation for the Mo solid solution, as given by:

$$\dot{\varepsilon} = 1.6\ x\ 10^{-5}\sigma^{5.47}\exp(-360\ kJ\ mol^{-1}/RT) \tag{3.1}$$

The calculated values for the stress exponent and the activation energy closely match those characteristic of lattice diffusion of Mo, implying dislocation climb as the dominant mechanism for tensile creep. The extremely high stresses supported by their alloys led the authors to claim that Si segregation to dislocation cores was the rationale. Atom probe field ion microscopy and Auger electron spectroscopy were used to prove

that Si segregates to dislocation cores and grain boundaries. Precipitation of Mo_5SiB_2 particles on the grain boundaries during creep tests were also used as evidence of grain boundary segregation of Si.

3.1.1.2 Mo_3Si

As $MoSi_2$ cannot exist in thermodynamic equilibrium with α-Mo,[13, 16] more Mo-rich silicides such as Mo_3Si, Mo_5Si_3 and Mo_5SiB_2 must act as the oxidation- and creep-resistant phases in high Mo content Mo-Si-B alloys. Owing to its higher Mo content, Mo_3Si will have lower oxidation resistance than $MoSi_2$. Mo_3Si forms in the A15 cubic structure and was initially thought to be a line compound.[33] Rosales and Schneibel[34] showed that some compositional flexibility is possible, as compositions with narrow window of less than 0.5 at.% Si around 24 at.% Si (*i.e.* Mo_3Si is not a stoichiometric compound) produced single phase Mo_3Si. They also reported no trend in hardness or fracture toughness with varying Si content. The average fracture toughness of Mo_3Si is 3 MPa√m,[34] though Rosales[35] reported a slightly lower indentation toughness of 2.4 MPa√m for directionally solidified single crystals. Swadener, *et al.*[36] grew single crystals of Mo_3Si using an optical floating zone furnace. Nanoindentation of their single crystals revealed highly anisotropic elastic behavior (C_{11} = 505 ±35 GPa, C_{12} = 80 ±60 GPa and C_{44} = 130 ±15 GPa). Slip was found to occur in both {110}(100) and {100}(010) systems.

The high temperature compression behavior of Mo_3Si *in vacuo* at 1325°C was studied by Rosales, *et al.*[37] They observed significant yield points in some crystallographic directions attributed to few mobile dislocations. Slip was seen to occur on {001} and {012} planes, with similar critical resolved shear-stresses. Since only three slip systems are active, even at 1325°C, Mo_3Si displays very little plasticity. Rosales and Martinez[38] showed that alloying Mo_3Si with Nb increased both the strength and ductility of Mo_3Si at 1400°C and a strain rate of $10^{-5}s^{-1}$. Mo_3Si forms a solid solution with Nb, via a diffusional substitution process, so an increase in strength at 1400°C is not unexpected.[38] The increase in ductility was rationalized as a reduction in the ductile-brittle transition temperature with the addition of Nb.

Very little data has been published on the oxidation behavior of Mo_3Si as a single phase. Both Ochiai[39] and Rosales, *et al.*[40] have studied the oxidation behavior of Mo_3Si as a function of Al additions. At 900°C, Ochiai[39] reported a significant decrease in mass loss after 1 and 10 hours of oxidation for an alloy containing 15 mol.% Al. However, the mass loss increased as the Al was raised above 15 mol.%. A mixed Al_2O_3-SiO_2 scale was postulated to act as a better oxygen barrier than either a pure Al_2O_3 or SiO_2 scale. Chromium additions of less than 15 mol.% were shown to greatly improve the oxidation resistance of both Mo_3Si and Mo_3Al at 900°C.

Rosales, *et al.*[40] conducted a much more comprehensive study on the effect of Al on the oxidation resistance of Mo_3Si. Cyclic oxidation experiments were performed at temperatures ranging from 700-1000°C on directionally solidified Mo_3Si alloys containing 8-16 at.% Al. The oxidation resistance of Mo_3Si was found to increase with increasing Al content. Unalloyed Mo_3Si failed catastrophically by a pesting reaction, while the highest Al-content alloy displayed the two-stage oxidation kinetics typical of MoO_3 volatilization followed by subsequent formation of a passivating Al_2O_3-SiO_2 scale. The oxide was found to form in two layers: Al_2O_3 on the outer surface of the material and SiO_2 between the substrate material and the outer Al_2O_3 scale. The SiO_2 layer was proposed to form after oxygen diffusion through the Al_2O_3 layer allowed some Mo_3Si to oxidize.

3.1.1.3 Mo_5Si_3 (T1)

Mo_5Si_3 exhibits highly anisotropic thermal expansion,[41-43] so much so that the residual stresses that develop during cooling can exceed the fracture strength of the material. Mo_5Si_3 forms in a tetragonal structure. As a result of this structure, and the highly covalent nature of the basal plane bonds, the coefficient of thermal expansion ratio, CTE(c)/CTE(a) is approximately 2.[41-43] Additions of Nb or V can reduce this anisotropy. Nb reduces CTE(c) by substituting for Mo in *16k* sites, elongating Mo chains along the c axis and reducing the anharmonicity of the chains.[42] V substitutes for c-axis Mo, directly reducing the c/a ratio and thus the thermal expansion anisotropy. CTE(c)/CTE(a) ratios as low as 1.0 and ~1.25 have been reported for highly V-alloyed[41] or Nb-alloyed[42] materials.

Mo_5Si_3, with a high Mo content, has poor oxidation resistance[44] though it performs better than Mo_3Si. Boron has been shown[45-49] to be highly effective at improving the oxidation resistance of Mo_5Si_3. Meyer and Akinc studied the isothermal oxidation behavior of Mo_5Si_3 and B-Mo_5Si_3 between 600°C[45, 46] and 1450°C.[47] At 800°C, their undoped Mo_5Si_3 suffered from rapid oxidation and a pest reaction. The oxidation resistance of Mo_5Si_3 was shown to be the best at 900°C,[47] though the SiO_2 scale that formed was always porous and weight loss was always linear. They found that outward transport of MoO_3 through the SiO_2 scale was rate-limiting in the 900-1100 °C temperature regime; the authors were unable to clarify which transport process was rate-limiting. Similar behavior was noted by Natesan and Deevi[49] for undoped Mo_5Si_3 hot pressed alloys and single crystals.

Small amounts of B, 1-2 wt.%, can improve the oxidation resistance of Mo_5Si_3 by more than five orders of magnitude.[47] Meyer and Akinc[47] reported no pesting reaction at 800°C and parabolic weight gain above 1050°C. The transition to parabolic oxidation kinetics implies that oxygen diffusion through a dense scale is the rate-limiting step.

The oxidation behavior of B-Mo_5Si_3 exhibits two stages: (1) initial transient mass loss as Mo is oxidized and escapes as MoO_3 and (2) passivation by a dense SiO_2 scale. The mass loss decreased with increasing B content.[45] Boron is a well-known flux of silica.[50] Increasing the boron content lowers the viscosity of the SiO_2 scale, allowing for quicker surface coverage and a shorter transient period. As a result, the overall mass loss of the alloy will be lower, even though B increases the diffusivity of oxygen through the scale.[51]

Mechanical properties for Mo_5Si_3 have been determined at both ambient[52] and elevated temperatures.[48, 53-55] Ström[52] found a solubility range of ~ 2 at.% Si, implying that Mo_5Si_3 is also not a line compound and can exist at lower silicon contents than originally posited by Nowotny, *et al.*[13] He also found that the indentation toughness and Vickers hardness of Mo_5Si_3 depended upon Si content. At both hypo- and hyper-stoichiometric compositions (no exact compositions were given), the indentation toughness of the material was lower than the stoichiometric composition, though the scatter is very large, nearly 50% of the reported value of 2.4 MPa√m. The relatively low hardness and toughness of the off-stoichiometric compositions was associated with CTE mismatch cracking, as well as the much lower hardness of $MoSi_2$ in the case of the hyper-stoichiometric composition. The hypo-stoichiometric composition contained second phase Mo_3Si particles while $MoSi_2$ was found in the hyper-stoichiometric alloy.

Yoshimi, *et al.*[55] investigated the high temperature compression behavior of Mo_5Si_3 single crystals. They found that temperatures in excess of 1300°C were required for plastic deformation. They tested the compression behavior along four crystallographic axes: [001], near-[101], near-[111] and [100]. At all testing temperatures above 1200°C a large drop in flow stress after yielding was observed for the near-[101], near-[111] and [100] orientations. Compression along the [001] axis did not exhibit a yield drop, and the post-test sample was heavily sheared. The authors ascribed this behavior to insufficient slip systems in this direction. For the near-[101], near-[111] and [100] orientations, after the initial yield drop, the flow stress remained relatively constant, which the authors modeled as constant stress creep. They found that the activation energy varied with orientation, obtaining a value of 458 kJ/mol for the near-[111] orientation and 490 kJ/mol for the near-[101] orientation. The authors assumed no variation in stress exponent with orientation.

The compressive creep behavior of Mo_5Si_3 and B-doped Mo_5Si_3 was studied in more depth by Meyer, *et al.*[54] They performed constant stress creep tests over the range 1220°C-1320°C and 140-180 MPa. Samples were held under load and at temperature until the sample strained ~1%, then the temperature was increased by 20°C and another data point was recorded. The authors tested samples consisting of nominally pure Mo_5Si_3, as well as the B-doped material which consisted of ~ 54 vol.% Mo_5Si_3 with the

balance of the material consisted of nearly equal volume fractions of Mo_5SiB_2 and Mo_3Si. They reported an average stress exponent of 4.3,[54] indicating dislocation climb as the dominant creep mechanism, though no clearly defined primary or secondary creep regimes could be discerned. The activation energies for all test conditions fell between 386 and 412 kJ/mol, implying no change in the dominant creep process over the test regime. While the Mo_5Si_3 phase in the B-doped material exhibited no dislocation activity, moderate dislocation activity was observed in the Mo_5SiB_2 phase. A much higher dislocation density was observed in the Mo_3Si phase and polygonization occurred after 5% strain, which the authors state resulted from dislocation climb. The lack of dislocations in the Mo_5Si_3 phase was contradicted by the work of Yoshimi, *et al.*[55] who found evidence of slip in single crystals of Mo_5Si_3, but no explanation as to why Meyer, *et al.* did not see dislocations in the Mo_5Si_3 phase is given by either set of authors. Significant cracking was observed in the Mo_5Si_3 phase at the highest loads and temperatures. Meyer, *et al.*[54] proposed cracking and sliding of Mo_5Si_3 grains as the means by which Mo_5Si_3 accommodates creep deformation.

3.1.1.4 Mo_5SiB_2 (T2)

Mo_5SiB_2 forms in $D8_l$ body-centered tetragonal structure, with a unit cell containing 32 atoms (20 Mo, 4 Si, 8 B).[56, 57] The atoms arrange into four distinct layer types: layer A containing only Mo atoms, layer B containing only Si, layer C containing Mo and B atoms and another layer containing only Mo atoms, but shifted by one half the base diagonal in relation to the A layer, labeled as layer $A_{1/2 1/2}$.[57] Layers are stacked in a $BACA_{1/2 1/2}BA_{1/2 1/2}CAB$ structure, as shown in Fig. 3.5. The two different A-type layers are required to accommodate the significant difference in atomic radii between Si and B. As a result of this complicated crystal structure, the coefficient of thermal expansion of Mo_5SiB_2 is nearly isotropic; Rawn *et al.*[56] reasoned that the differing thermal response of the various bond types lead to low CTE anisotropy. Rawn *et al.*[56] observed a CTE of ~7.7×10^{-6} K^{-1} for polycrystalline Mo_5SiB_2, on par with the values reported by Ito, *et al.*[58] for single crystals and Field, *et al.*[59] for a polycrystalline alloy.

Mo_5SiB_2, like Mo_3Si and Mo_5Si_3, is not a line compound and exhibits some compositional flexibility around the stoichiometric concentrations (Fig. 3.1). In fact, Sakidja, *et al.*[60] demonstrated the potential of α-Mo precipitation from supersaturated Mo_5SiB_2 as a means of ductile phase reinforcement of Mo_5SiB_2. Studies of the effects of a number of transition[57, 61, 62] and refractory metal[63] alloying additions on the stability of Mo_5SiB_2 and multiphase regions containing Mo_5SiB_2 (*i.e.* the α-Mo-Mo_3Si-Mo_5SiB_2 three phase region) have recently been published. A combination of geometric and electronic factors was shown[57, 61] to increase the stability of Mo_5SiB_2. A valance electron per atom (*e/a*) ratio of 5.5 was shown[61] to exhibit a minimum gap in total density of states. Mo has an *e/a* ratio of 6, while transition metals like Ti, Zr and Hf have *e/a* ratios of 4. All of

these transition metals form extended solid solutions with Mo_5SiB_2, but only Ti has been shown[62] to be effective at stabilizing a three phase equilibrium. Both Hf and Zr were shown[62] to limit the stability of a α-Mo-Mo_3Si-Mo_5SiB_2 three-phase equilibrium as a result of the formation of MoSiHf and MoSiZr ternary phases. It was argued by Sakidja and Perepezko[61] that a favorable *e/a* ratio was not the only factor driving extended solubility of transition metal additions. The authors claimed that rare-earth metal substitutions would not form extended solid solutions in Mo_5SiB_2, even though rare-earth metals have favorable *e/a* ratios; the large size difference between atoms like Y and Mo was stated as the cause.

Sakidja, *et al.*[63] showed a larger α-Mo/Mo_5SiB_2 two-phase equilibrium regime could be obtained by substitution of Nb or Cr for Mo in Mo_5SiB_2. Nb increased the *c/a* ratio of Mo_5SiB_2 as a result of its larger atomic radius, thus allowing more Si to substitute for B and lowering the B/Si ratio. Cr, by contrast, lowered the *c/a* ratio as a result of its smaller atomic radius, allowing more Si to be replaced by B. In both situations, altering the *c/a* ratio of Mo_5SiB_2, and by extension the effective atomic ratios of the metalloid components (*i.e.* altering the B/Si ratio), stabilized the α-Mo-Mo_5SiB_2 two-phase field over a larger compositional range.[63] Readers are directed to Perepezko, *et al.*[2] for a more thorough discussion of the thermodynamics and phase stability of the Mo-Si-B system.

Only a few studies have been published on the mechanical properties of Mo_5SiB_2.[58, 59, 64, 65] While few dislocations have been observed in Mo_5SiB_2, slip has been observed on the <100>{010} slip system.[59, 64, 65] Ihara, *et al.*[65] reported an indentation toughness of Mo_5SiB_2 of ~ 2 MPa√m, comparable to other Mo-Si intermetallics. Hayashi, *et al.*[64] and Ito, *et al.*[58] studied the creep response of Mo_5SiB_2 in compression. The creep rate for [021] oriented Mo_5SiB_2 single crystals at 1300°C was reported[58, 64] to be three orders of magnitude lower than that for the hardest orientation of $MoSi_2$, highlighting the excellent creep resistance afforded by Mo_5SiB_2. Unfortunately, the creep mechanism for polycrystalline Mo_5SiB_2 was not fully characterized by Hayashi, *et al.*[64] Plastic anisotropy of Mo_5SiB_2, grain boundary sliding and the presence of small amounts of second phases contributed to confusion about the dominant creep mechanism. The authors did report a stress exponent of 4.6, however.

Very little information exists on the oxidation behavior of pure Mo_5SiB_2. Yoshimi, *et al.*[66] have published the only study to date, though their samples contained small amounts of MoB, Mo_2B and Mo_5Si_3 as secondary phases. As Nunes, *et al.* showed,[16] direct solidification of pure Mo_5SiB_2 is very difficult, and these secondary phases will remain even after long heat treatment. Yoshimi, *et al.*[66] tested the short-term isothermal response of their material between 700°C and 1400°C. Below 800°C MoO_3 formed then volatilized, leading to slight mass gain followed by subsequent mass loss.

Above 1000°C two-stage oxidation kinetics were observed and two layers of oxidation product covered the base material. During the initial transient period, Mo, B and Si simultaneously oxidize forming volatile MoO_3 and B_2O_3 as well as a dense SiO_2 scale. As MoO_3 and B_2O_3 volatilize, SiO_2 is accelerated by rising Si activity. When a SiO_2 scale completely covers the substrate surface oxygen transport through the scale becomes the rate limiting step and parabolic oxidation kinetics dominate. At this point, the oxygen partial pressure at the oxide interface is governed by the equilibrium between Si and SiO_2. Si is selectively oxidized at these oxygen partial pressures, leaving behind an interlayer of α-Mo. The oxidation resistance for Mo_5SiB_2 is not as good as B-doped Mo_5Si_3 since the B content (and thus oxygen diffusivity through the borosilicate scale) is much higher in the former case.

3.2 Processing

Many strategies have been employed to process Mo-Si-B alloys. Direct solidification of Mo-rich alloys has been frustrated by a high degree of solute segregation during solidification. Segregation of B during solidification leads to the precipitation of unwanted phases like MoB and Mo_2B.[16] As stated in Section 3.1.1.4, much research has been conducted to find alloying additions that can stabilize Mo_5SiB_2 over a wider compositional range and reduce solidification segregation.

Direct solidification of Mo-Si-B alloys via repeated arc-melting and casting is the processing method most utilized in the study of Mo-Si-B alloys owing to its relative processing ease; the disadvantages of the processing method have been enumerated above. Directional solidification has also been used by some researchers to produce high aspect ratio grains. Powder metallurgy methods have recently been developed to process Mo-Si-B alloys using solid state reactions. Hot pressing and sintering of blended powders, reaction hot pressing, plasma spraying, rapid solidification via gas atomization, plasma rotating electrode processing, vacuum annealing Mo-Si-B powders to create material with a continuous α-Mo phase, mechanical alloying and reaction synthesis of Mo, Si_3N_4 and BN powders have all been used with great success to process Mo-Si-B alloys. We will briefly describe a number of these processing methods and their resultant phase morphologies.

3.2.1 Ingot Metallurgy

Arc-melting is used by many researchers to directly solidify Mo-Si-B alloys[61, 67-85] or as a precursor material which is pulverized then reconsolidated.[82-87] Elemental Mo, Si and B are melted using a very high amperage DC current arc. A variety of microstructures are possible using this method, as the equilibrium microstructure is obtained from the melt. By changing the composition of the alloy, it is possible to alter

the phase morphology. For example, small, isolated islands of α-Mo form within an intermetallics matrix for Mo-4Si-1B,[84] while a mixture of two-phase α-Mo/Mo_5SiB_2 eutectic and α-Mo/Mo_5SiB_2/Mo_3Si three-phase eutectic forms for Mo-5.1Si-1.3B.[61] Arc-melting and direct solidification has been successfully used to form both α-Mo-Mo_3Si-Mo_5SiB_2[84] and Mo_5SiB_2-Mo_3Si-Mo_5Si_3[45] alloys.

The optical floating zone technique has recently been used[88-91] to directionally solidify Mo-Si-B alloys. A halogen or xenon light beam is focused on a precast Mo-Si-B rod, creating a small molten zone;[92] the light beam, and thus the molten zone is then slowly moved along the sample, resulting in a directionally solidified alloy[88-91] or a single crystal.[58] Ito, *et al.*[88] pioneered the use of an optical floating zone furnace to grow directionally solidified two-phase Mo-3.4Si-2.6B eutectic alloys. The authors obtained a Mo_5SiB_2 matrix surrounding fine (~ 10 μm) α-Mo grains, interspersed with some coarser α-Mo dendrites at a growth rate of 5 mm/hr. Wang, *et al.*[90, 91] directionally solidified a Mo-5Si-1.4B alloy using growth rates of 10 and 30 mm/hr. They found slight microstructural alignment along the growth direction, with the degree of alignment increasing with increasing growth rate. Transverse sections revealed a two-phase α-Mo-Mo_5SiB_2 dendritic microstructure. A finer, three phase eutectic (α-Mo-Mo_5SiB_2-Mo_3Si) was found in the interdendritic regions. The authors reported a coarse and inhomogeneous grain morphology. The coarsest α-Mo dendrites were ~50 μm long in the case of the slower growth rate and 40 μm in the case of the faster growth rate.

3.2.2 Powder Metallurgy

Powders rapidly solidified from the melt[11, 18, 19, 32, 93-101] can avoid the formation of deleterious boride phases. Small, spherical particles consisting of either an intermetallic matrix phase surround primarily solidified α-Mo[93, 94] or an α-Mo matrix phase [95-97] can be produced, depending on the atomizing gas (and thus cooling rate). Plasma rotating electrode processing, another rapid solidification technique, utilizes electric arc heating to melt a rotating electrode. Centrifugal forces eject the molten melt, which solidify into spheres in flight. The PREP process has proven effective at forming α-Mo matrix powders containing Mo_5SiB_2 dispersions.[18, 19, 32, 98-101] Consolidation of these powders by hot pressing and sintering leads to the formation of dense, well bonded three-phase microstructures.

Low pressure plasma spraying has been used with some success to deposit Mo_5Si_3-MoB-$MoSi_2$ coatings on stainless steel[102-104] and Mo_3Si-Mo_5Si_3-Mo_5SiB_2 coatings on Mo-ZrC alloys.[105] Argon carrier gas is used to inject Mo-Si-B powders into a DC plasma flame. The powders melt then splat cool upon contact with the substrate. Initial experiments[102] using air as a carrier gas showed unacceptable levels of silicon loss and oxygen impurities, so inert atmospheres and carrier gases must be used. A high degree

of variation in the grain size and composition of individual splats implies that the solidification undercooling and composition can vary significantly from layer to layer in the coating. High temperature (>1800°C) annealing is required to recrystallize the microstructure and improve the coating homogeneity.[102] Approximately 8 wt.% of the Mo_5Si_3-MoB-$MoSi_2$ coating is silica, reducing the high temperature strength of the coating, but improving its ductility.[104] Dense coatings are possible with this technique,[105] highlighting the potentials for using low pressure plasma spraying to apply oxidation-resistant coatings to ductile-phase toughened α-Mo-based alloys.

Reactive hot-pressing combines the increased reactivity experienced by a material as it undergoes a phase transformation with the application of pressure to create a dense and strongly bonded material.[106] Only a few researchers[107-112] have pursued this processing path. Reactive hot pressing has been particularly useful for the manufacture of Mo-Si-B-Al alloys.[107-111] Mitra, *et al.*[107] added Al to their material as a means to scavenge oxygen impurities from their starting materials. They held their Mo-Si-B-Al powder blends at 700°C for 1 hour before hot-pressing to allow liquid Al to react with any SiO_2, MoO_3 or B_2O_3 to form α-Al_2O_3. In this way, the starting materials are purified, and oxygen impurities in the alloy are tied up in Al_2O_3 inclusions. The relatively low reaction temperature was required to limit the fluidity of the Al liquid and prevent its escape from the hot press die during the reaction step. The free energy of Al_2O_3 formation is lower than that for SiO_2 or MoO_3, driving the formation of Al_2O_3. Li and Peng[112] have shown that this technique can also be used to create Mo-Si-B alloys without the addition of Al. They held their material at 1400°C for 2 hours before raising the temperature to 1600°C and applying pressure. Utilizing this method the authors were able to create fully dense Mo_3Si-Mo_5SiB_2-matrix materials with 18-31 vol.% discontinuous α-Mo, with the α-Mo content scaling inversely with increasing B content.[112]

Hot pressing of blended powders provides a relatively simple means of creating a two- or three-phase microstructure without the pitfalls of direct solidification and is widely used in processing of Mo-Si-B alloys. This technique has been used to successful compact and sinter mixtures of molybdenum silicides, Mo and B[81, 113],[81, 112] precast Mo-Si-B powders, [82-87] elemental Mo, Si and B[114] as well as rapidly-solidified,[18, 19, 32, 95-101] surface-modified,[115-118] reaction synthesized[15, 119-122] or mechanically alloyed[4, 10, 11, 14, 123-136] Mo-Si-B powders. Heat treatment is required after hot pressing to further homogenize the material. The resultant microstructure depends greatly on the chosen powder mixture and the particle size of the starting material. Schneibel, *et al.*[80] synthesized an Mo_5Si_3-Mo_5SiB_2-Mo_3Si alloy from $MoSi_2$, Mo and B, while the elemental Mo, Si and B powders hot pressed by Nieh, *et al* [114] produced an alloy containing discontinuous islands of α-Mo within an Mo_3Si-Mo_5SiB_2 matrix.

Kruzic, *et al.*[116-118] demonstrated the effects of initial powder size on the microstructure of their continuous α-Mo matrix material. They found it possible to produce microstructures with varying grain sizes while maintaining an equal volume fraction of α-Mo solely by varying the initial powder size. The powders used by Kruzic, *et al.* were produced utilizing the novel surface-modification technique pioneered by Schneibel, *et al*.[115] After pulverizing arc-cast ingots of Mo-20Si-10B (at.%), the resultant powder was vacuum annealed at 1600°C for 16 hr. in a vacuum better than 10^{-3} Pa. At this temperature and oxygen partial pressure Si preferentially oxidized to form volatile SiO[115] leaving behind an α-Mo-enriched surface layer. Compaction, hot pressing and subsequent annealing produces a continuous α-Mo matrix decorated with second phase intermetallic particles.

Reaction synthesis of Mo-Si-B alloys from Mo, Si_3N_4 and BN powders has garnered interest[15, 118-121] as a means of manufacturing Mo-Si-B alloys on an industrial scale[15, 119-122]. This simple processing method relies on reactions between the nitride phases and Mo to form intermetallic Mo_3Si and Mo_5SiB_2 during free sintering in an Ar-10% H_2 atmosphere. Specifically, the intermetallic phases form according to the following reactions:

$$3\ Mo + 2/3\ Si_3N_4 \rightarrow Mo_3Si + 2/3\ N_2 \qquad (3.A)$$

$$5\ Mo + 1/3\ Si_3N_4 + 2\ BN \rightarrow Mo_5SiB_2 + 5/3\ N_2 \qquad (3.B)$$

At a sintering temperature of 1600°C, 95% of theoretical density was achieved after a soak of 6 hours. While Middlemas and Cochran[119] postulated that an increased sintering temperature would increase the density of the alloy further, the accompanying grain growth was seen as unacceptable. Hot-isostatic pressing was chosen as the final consolidation step, as it resulted in nearly 100% dense compacts which retained the desired fine grain structure. Hot isostatic pressing was not possible directly from the unfired powders, as the evolution of N_2 gas during processing prevents full densification. As this process may not require the application of load during sintering, many complex shapes which cannot be made using other powder metallurgy processes are possible. Ultra-fine grain sizes are possible if submicron starting materials are used.[121]

Mechanical alloying has received much attention recently[4, 10, 11, 14, 123-136] as a method for producing ultra-fine grained *in-situ* Mo-Si-B composites. High energy collisions during mechanical alloying lead to repeated cold welding and fracturing of powder particles.[137] This high-energy processing method allows for the formation of non-equilibrium materials, such as supersaturated α-Mo. Krüger, *et al.*[14] demonstrated complete dissolution of 10 at.% Si into a supersaturated α-Mo solid solution, far beyond

the equilibrium 1-2 at.% Si proposed by Nunes, *et al.*[16] and Nowotny, *et al.*[13] This process is also useful for creating ultra-fine grain sizes, as extended milling reduces the grain size into the submicron regime.

The effectiveness of mechanical alloying as a method for producing Mo-Si-B alloys appears to be sensitive to composition. Krüger, *et al.*[14] were able to synthesize Mo-3Si-1B ultrafine grained materials (grain size ~ 1 μm) with a continuous α-Mo phase[123] after 20 hours of milling at 200 rpm and a 3 hour anneal at 1400°C to precipitate the intermetallic phases. Abbasi and Shamanian[124-126] found that a composite structure consisting of nanoscale Si and B particles embedded within a Mo matrix formed from a 5:1:2 (mol.%) mixture of Mo, Si and B powders after 10 hours of milling. Subsequent heat treatment led to the precipitation of Mo_5SiB_2, $MoSi_2$ and Mo_3Si.[124] However, an increase in milling time to 20 hours led to the direct formation of a two-phase α-Mo/Mo_5SiB_2 composite with Mo_5SiB_2 particles embedded in a continuous α-Mo matrix.[125] The authors were also able to produce a three-phase α-Mo-Mo_5SiB_2-Mo_3Si alloy in a two-step mechanical alloying process.[126] After milling a Si-43.62B (wt.%) mixture for 20 hours, Mo was added to create a 5:1:2 Mo:Si:B molar ratio. The powder was milled for an additional 20 hours at 300 rpm to form an α-Mo/$MoSi_2$ nanocomposite. After the second milling step, the powder was annealed for 1 hour at 1100°C to precipitate Mo_3Si from the α-Mo/$MoSi_2$ composite. An increase in secondary milling time reduces the amount of Mo_3Si that forms on subsequent annealing, stabilizing an α-Mo-Mo_5SiB_2-$MoSi_2$ structure. It was postulated by Abbasi and Shamanian[126] that the extremely short diffusion pathways that result from extended mechanical alloying cause this shift in phase structure. By contrast, Yamauchi, *et al.*[127] were unable to directly synthesize Mo_5SiB_2 via mechanical alloying, even after milling a 5:1:2 molar mixture of Mo, Si and B at 500 rpm for 100 hours. A two-step mechanical alloying process, where Mo and Si were milled for 50 hours, then B was added and the mixture was milled for another 50 hours, followed by spark plasma sintering, was required to obtain an α-Mo-Mo_5SiB_2 *in-situ* composite. Yamauchi, *et al.*[127] were unable to form an α-Mo-Mo_5SiB_2 composite from Mo-3.3Si-2.5B. Similarly, in their initial work on Mo-5Si-1.4B, Bakhshi, *et al.*[128] were unable to produce a Mo solid solution, even after 20 hours of mechanical alloying at 365 rpm and 10 hours of annealing at 1100°C. In their subsequent study, Bakhshi *et al.*[129] were still unable to synthesize a solid solution phase for a Mo-5Si-1.4B alloy, but were able to form intermetallic phases in Mo-57Si-10B and Mo-47Si-23B (at.%).

3.3 Oxidation Behavior

3.3.1 Mechanisms

Parthasarathy, *et al.*[67] recently published a comprehensive study of the oxidation mechanisms in α-Mo-Mo_5SiB_2-Mo_3Si alloys. They examined the cyclic oxidation response of Mo-4.3Si-1.7B alloys at temperatures ranging from 500°C to 1300°C. The authors identified four temperature regimes with differing oxidation kinetics. At low (500-600°C) temperatures, Mo, Si and B all oxidize, as evidenced by the formation of a solid MoO_3(Si,B) scale. While the formation of a SiO_2 is thermodynamically preferred, owing to its more favorable free energy of formation, its high viscosity at low temperatures prevents SiO_2 from forming a protective scale. As a result, Mo is free to oxidize and form MoO_3. In this temperature range parabolic weight gain dominates, as oxygen diffusion into the MoO_3 determines the oxidation behavior. Parthasarathy, *et al.*[67] reported a parabolic rate constant, $k_p = 3.41\text{x}10^5 \exp(-94.5 \text{ kJ mol}^{-1}/RT)$ mg/cm^{2}hr$^{0.5}$ in this temperature regime, much smaller than the parabolic rate constant they reported for pure Mo ($k_p = 7.93\text{x}10^{10} \exp(-160.6 \text{ kJ mol}^{-1}/RT)$. The simultaneous oxidation of Mo, Si and B serves to slow the oxidation kinetics at 500-600°C, but the scale is not protective.

Around 700°C (±50°C) a porous borosilicate scale forms but it offers little oxidation resistance. In this temperature regime, linear weight loss dominates. The authors reported a linear rate constant of 3.3 mg/cm^2 hr at 700°C.[67] They showed no difference in the oxidation kinetics between Mo-Si-B and pure Mo in this temperature regime. At these intermediate temperatures, oxidation of Mo into volatile MoO_3 is the rate limiting step. The porous scale provides easy access for oxygen to reach the substrate material. Little B_2O_3 is thought to volatilize at this temperature, so the B_2O_3 content of the scale is high. As a result, the viscosity of the borosilicate scale is very low[67] (5x10^6 Pa-s), to the point that bubbles can form within the scale since complete fining of silica melts require viscosities in excess of 10^9 Pa-s.[138]

At higher temperatures, parabolic weight loss kinetics are active. An initial stage of rapid MoO_3 formation and evaporation is followed by slow weight loss as B_2O_3 begins to evaporate from the scale, slowing the diffusion of oxygen through the scale. However, at 800°C, the scale retains a low enough viscosity to allow MoO_3 to form in bubbles within the scale. As a result, MoO_3 egress and inward oxygen diffusion are paradoxically faster at 800°C than at 1300°C. At higher temperatures, significant B_2O_3 evaporation occurs, raising the viscosity of the scale by as much as 10 orders of magnitude.[139] The evaporation of B_2O_3 also serves to slow the diffusion rate of oxygen by as much as 6 orders of magnitude.[139] The combination of these two effects leads to a more protective scale at 1300°C than at 800°C. Oxygen diffusion, and thus scale growth,

is much slower; the oxide scale at 1300°C is half as thick as the scale that forms at 800°C. Mendiratta, *et al*.[68] have demonstrated the potential of pre-oxidizing material at 1300°C for subsequent use at 800°C, though the lifetime of such a treatment is finite, after which the oxidation kinetics mimicked those for an untreated sample. The oxidation mechanism map developed by Parthasarathy *et al*.[67] and refined by Dimiduk and Perepezko[1] is shown in Fig. 3.6.

Study of the early stages of oxidation in a Mo-3Si-1B alloy was initiated by Helmick, *et al*.[82] Those researchers examined the behavior of both arc-melted and compacted powder alloys when exposed to a number of environments. Specifically, they studied the early stages of formation of the borosilicate scale in static and flowing air, as well as flowing oxygen over the temperature range 700-1100°C. In the first minutes of oxidation the component phases were found to oxidize independently. That is, Mo_5SiB_2 formed MoO_3, SiO_2 and B_2O_3, Mo_3Si formed MoO_3 and SiO_2 and α-Mo formed MoO_3. As the time of oxidation is increased, the borosilicate scale flowed to first cover Mo_3Si then the α-Mo, but channels can form through the scale, mainly at grain boundaries. Fig. 3.7 is a schematic of this oxidation process.[70] The walls of these channels, as well as the substrate, are coated with MoO_2. The oxygen pressure is thought to be high enough within the channels to oxidize Mo to form MoO_2, but is not high enough to convert the MoO_2 to MoO_3. These channels are the last to seal, leading to a transition from transient oxidation to steady-state parabolic weight loss. At 700°C, a porous MoO_3(Si,B) scale formed. This scale was not protective, as evidenced by the observed linear weight loss kinetics. At 816°C, static environments produced channel-free oxide scales, while channels were seen in the oxide scales formed in flowing-gas environments. While the increased removal of MoO_3 was viewed as beneficial, as it sped the formation of a borosilicate scale, removal of B_2O_3 was also increased. Increased B_2O_3 removal had the effect of lowering the scale viscosity and hindering pore and channel healing. As a result, the oxidation performance in flowing gas was worse than static air. At 1000°C, however, little difference in scale morphology was observed for the various environments. A channel-free scale formed for all test conditions. The decrease in scale viscosity was shown to counteract any increase in viscosity from B_2O_3 removal. At this temperature, the scale remained sufficiently fluid to heal any channels that may have formed. At 1100°C, a channel-free scale formed for the static and slow gas flow rate conditions, but a porous scale was observed for the fastest gas flow rate. The rate of B_2O_3 removal was too great for the highest gas flow rate. As a result, the scale viscosity increased to a point where the scale was unable to flow and heal any channels.

Rioult, *et al*.[70] expanded the work of Helmick, *et al*.[82] and probed the effect of microstructural size scale on transient oxidation of Mo-5Si-1.3B at 1100°C. They

examined 3 slices taken from different sections of an arc-cast ingot. Since the bottom of the ingot was in contact with a water-cooled hearth the bottom of the ingot experienced a higher cooling rate than the top. As a result slices from different heights along the ingot will have different microstructural size scales, with the finer microstructures towards the bottom. While the steady-state behavior for each of the microstructures was very similar, the transition time from transient to steady-state oxidation scaled with grain size. As a result, the weight loss during the transient period was lowest for the fine microstructure (10 mg/cm^2), while the intermediate (27 mg/cm^2) and coarse microstructures (32 mg/cm^2) showed significantly more weight loss. As observed by Helmick, *et al.*,[82] each of the constituent phases initially reacted with oxygen individually. A dense borosilicate layer was found over the Mo_5SiB_2 grains, while a nanoporous, non-protective scale was found covering the Mo_3Si grains. No scale was found covering α-Mo, as MoO_3 volatilized at 1100°C. As the oxidation time increased, flow of the borosilicate scale onto the α-Mo began to protect those grains. Likewise, the porous SiO_2 layer covering the Mo_3Si grains began to sinter, likely aided by boron diffusion from neighboring Mo_5SiB_2 grains. As the transient period progressed, the rate of mass loss decreased. Complete oxidation of the smallest α-Mo and Mo_3Si grains exposed the grains underneath. Some of these grains were Mo_5SiB_2, which formed more protective borosilicate glass. A finer microstructure containing homogenously-distributed Mo_5SiB_2 provided a shorter diffusion distance for B into the SiO_2 scale above Mo_3Si grains. Since the diffusion distance was smaller, sintering of SiO_2 occurred more rapidly, leading to a shorter transient period.

This effect was also observed by a number of other researchers. Wang, *et al.*[91] reported poor oxidation resistance at 1200°C for their directionally solidified Mo-3.6Si-2B alloy. The alloy grown at a slower rate (*i.e.* a coarser microstructure) performed worse than the faster growth rate material. This effect was attributed to large α-Mo particles. Schneibel, *et al.*[139, 140] also reported significantly increased weight loss at 1300°C in a coarse grained 21 vol.% α-Mo alloy when compared to a finer grain material containing the same amount of α-Mo[140, 141]. Supatarawanich, *et al.*[71, 72] also reported improved oxidation resistance for finer microstructures, but the alloys they tested did not have the same phase distribution (*i.e.* the α-Mo content and its morphology was different for each of the alloys the authors tested). As a result, it is difficult to determine the effect of microstructure size scale on the oxidation performance of their alloys. One important outcome of their work, however, was the identification of Mo_3Si (or a higher-Si-content phase like Mo_5Si_3) as a necessary component for an oxidation-resistant alloy. Without the additional source of silicon provided by Mo_3Si, the boron content of the oxide scale is too high and oxygen diffuses rapidly through the scale.[71, 72] A 1:1 Si:B ratio was shown to have the best oxidation resistance at 1300°C. Alloys with less Si will form

scales through which oxygen can diffuse rapidly, while alloys with a higher Si:B ratio may not completely passivate, since the scale viscosity may be too high.

3.3.2 Oxidation Behavior in Other Environments

Only a few oxidation experiments have been conducted on Mo-Si-B alloys in atmospheres other than laboratory or dry air. Mandal, *et al*.[142] published the first study of the effects of wet air on the oxidation behavior of Mo-Si-B alloys. They tested three alloys (B-Mo_5Si_3-$MoSi_2$-MoB; Mo_5SiB_2-Mo_3Si; α-Mo-Mo_5SiB_2-Mo_3Si) in dry and wet (up to 2 x10^4 Pa H_2O) air at 1000°C and 1100°C. The transient weight loss of the alloys was independent of test temperature and atmosphere. Instead, the transient weight loss scaled with increasing Mo weight fraction. Water vapor was seen to promote the formation of a thicker borosilicate scale and enhance growth of a subscale region of Mo and MoO_2, but the authors were unable to explain this behavior. However, the α-Mo-containing alloy exhibited the greatest increase in scale thickness and interlayer formation. Thom, *et al*.[143] expanded on the earlier work of Mandal, *et al*.[142] with their isothermal thermogravimetric analysis of the oxidation rates at 1000°C of the same three Mo-Si-B alloys in flowing wet air (2x10^4 Pa H_2O). Thom, *et al*.[143] also evaluated the oxidation response of Mo-Si-B alloys in synthetic combustion gas (N_2-13CO_2-10H_2O-4O_2), utilizing the test methods of Mandal, *et al*.[142] The synthetic combustion gas was formulated to simulate the oxidizing flue gas produced by burning fossil fuels, without any sulfidizing agents. The more accurate tests conducted by Thom, *et al*.[143] showed two effects: (1) the oxidation rates for the B-Mo_5Si_3-$MoSi_2$-MoB alloy and the α-Mo-Mo_5SiB_2-Mo_3Si alloy were not greatly affected by wet air and (2) the initial weight loss for all three alloys was greater in wet air than in dry air. The Mo_5Si_3-Mo_5SiB_2 alloy exhibited slight weight gain after the initial weight loss. The second result contradicts the earlier results of Mandal, *et al.*,[142] but the imprecision of the earlier tests led to large scatter in the data, and possible obfuscation of any effects of wet air on the initial oxidation behavior. Thom, *et al*.[143] postulated that the similar oxidation rates in dry and wet air for the α-Mo-containing alloy represented no change in the salient weight loss mechanism, *i.e.* transport of MoO_2 and MoO_3 through the borosilicate scale. It should be noted, however, that only one sample was tested for each condition. The authors also reported an increase in initial weight loss and scale thickness when samples were tested in synthetic combustion gas. Though their test method precluded accurate calculation of oxidation rates, scales nearly twice as thick as the wet air case were found on the α-Mo-Mo_5SiB_2-Mo_3Si and Mo_5SiB_2-Mo_5Si_3 alloys after exposure to the synthetic combustion gas. The authors reason that the lower Si:B ratio in the Mo_5SiB_2-containing alloys leads to decreased resistance to synthetic combustion gas. No rationale was given as to why this might be the case. The authors also did not relate any justifications

for the enhanced mass transport through the oxide scale for the α-Mo-Mo_5SiB_2-Mo_3Si alloy exposed to wet air.

To date, only one paper regarding the sulfidation behavior of Mo-Si-B has been published. Tortorelli, *et al*.[144] studied the isothermal response of an α-Mo-Mo_5SiB_2-Mo_3Si alloy to exposure to an oxidizing-sulfidizing environment at 800°C. The H_2-H_2S-H_2O-Ar atmosphere to which they exposed their Mo-5Si-1B alloy was meant to mimic the most severe coal gasification conditions. At 800°C, thermodynamic calculations predicted the partial pressures of S (10^{-6} atm) and O (10^{-22} atm) would result in the formation of SiO_2 and MoS_2. After 150 hours of exposure, only a thin corrosion layer formed on the sample surface. The component phases were observed to independently react with the environment. Very little difference was observed in the oxidation-sulfidation behavior for fine- (~1-5 μm) and elongated, coarse-grained (~30-50 x 7-10 μm) materials. The sulfidation response of these alloys was comparable to very sulfidation-resistant Fe_3Al. This result is not wholly unexpected, as Mo is known to be very sulfidation-resistant.[145] Schneibel, *et al*.[146] proposed a study of the behavior of a Mo-3Si-1B alloy in a fully-operational coal gasifier but to date no results have been presented.

Burk, *et al.*[130] examined the effect of low (10^{-6}-10^{-4} bar) and very low (10^{-19}-10^{-12} bar) oxygen partial pressures on the oxidation behavior of a mechanically-alloyed Mo-3Si-1B-1Zr alloy. At these oxygen partial pressures, Si and B are selectively oxidized, while the formation of MoO_2 and MoO_3 is prevented. Isothermal thermogravimetric analysis of the oxidation kinetics between 820°C and 1200°C was performed in both oxygen partial pressure regimes.

At very low oxygen partial pressures, 10^{-19}-10^{-12} bar, MoO_x formation is completely suppressed, and the oxide growth kinetics are determined solely by the formation of SiO_2 and B_2O_3. At 820°C no external scale formed and internal oxidation products of Si were found to a depth of 20 μm after 100 hrs. At 1000°C, a SiO_2 scale began to form, but the viscosity of the scale was too high to allow for complete coverage of the surface. Instead, isolated droplets of SiO_2 were found. At 1200°C, complete wetting of the surface was observed, as individual SiO_2 droplets formed then flowed to cover the surface after 100 hours of exposure. No ZrO_2 was present in the SiO_2, an important implication for the oxidation resistance of this alloy, which will be discussed further in Section 4.3. As a result of the formation of internal SiO_2 precipitates, oxygen transport was slowed and Si diffusion became the rate limiting step in the formation of an external scale. Internal SiO_2 precipitates formed until some critical volume fraction, based on the oxygen partial pressure was achieved, at which point an external SiO_2 scale began to form as droplets.

Unlike exposure to very low oxygen partials pressures, the oxide scale that formed upon exposure to low (10^{-6}-10^{-4} bar) partial pressures of oxygen was not protective. At these oxygen partial pressures, the formation of MoO_x was not completely eliminated. A 1-2 μm MoO_x film formed between a porous SiO_2 scale and the base material. Evaporation of MoO_3 left behind channels within the oxide scale and led to catastrophic oxidation. At 1000°C, a few dense SiO_2 droplets formed on the oxide surface, but their coverage was minimal. At 1200°C, the occurrence of SiO_2 increased, but still very little of the oxide surface was covered. ZrO_2 were observed within the porous SiO_2 scale, so pre-treatment at oxygen partial pressures in the range 10^{-6}-10^{-4} bar are ineffective at preventing the incorporation of ZrO_2 into the oxide scale.

3.3.3 Effects of Alloying Additions

Small additions of a number of alloying additions have been shown to increase the oxidation resistance of Mo-Si-B alloys. Small (<0.3 wt.%) additions of Ti, Hf, Zr and Al were shown to increase the wetting ability of the borosilicate scale, while larger additions (as much as 10 wt.%) were shown to form more refractory oxides underneath the borosilicate scale.[95, 96] Additions of as little as 2 wt.% of Fe, Ni, Co, and Cu have also been shown to improve the oxidation resistance of Mo-Si-B, though no specific mechanism was stated.[97] We will focus on the effects of Al, Nb and Zr alloying additions on the oxidation behavior. The influence of nanoscale Y_2O_3 and La_2O_3 additions will also be reviewed.

The oxidation response of Al-added Mo-Si-B alloys has been extensively studied.[73, 74, 109-111, 147] Paswan, *et al*. studied the isothermal[109, 110] as well as cyclic and nonisothermal[111] response of reaction hot-pressed Mo-5Si-1.4B, Mo-4.3Si-1.1B-1Al and Mo-4.1Si-1.2B-2.6Al alloys. Isothermal experiments conducted between 400°C and 800°C showed a decrease in oxidation resistance with increasing Al content.[109] At high temperatures, spallation of the oxide scale periodically re-exposed fresh material to the oxidizing atmosphere. This spallation was thought to be the result of internal stresses that develop as a result of the differences in coefficients of thermal expansion of the various components. At lower temperatures, α-Al_2O_3 did form, but it could not completely cover the surface. The formation of α-Al_2O_3 retarded the formation of a borosilicate scale, slowing passivation. During cyclic oxidation at 1150°C, mullite ($3Al_2O_3{\cdot}2SiO_2$) and crystalline SiO_2 formed.[111] The appearance of these phases was thought to signal reduced oxidation resistance, as the grain boundaries of mullite and crystalline SiO_2 were thought to act as high diffusivity pathways.[111]

At first glance, this result contradicts the work of Yamauchi, *et al*.[147] who studied the effects of small (≤ 5 mol.%) Al additions on the isothermal oxidation behavior of a Mo-3.3Si-2.5B two-phase α-Mo-Mo_5SiB_2 eutectic alloy. Over the temperature range 800-

1400°C, the oxidation performance of the Al-containing alloys was better than the undoped alloy. The best performance was observed for the alloy containing 1 mol.% Al. At 1000°C, mullite and SiO_2 form a dense, protective scale, while at 1200°C a more needle-like morphology was observed. Two observations can be made to reconcile the different behaviors observed by Paswan, *et al.*[109-111] and Yamauchi, *et al.*[147] Firstly, Al is known to have a slightly negative influence on the oxidation behavior of Mo-Si-B alloys below 1000°C.[95, 96] The isothermal temperature regimes studied only overlap at 800°C, so it is likely that Yamauchi, *et al.*[147] observed the beneficial wetting effect described by Berczik[95, 96] while the lower temperature regime explored by Paswan, *et al.*[109] highlighted the deleterious effects of Al. Secondly, Yamauchi, *et al.*[147] did not probe the cyclic oxidation properties of Al-added Mo-Si-B. It has been proposed that coefficient of thermal expansion mismatches results in large residual stress during cooling,[111] which leads to cracking and spallation of the oxide scale, an effect that would be minimized during an isothermal experiment. It also should be noted that the two-phase eutectic studied by Yamauchi *et al.*[147] contained much less Si and more B than the material studied by Paswan, *et al.*[109-111] (5 wt.% Si and 1.4 wt.% B for Paswan, *et al.*; 3.25 wt.% Si and 2.5 wt.% B for Yamauchi, *et al.* As a result, the viscosity of the oxide scale on the Yamauchi material would be much lower, allowing that scale to self-heal much more rapidly.

Das, *et al.* also studied the effects of Al and Ce additions on the oxidation behavior of Mo-Si-B at low (500-700°)[73] and high (1100°C)[74] temperatures. They saw an improvement in the oxidation resistance of Mo-5Si-1.4B with the addition of 2.6 wt.% Al. This result would also seem to contradict the findings of Paswan, *et al.*[109] who studied an alloy with the same composition. However, it is important to realize that the microstructural morphologies of the two materials were very different, owing to their differing processing methods. The reaction hot-pressed material tested by Paswan, *et al.*[109] exhibited an equiaxed grain structure of nonhomogenously-distributed α-Mo grains ~10 μm in size. The arc-melted material examined by Das, *et al.*[73] displayed primary α-Mo grain structure surrounded by an ultrafine (<0.2 μm interlamellar spacing) three-phase eutectic. Al was thought to refine the interlamellar spacing in the material used by Das, *et al.*[73] This grain refinement, coupled with the formation of Al_2O_3, was thought to speed passivation in the low temperature regime. At low temperatures, the addition of Ce did not affect the oxidation behavior. However, at high temperature, the addition of 0.16 at.% Ce to Mo-4.1Si-1.2B-2.6Al (*i.e.* the alloy tested at low temperature by Das, *et al.*[73]) reduced the total mass loss during a 24 hour exposure to oxygen by ~40%.[74] Inhibition of mullite formation by Ce was proposed as the cause of the observed improvement in isothermal oxidation resistance at 1100°C.

Nb-Nb_5Si_3 *in-situ* composites have been shown to exhibit reasonable room temperature toughness coupled with strength retention at high temperatures.[148] Unfortunately, Nb forms a porous, non-protective Nb_5O_2 oxide upon exposure to air. As a result, the oxidation resistance of Nb-Nb_5Si_3 is very poor above 500°C. Unlike MoO_3, which is volatile, Nb_2O_5 does not evaporate, and can slow the formation of a borosilicate scale.[86] Nb forms a complete solid solution with Mo, so there is potential to combine the superior fracture toughness behavior of Nb-based alloys with the oxidation resistance of Mo-based alloys. Behrani, *et al*.[86] investigated the oxidation behavior of Mo-Si-B and Nb-Mo-Si-B alloys in flowing air at 1000°C. Of the alloys they examined, the Mo_5Si_3(B)-$MoSi_2$-MoB expressed the best oxidation resistance; this result is not unexpected as this alloy contained the lowest Mo weight fraction of the three Mo-Si-B alloys tested. A dense oxide scale, ~10-50 μm thick, formed on the surface after 100 hours of exposure. The thickness of the oxide scale increased with increasing Mo content. The Nb-Mo-Si-B alloys, composed of $(Mo, Nb)_5Si_3$(B)-$(Mo, Nb)_5SiB_2$-$D8_8$, exhibited very poor oxidation resistance. The $D8_8$ phase, $(Nb, Mo)_5Si_3$(B), forms as a hexagonal structure, unlike the body-centered tetragonal T2 $(Mo,Nb)_5SiB_2$ phase, and is not as oxidation-resistant.[149] A highly porous and cracked 600 μm thick SiO_2 scale containing many Nb_2O_5 particles formed after only 10 hours. Residual porosity in the base material, volatilization of MoO_3 and the formation of porous Nb_2O_5 were all believed to cause the poor oxidation resistance of the Nb-Mo-Si-B materials. Though the oxidation resistance of this material was very poor, it exhibited marginal improvement over the oxidation resistance of unalloyed Nb-Si-B materials.[86]

As described in Section 2.1, Zr has been demonstrated as an effective ductilizing agent for α-Mo. As such, the oxidation behavior of Zr-added Mo-Si-B (such as Mo-3Si-1B-1Zr) must be understood. As briefly noted in Section 4.2, Zr can be very damaging to the oxidation resistance of these alloys. The initial oxidation studies performed by Burk, *et al*.[131] revealed two temperature regimes displaying vastly differing oxidation behavior. Grain refinement (though no grain sizes were given) was proposed as the mechanism by which slightly improved oxidation resistance was realized in Zr-added materials at temperatures up to 1100°C. Above this temperature, the oxidation resistance of the alloy drastically decreased. At 1300°C, nearly-linear weight loss was observed, and a scale containing many ZrO_2 inclusions and pores was found. Burk, *et al*.[132] recently published a more comprehensive study on the extremely poor oxidation resistance of Mo-3Si-1B-1Zr above 1200°C. They found that ZrO_2 inclusions in the borosilicate scale and MoO_3 bubble formation caused the degradation of oxidation resistance above 1200°C. The ZrO_2 inclusions within the scale underwent a phase transformation above 1100°C, transforming from a monoclinic to a tetragonal structure. This transformation was accompanied by a volume decrease of approximately 7%.[150] This phase transformation created voids within the scale, allowing the formation of

MoO_3 bubbles. These bubbles eventually collapsed, leaving behind partially-closed pores. Oxygen then gained easy access to unreacted material. It should be noted that this transformation was not instantaneous, so the oxidation behavior of Mo-3Si-1B-1Zr closely matched that of Mo-3Si-1B during the first stages of oxidation. The fine microstructural scale of the alloys tested served to increase the number of grain boundaries, which acted as high diffusivity pathways, a beneficial effect for passivation of Mo-3Si-1B but detrimental in the case of Mo-3Si-1B-1Zr, where quick oxygen diffusion enhanced the production of MoO_3. As a result, MoO_3 formation and not oxygen diffusion through the scale became the rate-limiting step, thus linear weight loss kinetics dominated. As shown by Burk, *et al*.,[130, 132] pre-treatment in extremely low oxygen partial pressures is required to form a borosilicate scale absent any ZrO_2 inclusions.

Nanoscale oxide dispersions of Y_2O_3 and La_2O_3 have also been used to reduce the grain size of Mo-3Si-1B in an effort to increase their ductility.[10, 11, 131] Jéhanno, *et al*.[11] reported improved oxidation performance at all temperatures for alloys containing 0.1 wt.% La_2O_3. While the addition of 0.1 wt.% Y_2O_3 did improve the oxidation resistance at some temperatures, it was not as effective as La_2O_3. More effective grain boundary pinning by La_2O_3, and thus a more refined grain structure, was believed to be the origin of this behavior. A more comprehensive study by Burk, *et al*.[131] highlighted the improved oxidation resistance of La_2O_3-dispersed Mo-3Si-1B. La_2O_3 was found to improve the fluidity and adhesion of the borosilicate scale. Incorporation of La into the borosilicate layer greatly reduced the coefficient of thermal expansion, reducing the occurrence of cracking. The presence of La_2O_3 on grain boundaries was also thought to slow grain boundary diffusion, reducing the speed at which MoO_3 evaporated. At 1300°C, these effects combined to slow mass loss. At 820°C, these effects were even more potent, as the linear weight loss of Mo-3Si-1B at this temperature was replaced by much slower parabolic weight loss.[131] The transition from linear to parabolic weight loss was thought to arise from slower oxygen diffusion through the borosilicate scale.

3.3.4 Surface Modification Strategies

A number of surface modifications have been used to improve the oxidation resistance of Mo-Si-B alloys. Deposition of an Al-Si metallic coating has proven feasible.[151] Pre-oxidation at high temperatures has proved effective at enhancing the oxidation resistance of Mo-3.9Si-1.5B.[68] Other researchers have deposited SiO_2[75] or borosilicate[93] layers with some success. Wang, *et al.*[90] demonstrated improved oxidation resistance when the surface of their directionally solidified Mo-3.6Si-2B alloy was remelted using a Nd:YAG laser in Ar. Regions remelted with the laser exhibited a much finer 3-phase eutectic microstructure than the elongated α-Mo dendrites present in the original material. The oxidation performance of this material was greatly

improved owing to the refinement in grain size. Behrani, *et al*.[87] were able to achieve a three-fold improvement in the oxidation resistance of their Nb-Mo-Si-B materials by the application of a chlorination treatment. Exposure of pre-oxidized samples to flowing Cl selectively removed Nb_2O_5 from the oxide scale, allowing for surface passivation, which was not possible when porous Nb_2O_5 remained in the scale.[86] A chlorination treatment of only 15 minutes was all that was required to remove nearly all the Nb_2O_5 from a 100-200 μm thick oxide scale.[87]

Sakidja, *et al*.[152] examined the effectiveness of aluminum pack cementation as a means for developing an Al_2O_3 surface coating on Mo-3Si-1B. Samples were packed in a mixture of NH_4Cl (1 wt.%, to act as a halide activator), Al-12Si (14 wt.%, the Al source material) and Al_2O_3 (85 wt.%, to act as filler material). The pack samples were then held at 900-1000°C, depending on desired coating thickness, for 50 hours. As a result of this process, a 40-50 μm thick layer of Mo_3Al_8, containing some MoAlB and $Mo(Si,Al)_2$, formed on the material surface. Upon exposure to oxygen (0.2 x 10^5 Pa) at temperatures between 732°C and 1372°C, a dense Al_2O_3 layer formed. This layer afforded extraordinary oxidation resistance, as is apparent in from the weight change of the alloys after oxidation, as related in Table 3.I.

Table 3.I: Oxidation behavior of Al-packed Mo-3Si-1B at elevated temperatures

Material	Oxidation Temperature					
	732°C	1000°C	1100°C	1200°C	1300°C	1372°C
Uncoated Mo-3Si-1B	-427.46 (50 hr)	-247.01 (14 hr)	-367.35 (2.5 hr)	-277.89 (1.47 hr)	-320.48 (2.5 hr)	No Test
Al-packed Mo-3Si-1B	+0.01	+0.25	+0.27	+1.09	+2.35	+3.50

As the Al_2O_3 formed, a $Mo_3(Al,Si)$ containing approximately 30 vol.% Mo_5SiB_2, grew between the Mo_3Al_8 layer and the base material. The growth of this interlayer limited the availability of Al to heal any cracks that appeared, and thus the lifetime of the coating. Rioult, *et al*.[69] defined the lifetime of the coating as a complex function of the coating thickness (E), densities of the various layers (d_{Mo3Al8}, d_{Al2O3} & $d_{Mo3(Al,Si)}$), molar masses of the various constituents (M_{Mo3Al8}, M_{Al2O3} & $M_{Mo3(Al,Si)}$), the Al:Si ratio in the $Mo_3(Al,Si)$ phase (r), the proportion of $Mo_3(Al,Si)$ in the interlayer (F) and constants determined from the parabolic growth rates of the Al_2O_3 (A_x & E_{ax}) and $Mo_3(Al,Si)$ (A_y & E_{ay}) layers. Their model for the lifetime of an Al_2O_3 coating is given by:

$$t_{\text{lifetime}} = \left[7 \frac{E \times d_{\text{Mo}_3\text{Al}_8}}{M_{\text{Mo}_3\text{Al}_8}} \frac{1}{2\frac{d_{\text{Al}_2\text{O}_3}}{M_{\text{Al}_2\text{O}_3}}\sqrt{A_x\, exp\left(\frac{-E_{ax}}{RT}\right)} + \frac{r}{1+r} \times \frac{F \times d_{\text{Mo}_3(\text{Al,Si})}}{M_{\text{Mo}_3(\text{Al,Si})}}\sqrt{A_y\, exp\left(\frac{-E_{ay}}{RT}\right)}} \right]^2 \tag{3.2}$$

The calculated lifetimes for various coating thicknesses at various temperatures are given in Fig. 3.8. Below 950°C, the lifetime is expected to suffer as a result of the

formation of the less protective θ-Al_2O_3 phase. Under thermal cycling the lifetime of these coatings is also expected to decrease, as coefficient of thermal expansion mismatch can lead to cracking and spallation of the Mo_3Al_8 coating.[69] Despite these limitations, Al pack cementation has the potential to drastically improve the oxidation resistance of Mo-Si-B. The analysis by Rioult, *et al*.[69] suggested that a 100 μm thick Mo_3Al_8 coating could provide more than 1000 hours of enhanced oxidation resistance at 1300°C. This lifetime was further improved if a B-rich layer was formed on the base material before Al-pack cementation, as this layer inhibited diffusion of Al into the base material.[152]

Pack cementation of Si has also garnered[83, 89, 153, 154] interest[83, 89, 153, 154] as a means of improving the oxidation resistance of Mo-Si-B alloys. The process for creating an oxidation resistant coating is similar to the process used for Al pack cementation. A Mo-Si-B substrate was packed in a powder mixture of NaF (5 wt.%, to act as the halide activator), Si (25 wt.%, source material) and Al_2O_3 (70 wt.%, to act as filler material).[154] On heating to 900°C, Si reacted with NaF to form SiF_4 gas. This vapor interacted with the surface of the substrate and deposited a uniform layer of Si. This surface enrichment led to the *in-situ* formation of a $MoSi_2$ coating. $MoSi_2$ cannot exist in thermodynamic equilibrium with either α-Mo or Mo_3Si. As a result, an interlayer containing B-doped Mo_5Si_3 formed. When exposed to an oxidizing atmosphere, a SiO_2 scale formed on the outer surface of the coating, while the Mo_5Si_3 interlayer continued to grow. Boron atoms ejected during the transition of Mo_5SiB_2 to Mo_5Si_3(B) reacted with α-Mo grains to form particles of MoB.[155] Sakidja, *et al.*[154] have reported complete transformation of $MoSi_2$ to Mo_5Si_3 and SiO_2 after only 25 hours in air at 1300°C. Underneath the Mo_5Si_3 layer, a two-phase region of Mo_5SiB_2 and MoB formed. A similar effect was noted by Ito, *et al.*[89, 153] This two-phase region acted as a barrier to Si transport. As a result, the growth of the Mo_5Si_3 layer was halted. Boron was continuously supplied to the Mo_5Si_3 layer by the underlying Mo_5SiB_2-MoB layer, maintaining the protective capabilities of this layer. Ito, *et al.*[89, 153] reported no weight change for Mo-3.4Si-2.6B alloys tested at 1300°C and 1400°C for 50 hours. A slight weight gain was reported for tests performed at 1500°C for 50 hours, though slight weight loss was observed in a 100 hour test. Ito, *et al*.[89] also reported a slight degradation in the cyclic oxidation response of their material, though the slight weight loss was curtailed after 40 hours.

While this strategy has proven effective at protecting alloys with small volume fractions of α-Mo,[89, 153, 154] the Si pack used was less successful at protecting a Mo-3Si-1B alloy, as the B content of the base material was not high enough to cause the formation of a continuous Mo_5SiB_2-MoB layer.[154] Sakidja, *et al*.[154] proposed co-deposition of Si and B as a means to create a Mo_5SiB_2-MoB layer. The mechanics of such a deposition were explored further by Tang, *et al*.[83] They explored the oxidation resistance afforded by

deposition of Si, Si and B, or B then Si on a Mo-4Si-1B substrate. Si deposition resulted in a coating that transformed completely into Mo_5Si_3 after 12 hours' exposure at 1600°C. As a result, the sample was completely oxidized after only 50 hours at this temperature. Co-deposited B and Si resulted in the formation of a similar coating structure as the solely Si deposition, though the porosity of the coating increased with increasing B content. The coating was again completely transformed within 12 hours at 1600°C, and the sample was completely oxidized after 50 hours. The initial porosity of the coating was not thought to affect the long term oxidation behavior, as these pores were sealed by the oxide during the experiment. The two-step process formed a more complex coating. After the initial B deposition, a Mo_2B_5layer containing MoB particles was observed on the sample surface, while a Mo_5SiB_2-MoB layer formed between the outer coating and the substrate material. After the second step, the outer Mo_2B_5 layer had been converted into $MoSi_2$, while the Mo_5SiB_2-MoB interlayer had increased in thickness. This process was also unsuccessful at significantly improving the lifetime of a $MoSi_2$ coating at 1600°C. Though these deposition techniques were unable to extend the life of a $MoSi_2$ coating on Mo-4Si-1.1B at 1600°C, a lifetime on the order of thousands of hours was predicted for coatings oxidized at 1100°C. Si diffusion, and the resulting transformation of $MoSi_2$ into much less oxidation-resistant Mo_5Si_3, limits the lifetime of a $MoSi_2$ coating.

3.4 Mechanical Properties

Since Mo-Si-B alloys are potential candidates for next-generation ultra-high temperature structural materials, an understanding of the mechanical response of these materials both at room temperature and elevated temperatures is necessary. We will review the research on the mechanical properties of these alloys as pertains to creep, fracture and fatigue. Before this behavior can be properly examined, the high temperature tension, compression and bending behavior of these materials must be explored. We will focus on the behavior of α-Mo-$Mo_5SiB_2Mo_3Si$ alloys, as alloys consisting of only intermetallic phases (*i.e.* Mo_5Si_3-Mo_5SiB_2-Mo_3Si) are too brittle to act in load-bearing applications. As a result, very little research has been published on the mechanical properties of purely-intermetallic phase constructions.[81] α-Mo is a required component if any significant ductility is desired, as very few dislocations, and thus very little plasticity can be realized in the highly-ordered intermetallic phases (*cf.* Sections 3.1.1.2-4).

3.4.1 Tension, Compression and Constant Load Creep

Only a few studies of the basic tension, compression or bending behavior of Mo-Si-B alloys at elevated temperatures have been published.[9, 10, 14, 15, 94, 114, 133-136] The elastic

constants of a Mo-4Si-1B alloy, as determined by FEM simulation and confirmed by the resonant beam technique as shown in Table 3.II.[133]

Table 3.II: Elastic Constants of Mo-4Si-1B at 24°C-1200°C

Temperature (°C)	E (GPa)	G (GPa)	K (GPa)	ν
24	325	125	252	0.285
300	313	121	248	0.289
600	298	115	241	0.294
900	284	109	241	0.304
1200	269	102	239	0.312

Nieh, *et al*.[114] published the first tensile data for a α-Mo-Mo_5SiB_2-Mo_3Si alloy. The authors examined the high temperature deformation behavior of a 3-phase, α-Mo-rich Mo-3.4Si-1.9B alloy manufactured by hot-pressing blended elemental powders. The resulting alloy contained ~ 50 vol.% α-Mo as a continuous matrix phase containing a fine dispersion of intermetallic phases. The grain size of all phases was ~ 3 μm. The authors observed marked temperature and strain rate sensitivities for their alloy. At 1400°C, a peak stress of 222 MPa and a tensile elongation of 150% were recorded at a strain rate of 10^{-4} s^{-1}, while the peak stress at a strain rate of 10^{-3} s^{-1} were 480 MPa and 23%, respectively. A significant strength decrease was observed at 1450°C, peak stresses of 138 MPa at a strain rate of 10^{-4} s^{-1} and 275 MPa at a strain rate of 10^{-3} s^{-1}, while elongation to failure increases were noted at some strain rates. The authors attributed this behavior a combination of creep of the α-Mo phase and grain boundary sliding. Plastic deformation of the α-Mo phase accommodated grain boundary sliding of the intermetallic phases without the formation of cavities. For their material, Nieh, *et al.*[114] reported a stress exponent, $n = 2.8$ (highlighting the combined influence of grain boundary sliding ($n = 2$) and creep of α-Mo ($n = 5$)) and an activation energy of 740 kJ/mol. Similar behavior, in compression, has been observed by Mitra, *et al*. for a Mo-5Si-1.4B alloy, [107, 108] though the higher strength retention at high temperatures reported by Mitra, *et al*. is attributable to the lower α-Mo content in their alloy (33 vol.%, distributed as discontinuous particles in an intermetallic matrix).

The remarkable high temperature deformation behavior observed by Nieh, *et al*.[114] has also been observed by Jéhanno, *et al*.[134, 135] for their Mo-3Nb-3Si-1B mechanically-alloyed material. Nb was added as a solid solution strengthening agent for the α-Mo phase. Like Nieh, *et al.*,[114] the material tested by Jéhanno, *et al*.[134, 135]contained a continuous α-Mo matrix, though the volume fraction of α-Mo in the Jéhanno material was slightly higher (55 vol.%). However, the grain size in the Jéhanno material was even smaller than that of the Nieh material. Jéhanno, *et al.*[134, 135] reported

submicron grain sizes for all three phases present in their material. At 1400°C and a strain rate of 10^{-4} s^{-1} a maximum stress of 45 MPa and a plastic strain to failure of ~ 400% were reported.[135] Unlike the Nieh material, substantial plasticity was observed at faster strain rates at 1400°C (200% elongation at a strain rate of 10^{-3} s^{-1} and 25% elongation at a strain rate of 10^{-2} s^{-1}). In fact, more than 300% elongation was observed at 1300°C at a strain rate of 10^{-4} s^{-1}.[135] This result is noteworthy, as the alloys tested by Jéhanno, *et al*.[134, 135] and Nieh, *et al*.[114] both contain ~50 vol.% brittle intermetallic phases. After deformation, all phases remained in the submicron range as equiaxed grains, satisfying the requirements of superplasticity[156] as a potential deformation mechanism. Jéhanno, *et al*.[135] reported a stress exponent n = 2.3 and an activation energy of 470 kJ/mol. The authors credit bulk diffusion of Mo atoms, as evidenced by their observed activation energy for deformation (the activation energy of Mo self-diffusion is 405 kJ/mol[157]), for maintaining grain cohesion during plastic deformation.

Similar behavior in compression, though at significantly slower strain rates, was noted by Alur, *et al*.[98] and Kumar and Alur[101] for a Mo-2Si-1B two-phase powder-processed alloy containing an α-Mo matrix surrounding an α-Mo-Mo_5SiB_2 eutectic. These alloys were isothermally forged at 1760°C and compression samples were cut such that the long axis of the sample (*i.e.* the compression direction) matched the forging direction. Between 25°C and 800°C, the material was found to be relatively insensitive to strain rate in the range 10^{-7}-10^{-4} s^{-1}. The flow stress in this regime (~1100 MPa) was found to compare favorably with the room temperature yield stress (1280 MPa). Above 1000°C a significant strength drop and increase in strain rate sensitivity was observed. At 1000°C yield strengths between 790 MPa (at a strain rate of 10^{-4} s^{-1}) and 320 MPa (at a strain rate of 10^{-7} s^{-1}). At 1400°C the yield strength had fallen to 130 MPa and 15 MPa for strain rates of 10^{-4} s^{-1} and 10^{-7} s^{-1} respectively. Very similar yield strengths were reported for a three phase Mo-2.9Si-1.1B alloy consisting of an α-Mo matrix interspersed with intermetallic phases. At 1000°C, the material had a stress exponent n = 7.1, which was unaffected by strain rate. At 1400°C, the stress exponent had fallen to n = 5.2 for strain rates as slow as 10^{-5} s^{-1}. Below this strain rate a possible shift in deformation mechanism was observed, as the stress exponent in this regime was reported as n=2.5. Activation energies in the range 415-445 kJ/mol were reported for all test conditions, again implying self-diffusion of Mo as an important deformation mechanism. The high yield strengths of these materials, especially at lower temperatures, were at least partially attributable to the high initial dislocation densities in these materials as a result of the forging process.

FEM simulations performed by Alur, *et al*.[98] help to elucidate the deformation mechanisms in this temperature/strain rate regime. Assuming an elastic-plastic matrix and an elastic intermetallic phase, Alur, *et al*.[98] found a high degree of strain localization

in the matrix phase. At low temperatures, the matrix phase was highly strained, while the Mo_5SiB_2 phase was relatively unstrained. This behavior was the result of the comparatively low yield stress and high work hardening rate of the matrix phase. In this situation, the applied deformation was accommodated by plastic deformation of the matrix. At the lowest temperatures and highest strain rates cracking of Mo_5SiB_2 particles was observed, highlighting the inability of this phase to accommodate strain. At high temperatures the strains were more homogeneously distributed. A significant decrease in the strain level in each phase was achieved by allowing plastic deformation of the intermetallic phase. This shift in modeling behavior was justified by the presence of dislocations in the post-deformation Mo_5SiB_2 phase. Deformation was accommodated by both the matrix and the intermetallic phase. This behavior is highlighted in Fig. 9.

The importance of the matrix phase on the mechanical response of Mo-Si-B alloys was confirmed by Jéhanno, *et al.*[94] They examined the tensile response of two Mo-3Si-1B alloys. One alloy, consolidated from rapidly solidified gas atomized powders, was comprised of an intermetallic matrix surrounding large α-Mo particles. The second alloy, consisting of a continuous α-Mo matrix surrounding small intermetallic particles, was created by a 6:1 extrusion at 1800°C. A higher volume fraction of α-Mo was observed in the extruded material, but only one measurement was taken from each alloy condition, so this effect may be an artifact. All intermetallic-matrix samples tested in tension at an initial strain rate of 1.1×10^{-4} s^{-1} failed in a brittle manner below 1200°C. At 1200°C some measureable plasticity at failure (7.3% elongation) was observed. The brittle-ductile transition temperature for the intermetallic-matrix alloy was estimated to be ~1150°C. By contrast, significant plasticity (21.5% elongation) was found in the extruded, α-Mo-matrix material at 1093°C. The authors estimated the brittle-ductile transition temperature of the extruded material to be ~ 950°C-1000 °C, a drop of ~200°C. It is likely that some of the strength gain observed after extrusion was a result of the increased initial dislocation density of the post-extrusion material.

Implementation of a continuous α-Mo can greatly affect the brittle-ductile transition temperature for Mo-Si-B alloys. Krüger, *et al.*[14] developed ultra-fine grained (grain size ~ 1 μm) 3-phase Mo-3Si-1B alloys via mechanical alloying, as described in Section 3.2 In bending, the authors were able to achieve at least 8% strain at 1000°C, matching the behavior exhibited by the extruded material tested by Jéhanno, *et al.*[93] By contrast, the intermetallic-matrixed gas-atomized material required temperatures in excess of 1200°C to accomplish the same result. A cast and annealed, intermetallic-matrixed, Mo-4.2Si-1.1B alloy, containing ~40 vol.% discontinuous α-Mo exhibited negligible ductility, even at 1520°C and a strain rate of 7×10^{-6} s^{-1} in flowing nitrogen.[84] Meanwhile, an α-Mo-matrixed Mo-2.2Si-1B powder-processed alloy containing ~49

vol.% continuous α-Mo achieved a fracture strain of 1.8% at 1200°C *in vacuo* at a much faster loading rate (3.3×10^{-3} s^{-1}).[116]

Grain size reduction also has the potential to increase the ductility of Mo-Si-B and lower the brittle-ductile transition temperature. α-Mo, as a bcc metal, is highly susceptible to cleavage fracture. High stresses ahead of a dislocation pileup can initiate a cleavage failure. If the grain size is reduced to such a degree that a sufficient dislocation pileup cannot form, failure by cleavage will not occur and ductility can be realized at lower temperatures. With this framework in mind, a number of oxide dispersions have been utilized[9, 11, 25-29] to pin grain boundaries and limit grain growth during processing. The effects of $MgAl_2O_4$ spinel additions were discussed in Section 2.1. Jéhanno, *et al*.[11] observed substantial reduction in the brittle-ductile transition temperature with the addition of 0.1wt% Y_2O_3 or La_2O_3 to a Mo-3Si-1B alloy, though the alloy to which their data was compared does not have a continuous α-Mo matrix. It is difficult, as a result of the test method they chose, to separate the effects of a continuous α-Mo from the effects of a reduced grain size. The authors measured the brittle-ductile transition temperature by compressing cylinders until 10% plastic strain was reached. Large (100°C) temperature steps were used, so identification of a precise brittle-ductile transition temperature was not possible. As a result, the added benefit of a reduced grain size for the studied materials, as pertains to the brittle-ductile transition, is unclear. However, the work of Heilmaier, *et al*.[9] clearly shows the benefit of a submicron grain size as 8% plastic strain (the chosen benchmark for ductility) was reached for a mechanically-alloyed, submicron-grained Mo-3Si-1B alloy at 1000°C, while negligible ductility was observed for a micron-grained, La_2O_3-doped alloy. The reported low strength and ductility of the La_2O_3-doped alloy seems to contradict the results of Jéhanno, *et al*.[11] for the exact same material, but no explanation was given by the authors for this discrepancy.[9]

Alloying additions such as Zr have been shown[136] to affect the brittle-ductile transition temperature of Mo-3Si-1B and Mo-1.9Si-0.6B. Krüger *et al*.[136] observed significant plasticity in bending at 954°C at a displacement rate of 0.01 mm/min in Ar. While a micron-grained Mo-3Si-1B alloy exhibited ~0.5% strain in these conditions, a Mo-3Si-1B-1Zr alloy exhibited ~1.5% strain. At lower Si and B content, this effect was magnified. At 954°C, a Mo-1.9Si-0.6B-1Zr exhibited ~4% strain compared to the ~0.5% strain displayed by the Zr-less material. Limited plasticity was observed in the Mo-1.9Si-0.6B-1Zr material at temperatures as low as 800°C. The authors postulate that the brittle-ductile transition temperature of continuous α-Mo-matrixed Mo-Si-B materials can be reduced another 150°C with the addition of Zr.[136]

Mo-Si-B alloys are potential replacements for current Ni-based superalloys because, among other beneficial properties, they demonstrate excellent creep resistance

and strength retention at high temperatures. A number of studies on the creep behavior of these materials have recently been published.[9, 10, 18, 100, 134, 140, 141, 158, 159] The effects of creep on crack growth studied by Alur, *et al*.[100] will be withheld until the discussion of high temperature fracture toughness and fatigue in Sections 3.4.2 and 3.4.3.

Schneibel and Lin[159] measured the creep response of a cast Mo-4.2Si-1.1B alloy at 1200°C in flowing Ar. Owing to insufficient gettering of the Ar environment, oxidation of the material occurred during testing. MoO_3 crystals deposited on the quartz window used for laser extensometry of the sample. As a result, the authors were only able to successfully test one sample in tension. Compression tests were also performed in flowing Ar at temperatures between 1220°C and 1420°C. A steady-state creep stress was determined from the flow stress at 5% plastic strain. The activation energy (338 kJ/mol) and stress exponent (n = 2.7) were insensitive to temperature or strain rate. The power-law creep equation developed by Schneibel and Lin[159] is given by Eq. 3.3:

$$\dot{\varepsilon} = 2.2 \times 10^{14} s^{-1} (\sigma/E)^{2.7} exp([-338 kJ/mol]/RT) \qquad (3.3),$$

where E is the room temperature Young's modulus of this material, 327 GPa.[80] The authors claim Mo_3Si as the rate-controlling phase, since the calculated creep rate for single phase Mo_3Si using the compression data of Rosales, *et al*.[34] compares favorably to the observed behavior. However, the relatively low volume fraction of this phase (32 vol.%) implies a contribution from the Mo_5SiB_2 phase (30 vol.%). α-Mo was not thought to be rate controlling.

Schneibel[158] probed the effects of Nb and W alloying additions on creep response of Mo-X(Nb,W)-4.2Si-1.1B between 1200°C and 1400°C. He identified the creep stress as the compressive engineering flow stress at 2% plastic deformation. For an unalloyed material, Schneibel[158] reported a stress exponent of 3.2 and an activation energy of 295 kJ/mol. Addition of 36.7 wt.% (19.5 at.%) W was found to only slightly raise the activation energy to 319 kJ/mol. Nb had a much stronger effect on the creep behavior. While the stress exponent was unaffected, the addition of 11 wt.% (9.5 at.%) or 22.7 wt.% (19.5 at.%) Nb raised the activation energy to 345 kJ/mol or 489 kJ/mol, respectively. The potency of Nb was attributed to its much larger atomic radius than either Mo or W. As a result of its larger size, Nb was postulated to inhibit diffusion and dislocation motion. The effect of Nb and W on the creep behavior of Mo-4.2Si-1.1B is highlighted in Fig. 10.

In the same work, Schneibel[158] investigated the influence of microstructural morphology and scale on the creep behavior of Mo-6.1Si-1.1B and Mo-4.9Si-1.5B. Two Mo-6.1Si-1.1B alloys (21 vol.% discontinuous α-Mo) with differing α-Mo grain sizes were manufactured. The Mo-4.9Si-1.5B alloy contained ~30 vol.% continuous α-Mo as

achieved using the process described by Schneibel *et al.*[115] Both microstructural scale and grain morphology were observed to have a profound effect on the creep behavior in the studied temperature regime. A detectable increase in the stress exponent (n = 2.8 versus n =2.1 for the finer microstructure) and decrease in the activation energy (327 kJ/mol versus 376 kJ/mol) at 1300°C were observed for the coarser-grained of the two Mo-6.1Si-1.1B alloys. Likewise, a significant increase in the stress exponent (n = 3.9) and decrease in activation energy (328 kJ/mol) were observed for the continuous α-Mo Mo-4.9Si-1.5B alloy, though the reported values were calculated at 1400°C. α-Mo was the softest phase at these temperatures. As a result, the higher volume fraction in the Mo-4.9Si-1.5B material led to lower creep strength. Similarly, the continuity of the α-Mo phase in this material lowered the creep strength as plastic deformation of this phase was not as constrained. Finer microstructures provided more high diffusivity pathways, speeding diffusion of Mo, and thus lowered the creep resistance of the material.[140, 141, 158] The combined effects of α-Mo volume fraction and continuity are shown in Fig. 11.

Though the ultra-fine grained materials developed via mechanical alloying exhibit attractive oxidation resistance and formability, the preponderance of grain boundaries in these materials was expected to harm their creep resistance.[134] Jéhanno, *et al.*[134] studied the effect of microstructure size scale on the constant stress compression behavior of an ultra-fine grained Mo-3Nb-3Si-1B alloy between 1050°C and 1315°C. In order to assess the influence of grain size, both as-processed (submicron grains) and annealed (~7 μm α-Mo grains, ~ 4 μm intermetallic grains) samples were tested. Anneals at 1700°C for 10 hours were required to sufficiently coarsen the microstructure. The authors found that the stress exponent for each microstructure was approximately n = 2, indicating grain boundary sliding as a possible creep mechanism. The activation energies for each microstructure were also similar (477 kJ/mol for the as-processed alloy, 444 kJ/mol for the annealed material), again implying the role of Mo diffusion in the high temperature deformation behavior of Mo-Si-B alloys, as reported by Alur, *et al.*,[98] Kumar and Alur[101] and Jéhanno, *et al.*[135] Though the mechanism and activation energy for creep was similar for the as-processed and annealed microstructures, the coarser-grained annealed alloy exhibited a creep rate that was more than one order of magnitude slower than the ultra-fine grained material. Similar behavior to the ultra-fine grained material was reported by Heilmaier, *et al.* [9, 10] for La_2O_3-doped Mo-3Si-1B alloys. It should be noted that the alloys tested by Heilmaier, *et al.*[9, 10] compared very favorably with a Ni-based single crystal alloy, CMSX-4 below 1100°C and vastly outperformed the Ni alloy above 1200°C [9, 10]. Thermal instability of the CMSX-4 above 1200°C, coupled with the excellent thermal stability of Mo-3Si-1B up to 1600°C, was thought to be the origin of the Mo-Si-B alloy's superior creep resistance.

The most comprehensive study of the creep behavior of Mo-Si-B alloys was recently published by Jain and Kumar.[18] Their work on a Mo-0.9Si-0.2B material meant to represent the α-Mo solid solution phase was reviewed in Section 2.1. The authors also investigated the tensile load creep behavior of Mo-2Si-1B two-phase and Mo-3Si-1B three-phase alloys between 1000°C and 1300°C at both constant load and at a strain rate of 10^{-4} s^{-1}. Below 1200°C both the two- and three-phase alloy fractured after very little detectable plasticity. Above 1200°C no substantial difference between the creep behaviors of the two- and three-phase alloy was reported. For both materials a stress exponent $n = 7$ was calculated at 1200°C when the tensile data of Jain and Kumar[18] and the compression data of Alur, *et al.*[98] were combined to increase the range of strain rates examined. Creep voids did not form until very late in the creep lifetime. As a result, the creep behavior in tension and compression was assumed to be nearly identical and the results from tension and compression tests could be combined. At 1300°C a stress exponent $n = 4.6$ was reported for both multi-phase alloys, though a stress exponent could not be extracted from the 1300°C tension tests, as a lack of material prevented sufficient data from being collected. Mo_5SiB_2 particles were observed as grain boundary precipitates in samples tested above 1200°C. The quantity and coarseness of these particles was found to scale with temperature and applied stress. The authors postulated that the formation of these precipitates served to relieve the grain boundary Si and B segregation observed in the as-processed alloy. This reasoning was bolstered by the lack of any precipitates within grains or on recrystallized grain boundaries that formed during the experiment (and thus would not be sites of Si or B segregation). The formation of Mo_5SiB_2 occurred both in the gage section and within the grip section of the samples, implying that stress (and thus plastic strain) was not required for precipitation, though the application of stress did speed their coarsening. The higher Si content (and thus higher strength) of the matrix phase of the multiphase alloys, as well as the much higher volume fraction of intermetallic phases, were credited for providing the superior creep resistance of the two- and three-phase alloys. The alloys tested by Jain and Kumar[18] also outperformed Ni-based alloys over the temperature and stress regime investigated.

3.4.2 Toughness

While many researchers have performed toughness tests on Mo-Si-B alloys (*cf.* Appendix), only a few have investigated the operative fracture mechanisms in these alloys. We will discuss the fracture behavior of these alloys as both room temperature and elevated temperature. While the proposed operating temperature for these alloys exceeds 1200°C, it is unrealistic to think that fracture events cannot occur at low temperatures. In any event, the high brittle-ductile transition temperature for these materials means that the brittle behavior observed at room temperature will persist

until at least 1000°C, and possibly higher, depending on the alloy choice and grain morphology.

At room temperature, Mo-Si-B alloys are inherently brittle. The high intermetallic content required for good oxidation resistance, coupled with solid solution strengthening of the α-Mo phase, limits the ability of these alloys to plastically deform. As a result, these materials exhibit low room temperature toughnesses. α-Mo incorporated into an intermetallic matrix as a second phase can allow some room temperature plasticity, but the volume fraction and distribution of α-Mo greatly affects the fracture behavior of Mo-Si-B alloys. As a crack extends, it will encounter a region of α-Mo. At this softer phase, the crack can become blunted and trapped, increasing the so-called *intrinsic toughness* of the material.

Toughening in materials can be considered as a mutual competition between intrinsic and extrinsic mechanisms. *Intrinsic* toughening mechanisms dominate in ductile materials; they operate ahead of the crack tip to generate resistance to microstructural damage, with the most prominent mechanism being that of plastic deformation. *Extrinsic* toughening mechanisms, conversely, operate primarily in the wake of the crack tip to inhibit cracking by "shielding" the crack from the applied driving force.[160-163] Whereas intrinsic toughening mechanisms are effective in inhibiting both the initiation and growth of cracks, extrinsic mechanisms, such as crack bridging, are only effective in inhibiting crack growth.[161-163]

Uncracked ligament bridging to serves to increase the toughness as the crack grows. As a crack extends, it can encounter a more ductile α-Mo grain. Depending on the relative toughnesses of the phases, their relative elastic moduli and the angle of crack incidence, the crack will penetrate the α-Mo grain (and fracture the grain transgranularly) or deflect into the grain boundary and propagate around the grain.[164] This deflection event raises the perceived toughness of the material, as the preferred microstructural path no longer coincides with the direction of maximum driving force. As a result, more stress must be applied to continue crack propagation. At some point the crack must either propagate "backwards" up the flank of the grain, or it will stall, creating a highly stressed region in the proximity of the crack tip.[165] As the remotely-applied stress (and thus the local stresses near the crack tip) is increased, a region ahead of the crack tip can become stressed enough that the crack will reinitiate and continue propagating (Fig. 12). This process leaves behind an uncracked ligament which can carry load and shields the crack tip from the full extent of the remotely applied stress. As the crack extends, more bridges are left in the wake, increasing the shielding effect.

3.4.2.1 Room Temperature

The room temperature fracture behavior of Mo-Si-B alloys has been thoroughly investigated by Choe, *et al*.,[78, 79, 85] Kruzic, *et al*.[116-118] and Alur, *et al*.[99] for various alloy compositions, phase distributions and processing methods. Choe, *et al*.[85] studied the room temperature fracture behavior of two cast alloys (Mo-4.2Si-1.1B and Mo-12.1Nb-4.2Si-1.1B) and two hot-pressed powder alloys (both Mo-6.1Si-1.2B, differing starting powders). The cast alloys contained 38 vol.% discontinuous α-Mo as a second phase in an intermetallic matrix. The powder processed alloys contained 21 vol.% discontinuous α-Mo. The average grain size of the cast alloys (10.4 μm for Mo-4.2Si-1.1B, 7 μm for Mo-12.1Nb-4.2Si-1.1B) was significantly larger than the powder alloys (2.14 μm and 4.4 μm), though the coarser grained powder processed alloy contained a number of elongated 50 μm grains. The authors performed fracture toughness experiments, as per the ASTM E561 standard[166] using fatigue pre-cracked disk-shaped tension specimen. Stable crack growth was measured *in-situ* utilizing the unloading compliance technique prescribed by the testing standard. Stable crack growth and the accompanying rise in toughness were used to create crack growth resistance curves.

The authors found that the initiation toughness of their alloys scaled with mean grain size and volume fraction and contiguity of the α-Mo phase. The highest initiation toughness, K_o = 7.2 MPa√m, was exhibited by the Mo-4.2Si-1.1B alloy, which had the largest and most continuous grains. This alloy exhibited a slight rise in toughness with crack extension. After 800 μm of crack growth, a peak (plateau) toughness of K_{ss} = 7.8 MPa√m was reported. The finer-grained Mo-12.1Nb-4.2Si-1.1B alloy exhibited lower initiation (6.3 MPa√m) and peak (6.7 MPa√m) toughnesses. Both powder-processed alloys displayed significantly lower initiation toughnesses (5.7 MPa√m for the larger-grained alloy, 4.3 MPa√m for the smallest-grained, least continuous material) and no stable crack growth was observed. In fact, the authors were unable to fatigue-pre-crack the smaller-grained material, so the value reported for that alloy was over-estimated.

Fracture at room temperature in these materials is brittle and occurred mostly by transgranular cleavage of the intermetallic matrix. The crack predominately travelled through the intermetallic matrix or within the grain boundaries surrounding the α-Mo phase. Cracks were observed to deflect around or crack through small α-Mo regions, but became trapped at larger α-Mo grains. A small number of unbroken α-Mo grains were found in the crack wake, but these uncracked ligaments displayed minimal plastic deformation, which the authors attributed to plastic constraint of the α-Mo grains by the intermetallic matrix. The dominant toughening mechanism reported for these intermetallic-matrixed materials was crack trapping, an *intrinsic* toughening mechanism.

While Choe, *et al*.[85] showed the influence of grain size, volume fraction of α-Mo and the contiguity of the α-Mo phase, they did not study the effects of a continuous α-Mo-matrixed material. Kruzic, *et al.*[117] developed R-curves for a number of alloys with varying α-Mo volume fractions and grain sizes. All of the alloys tested consisted of intermetallic second phases distributed within a continuous α-Mo matrix, as the processing method developed by Schneibel, *et al*.[115] can produce a continuous α-Mo phase, even at very low volume fractions of α-Mo. The authors varied both the initial starting size ("fine" = <45 μm, "medium" = 45-90 μm, "coarse" = 90-180 μm) of their vacuum-anneal Mo-7.6Si-1.5B powders and the volume fraction of α-Mo in their "coarse" alloy (17 vol.%, 46 vol.% and 49 vol.%). Utilizing the notation of Kruzic, *et al.*,[117] the alloys are labeled F34, M34, C17, C46 and C49 where the letter represents the initial powder size and the number represents the volume fraction of α-Mo.

All of the alloys tested by Kruzic, *et al*.[117] exhibited significant rising R-curve behavior, with the largest degree of toughening with crack extension observed for the coarse-grained materials. While the C17 alloy had an initiation toughness (K_o =~5 MPa√m) comparable to the discontinuous α-Mo alloys studied by Choe, *et al*.,[85] after 3 mm of crack extension, the peak toughness of the C17 alloy had increased to ~7 MPa√m, a much larger increase in toughness than exhibited by the alloys studied by Choe *et al*.[85] which contained twice as much α-Mo, though distributed as a discontinuous second phase. The alloys containing a similar volume fraction of α-Mo as the work of Choe, *et al*.,[85] namely F34 and M34, exhibited similar initiation toughnesses (~7.5 MPa√m), but the increase in toughness with crack extension (K_{ss} = ~ 9 MPa√m) was significantly greater than seen by Choe, *et al*.[85] The high volume fraction α-Mo materials exhibited initiation toughnesses as high as 12.5 MPa√m and peak toughnesses in excess of 20 MPa√m after 3 mm of crack extension, as shown in Fig. 13. The values reported by Kruzic, *et al*.[117] are the highest reported room-temperature toughnesses for any Mo-Si-B alloy.

The transition to a continuous α-Mo matrix greatly improved the room temperature toughness. Crack trapping remained an important toughening mechanism, however, bridging by uncracked α-Mo ligaments occurred much more frequently, and provided *extrinsic* toughening and thus rising R-curve behavior. As shown in Fig. 14, cracks cannot avoid a continuous α-Mo phase, so the effectiveness of crack trapping and uncracked ligament bridging is improved when an α-Mo matrix is utilized. A larger volume fraction of α-Mo provides more traps and potential crack-bridging sites, so both the initiation toughness (as the result of more plasticity) and the peak toughness (as the result of more *extrinsic* toughening) will increase.

When comparing alloys with the same volume fraction of α-Mo but differing microstructural size scales, it becomes apparent that grain size had little effect on the

initiation toughness. Both the F34 and M34 alloys tested by Kruzic, *et al*.[117] had initiation toughnesses K_o = 7 MPa√m, similar to the initiation toughness of the cast material tested by Choe, *et al*.[85] While little difference was observed for the initiation toughnesses of these materials, a higher peak toughness at a larger crack extension was reported for the M34 alloy, implying an increased level of *extrinsic* toughening in that material. Kruzic, *et al*.[117] reported improved crack stability and easier bridge formation for coarser-grained alloys. That the authors were able to achieve significant stable crack growth accompanied by rising toughness in a coarse-grained alloy containing only 17 vol.% α-Mo highlights the influence of microstructural size scale on the rising R-curve behavior of these alloys.

Alur and Kumar[99] observed limited room temperature ductility and no rising R-curve behavior for their isothermally-forged Mo-2Si-1B alloys. Even though the volume fraction of α-Mo in the materials studied by Alur and Kumar[99] was even larger (62 vol.% α-Mo) than any of the materials studied by Kruzic, *et al*.[117] the initiation toughnesses observed by Alur and Kumar[99] were lower than those reported by Kruzic, *et al*.[117] The largest initiation toughness observed by Alur and Kumar[99] was only 9 MPa√m for an annealed alloy. The more brittle behavior and lack of extrinsic toughening observed for these materials can be attributed to the differing processing methods used to create the two materials. The powders used by Kruzic, *et al*.[117] have been processed in such a way as to create regions of α-Mo nearly free of Si. By contrast, the alloys used by Alur and Kumar[99] contained as much as 4 at.% Si within the grains and 12 at.% within the grain boundaries.[18] Since Si is a well-known solid solution strengthener and embrittling agent of Mo grain boundaries, the lower toughness observed by Alur and Kumar[99] was not unexpected. The presence of some recrystallized grains in these two-phase materials served to further embrittle the materials, since recrystallized Mo grain boundaries are weaker.

The work of these researchers clearly shows the influence of microstructure on the room temperature damage tolerance of Mo-Si-B alloys. A continuous α-Mo matrix imparts the highest toughness via two means: (1) a highly contiguous α-Mo phase increases the probability of a crack interacting with the more ductile α-Mo phase, increasing the incidence of crack trapping and ductile ligament bridging and (2) though it is possible to create a continuous α-Mo matrix with a small volume fraction of α-Mo,[115] the most common processing methods result in high α-Mo volume fractions. The high volume fraction of relatively ductile α-Mo increases both the crack initiation and crack growth (*i.e. extrinsic*) toughness.

3.4.2.2 Elevated Temperature

At elevated temperatures, the toughness of these alloys is significantly improved. As noted in Section 3.4.2, the ductile-brittle transition temperature of these alloys can be lowered by ~150°C by transitioning to a continuous α-Mo matrix. The ability of the α-Mo phase to plastically deform is drastically increased at elevated temperatures. As a result, the crack trapping ability of the material is much improved. Choe *et al.*[85] observed a sizeable increase in the initiation toughness of both their cast and their powder-processed alloys. At 1300°C the cast alloy exhibited an initiation toughness K_o = 9.7 MPa√m versus K_o = 7.2 MPa√m at room temperature. The powder processed alloys exhibited lower toughnesses at both room and elevated temperatures (K_o = 4.1 MPa√m and 5.7 MPa√m at room temperature, 8.1 MPa√m and 7.5 MPa√m at 1300°C), though this effect was likely the result of the lower volume fractions and contiguities of the α-Mo phase in the powder processed alloys. At elevated temperatures, significant microcracking was observed in the Mo_5SiB_2 phase. Microcracking, and the associated dilatation, acts as an additional crack-tip shielding mechanism, as the compressive forces caused by the microcracked region must be overcome before the critical stress to fracture the material can achieved.[163] The additional toughening effect afforded by microcracking of Mo_5SiB_2 is relatively small (~ 2 MPa√m from the dilatation of the microcracked region, ~1 MPa√m from the change in compliance as a result of the microcracks[85]) but noticeable.

A much larger increase in toughness was observable for α-Mo-matrixed alloys. Kruzic, *et al.*[117] found that the initiation toughness of a coarse grained (~100 μm grains) Mo-3.3Si-1.3B alloy increased from 9.8 MPa√m at room temperature to ~35 MPa√m at 1300°C, though the value reported for elevated temperature was valid for a plane stress condition, and is not directly comparable. In fact, the increase in ductility of the α-Mo phase at 1300°C was so profound that linear elastic fracture mechanics (*i.e.* the *K*-based approach) no longer applied and the *J*-integral approach (nonlinear elastic fracture mechanics) had to be used. After their tests were completed, the authors optically measured the crack tip opening displacement (CTOD) at crack initiation. Using the method detailed by Shih,[167] Kruzic *et al.*[117] calculated a J_{IC} which they then converted to an equivalent K_{JC} value which would have been observed had a sample large enough to satisfy the applicability requirements for linear elastic fracture mechanics been used. Again, the continuous α-Mo matrix forces the crack to interact with the ductile phase. The increased ductility of α-Mo at 1300°C increases the effectiveness of crack trapping. Similar to the observation at room temperature, a coarse microstructure increases the effectiveness of crack bridging at elevated temperature.

Alur and Kumar[99] observed similar behavior at elevated temperatures for their Mo-2Si-1B two-phase powder-processed alloy. The reported initiation toughnesses for

their alloy rose from ~9 MPa√m at room temperature to 25 MPa√m at 1400°C in vacuum, with the largest gains in toughness observed over the 1200°C (18 MPa√m)-1400°C (25 MPa√m) regime. At 1400°C, the authors observed a large amount of microcracking of the Mo_5SiB_2 phase not seen at room temperature. The authors also observed a much more tortuous crack path at 1400°C. The crack deflections were thought to be the result of the formation of a microcracked region ahead of the crack tip.

Alur, *et al.*[100] observed that the initiation toughness in three-point bending exhibited some loading rate sensitivity at elevated temperatures. While the initiation toughness increased monotonically with temperature at a loading rate of 10^{-3} mm/s, a toughness maximum was observed at 1200°C at a loading rate of 10^{-5} mm/s. The lower toughness at 1400°C than observed at 1200°C was attributed to creep cavitation and grain recrystallization. The much longer exposures to temperature at the slower loading rate (525 minutes to test at 10^{-5} mm/s versus 12 minutes to test at 10^{-3} mm/s) lead to creep effects like grain boundary sliding (and thus creep cavities). These cavities provide a preferred microstructural path, reducing the initiation toughness. Cavities form on recrystallized grain boundaries, which are known to be weaker. Plastic constraint by the hard metallic particles and the presence of silica were also proposed mechanisms for creep cavity formation. While creep effects were detrimental to the initiation toughness at 1400°C, at lower temperatures where creep cavitation does not occur creep can relax the local stresses at the crack tip, increasing the toughness.

3.4.3 Fatigue

Since Mo-Si-B alloys are toughened extrinsically, fatigue of these alloys is governed by degradation of the effectiveness of these mechanisms under cyclic loading. Specifically, early fatigue behavior consists of the rapid formation of many uncracked bridging ligaments. Continued cyclic loading causes a breakdown of some bridges, while new bridges form as the crack extends. Eventually a steady-state behavior is reached, where a dynamic zone of bridge formation and destruction is carried along with the growing crack. Near the end of the fatigue life, bridge destruction far outstrips bridge formation and failure proceeds rapidly. An example of this mechanism is illustrated in Fig. 15, though the bridge depicted is a rarely-formed intermetallic bridge. The mechanism operates in the same manner for α-Mo bridges. As a result of the brittle mechanisms for fatigue crack growth the fatigue thresholds and Paris law exponents ($da/dN \propto \Delta K^m$) for Mo-Si-B alloys are quite large, especially at room temperature. Thus the majority of the fatigue lifetime of these alloys is spent initiating a flaw that quickly grows to a critical size. Increased α-Mo ductility provides more extrinsic toughening, and thus slows crack growth and improves the fatigue resistance of these materials. However, increased α-Mo ductility leads to increased susceptibility

to fatigue, as the plastic deformation required for the typical fatigue-crack growth mechanism can occur more readily.

3.4.3.1 Room Temperature

Only a few researchers have studied the fatigue crack-growth behavior of Mo-Si-B alloys. Choe, *et al.*[85] investigated the tension-tension fatigue crack growth behavior of their cast Mo-4.2Si-1.1B and powder-processed Mo-6.1Si-1.2B alloys under stress-intensity control (K-control) at a load ratio (maximum load/minimum load) of $R = 0.1$ and a testing frequency of 25 Hz. The authors obtained crack growth rates, da/dN, between 10^{-11} and 10^{-5} m/cycle under K-increasing and K-decreasing conditions, with a normalized K-gradient of ±0.1 mm^{-1}, as per ASTM Standard E647.[168] Since these materials are very brittle, they exhibit a higher sensitivity to the maximum stress intensity at the fatigue threshold, $K_{max,th}$ than ΔK.[163] As a result, $K_{max,th}$ values were deemed more appropriate for gaging the fatigue resistance of Mo-Si-B alloys. The two quantities can be equated by the expression

$$\Delta K = K_{max,th}(1-R) \tag{3.4}$$

Both the cast Mo-4.2Si-1.1B and coarser-grained (*cf.* Section 3.4.2.1) powder-processed Mo-6.1Si-1.2B alloy exhibited a fatigue threshold (a ΔK value where crack-growth was assumed to be vanishingly small) $K_{max,th}$ = ~5 MPa√m, *i.e.* lower than the room temperature fracture toughness for these materials. By contrast, the slightly finer-grained Mo-12.1Nb-4.2Si-1.1B alloy displayed a slightly lower threshold, K_{th} = ~4 MPa√m. The fine-grained powder processed alloy, which did not have any elongated grains, failed catastrophically at ΔK = 4 MPa√m and no fatigue crack growth data could be obtained. The Paris law exponent for all three materials was approximately $m = 60$, comparable to many brittle materials.[169] The relatively high threshold values (K_{th} = ~ 70% of K_o for the cast alloys) and large Paris exponents highlight the flaw size and stress sensitivity of these intermetallic-matrixed materials. While some uncracked ligament bridges formed, over time they degraded and eventually cracked. However, the minimal bridge formation exhibited by these alloys mean little *extrinsic* toughening existed to be degraded and these materials were relatively insusceptible to fatigue. On each loading cycle the crack extended some amount then stopped. Any bridges that formed continued to carry load, but eventually failed by fatigue. As a result, the crack-microstructure interactions under cyclic loading mimicked those seen under monotonic loading, with the coarser microstructures providing better fatigue resistance.

Alloys containing a continuous α-Mo matrix exhibit similar fatigue behavior to that displayed by intermetallic-matrixed alloys. Kruzic, *et al.*[117] studied the fatigue crack growth response of their five alloys (F34, M34, C17, C46, C49, *cf.* Section 3.4.2.1) under

the same conditions used by Choe, *et al.*[85] At room temperature, owing to the relatively brittle response of the α-Mo phase, very large (>78) Paris law exponents were reported. Fatigue thresholds, $K_{max,th}$, as large as 10.6 MPa√m were reported for the coarse-grained material containing 49 vol.% α-Mo. The fatigue threshold was found to scale with microstructural size scale and volume fraction of α-Mo, while the Paris law exponent, m, decreased with increasing α-Mo content or grain size. In all cases, the fatigue threshold was approximately the same as the initiation toughness in monotonic loading, leading the authors to conclude that the mechanisms for crack growth did not change under cyclic or monotonic loading, similar to the behavior observed by Choe, *et al.*[85] Utilization of a α-Mo matrix improved the fatigue threshold, as compared to the intermetallic-matrixed materials studied by Choe, *et al.*[85] Kruzic, *et al.*[117] reported a room temperature fatigue threshold for their F34 alloy of $K_{max,th}$ = 6.8 MPa√m, an increase of 36% compared to the fatigue threshold reported by Choe, *et al.*[85] That the fatigue threshold increased with higher α-Mo volume fractions and contiguity is not surprising since the mechanisms of crack growth under cyclic loading are identical to the mechanisms for crack growth under monotonic loading. The fatigue thresholds for the F34 and M34 alloys (6.8 MPa√m and 7.2 MPa√m, respectively) were nearly the same, implying minimal influence on the fatigue threshold exerted by microstructural size scale, at least over the size regime studied in these alloys. However, the Paris slopes for the two alloys were quite different (125 for F34, 87 for M34). Since room temperature fatigue in these materials proceeds by degradation of *extrinsic* toughening mechanisms, the increased number and potency of uncracked ligament bridges (*i.e.* increased extrinsic toughness) exhibited by the coarser-grained M34 alloy leads to an increased susceptibility to fatigue, as expressed by the lowered Paris law slope for this alloy.

Alur and Kumar[99] studied both the stress-life (*S-N*) and fatigue crack-growth (da/dN versus ΔK) response of their Mo-2Si-1B isothermally forged alloy. Tension-tension *S-N* tests were performed in accordance with ASTM E466[170] at 5 Hz and a load ratio R = 0.1, with the loading direction aligned with the forging direction. Fatigue crack-growth experiments were performed using pre-cracked compact tension specimen at load ratios R = 0.1 and R = 0.2 (though no difference in behavior was noticeable for the two load ratios) and a testing frequency of 5 Hz. The forging direction was aligned with the plane of the sample as the geometry of the forged ingot precluded alignment of the notch with the forging direction. Tests were performed at constant ΔK and were interrupted every 25,000 cycles in order to optically measure any crack growth.

Though the material tested by Alur and Kumar[99] contained more α-Mo (62 vol.% than the maximum of 49 vol.% tested by Kruzic, *et al.*[117]) the fatigue response of this alloy was characteristic of a brittle material. A failure stress of 565 MPa was observed

for a 30,000 cycle life, which fell to 500 MPa for a 1,000,000 cycle life. The observed crack morphologies and fracture surfaces closely resembled the behavior of monotonically loaded samples. The authors reported a relatively low fatigue threshold (ΔK_{th} = 5 MPa√m) considering the high α-Mo content of their alloy. The low fatigue threshold exhibited by this alloy was the result of solid solution strengthening of Mo by Si and work hardening caused by isothermal forging during processing. Hardening of Mo limited its ductility and thus its ability to form uncracked ligament bridges; the degradation of these bridges is the mechanism by which fatigue occurs in Mo-Si-B alloys. It is important to note, however, that the room temperature Paris law exponent reported by Alur and Kumar (m = 17) is the lowest yet reported. While not in the regime characteristic of ductile materials (m = 2-4[163]), the relatively low value of the Paris law exponent for these materials highlights the influence of a large volume fraction of continuous α-Mo on fatigue susceptibility of Mo-Si-B alloys.

3.4.3.2 Elevated Temperature

At elevated temperatures, the fatigue resistance of Mo-Si-B alloys is improved. Improved ductility of α-Mo above ~1000°C results in larger fatigue thresholds. Above the ductile-brittle transition temperature, uncracked α-Mo bridges are much easier to form and act as more potent extrinsic toughening agents. The increased ductility of these bridges enhances their fatigue lifetimes as the material exhibits Paris law behavior more akin to ductile metals than the characteristic brittle behavior exhibited at room temperature. As a result, a larger portion of the fatigue life is spent growing a fatigue crack (as opposed to initiating a flaw that then grows) until it reaches a critical size large enough to initiate unstable fracture. Choe, *et al.*[85] saw the fatigue threshold of their Mo-4.2Si-1.1B alloy increase from 5 MPa√m at 25°C to ~ 8MPa√m at 1300°C while the Paris law exponent fell from m = ~60 to m = 44. While significant microcracking of the Mo_5SiB_2 phase provided some measure of crack-tip shielding, the ductility of the α-Mo phase was limited by its discontinuity and constraint by the surrounding intermetallic matrix; few α-Mo bridges formed as a result. More impressive fatigue resistance gains have been realized in alloys containing a continuous α-Mo, since a continuous α-Mo phase forces crack interactions and increases the effectiveness of crack trapping and uncracked ligament bridging. Kruzic *et al.*[117] reported a transition to more ductile fatigue behavior at 1300°C for their C49 alloy. While the authors were unable to accurately measure fatigue thresholds at this temperature, they found that the Paris law exponent for this alloy had dropped from m = 78 to m = 4, a characteristic value for fatigue of ductile materials.

The most comprehensive work on the high temperature fatigue behavior of Mo-Si-B was performed by Alur and Kumar[99] and Alur, *et al.*,[100] though they only studied the behavior of a two-phase Mo-2Si-1B alloy. Alur and Kumar[99] reported improved *S-N*

behavior for their alloy in a vacuum at 1200°C. The authors observed an endurance limit, which they defined as survival of the sample after 10^7 cycles at a given stress, of ~550 MPa, an improvement over the endurance limit (~500 MPa) observed at room temperature. Their material was more susceptible to fatigue at 1200°C, since plastic deformation was much more prevalent at this temperature. The authors observed some plastic stretching of α-Mo grains before failure, indicating more ductile behavior.

Alur and Kumar[99] also explored the fatigue crack growth behavior of their alloy in air (up to 600°C) and vacuum (up to 1400°C). To date, this study represents the only exploration of the combined effects of environment and temperature on the fatigue behavior of a Mo-Si-B alloy. In air, little difference was observed in the fatigue threshold (~ 5 MPa√m), but a slight increase in the Paris law exponent (m= 17 at room temperature, m = 23 at 600°C) was observed. Tests performed at 600°C *in vacuo* revealed a Paris law exponent m= 17, implying the difference in Paris law exponents in air and vacuum was caused by the environment. In this temperature regime α-Mo in this alloy oxidizes to form solid MoO_3,[99] a brittle oxide. Thus it is reasonable to believe an increase in the content of brittle phases at the expensive of more ductile α-Mo would lead to more brittle-like fatigue and thus a larger Paris law exponent. It is important to note that the effect of the testing environment on the fatigue behavior of Mo-2Si-1B was significantly smaller than that of a commercial Mo alloy. The improved oxidation resistance of an α-Mo-Mo_5SiB_2 alloy, as compared to the nominally pure Mo matrix of TZM (*e.g.* Mo-0.5Ti-0.08Zr-0.02C), was thought to minimize the effects of oxidation on the fatigue crack growth behavior of Mo-2Si-1B. However, the authors argue that the formation of a borosilicate layer leads to slip irreversibility, thus speeding crack growth and the temperature dependence of the formation of a borosilicate layer leads to the observed temperature dependence of the fatigue behavior in air up to 600°C. One aspect, acknowledged by Alur and Kumar,[99] which has never been studied is the effect of oxygen segregation and subsequent embrittlement on the fatigue behavior of their alloy.

Above 1200°C *in vacuo*, the fatigue threshold remained approximately the same as the room temperature value, but the Paris law exponent continued to decrease, falling as low as m = 3.5 at 1400°C. The authors observed fatigue striations on some grains, highlighting the improved ductility of their alloy at 1400°C. The authors did observe some creep effects, like creep cavitation, and dynamic recrystallization ahead of the growing fatigue crack. The formation of a recrystallized region provides a preferred microstructural path and speeds crack growth. However, recrystallization only occurred at 1400°C and a ΔK value (~ 9 MPa√m) much higher than the fatigue threshold.

The combined effects of creep (via the formation of creep cavities) and fatigue (via the degradation of ductile α-Mo bridges) are thought to speed crack growth and

increase the fatigue susceptibility of Mo-Si-B alloys. Alur, *et al*.[100] compared the fatigue crack growth rates of a Mo-2Si-1B alloy exposed to 4 Hz sinusoidal waveforms as well as trapezoidal waveforms including a tensile hold for various dwell times (5-15 seconds) at 1200°C and 1400°C. At 1200°C crack growth rates increased with a dwell time of at least 10 s. At 1400°C the deterioration of the fatigue resistance of this alloy was even greater. A marked increase in the fatigue crack growth rate was observed for all of the tested nonzero dwell times. The rapid increase in crack growth implied the formation of recrystallized grains and creep cavities ahead of the crack tip. The deterioration in the fatigue response increased with increasing ΔK, highlighting the influence of stress on the formation and eventual linking of creep cavities, which enhance crack growth.

3.5 Final Remarks

Alloys within the Mo-Si-B system can provide the high strength, oxidation resistance, creep resistance and damage tolerance required for ultra-high temperature structural applications. However, further optimization of these alloys is still required to tailor their microstructures for the mutually-exclusive requirements of these properties. Specifically, for optimum oxidation resistance, three-phase alloys with very small, discontinuous grains are required, whereas for creep resistance, small, discontinuous islands of α-Mo within a large-grained intermetallic matrix are superior. The most damage-tolerant microstructure, conversely, consists of large, continuous α-Mo grains as the matrix phase.

Alloying additions, like Zr, have the potential to increase the ductility of α-Mo. By increasing the plastic response capability of the α-Mo phase, it is possible to achieve high toughness utilizing far less α-Mo. As a result, the oxidation resistance of these materials can be improved. Unfortunately, Zr causes drastic deterioration of the oxidation resistance above ~1100°C.[132] Surface treatments, such as pre-oxidation in very low oxygen partial pressures as suggested by Burk, *et al.*[130] are required for Zr to become a viable alloying option.

Surface modification or thermal barrier coating of these alloys will likely be necessary to achieve the best combination of oxidation resistance and damage tolerance. The outer layer would provide oxidation resistance, while a coarse-grained interior could provide damage tolerance. Al[69, 152] and Si[83, 89, 153, 154] pack cementation have each proven successful at depositing an oxidation resistant coating on Mo-Si-B alloys, but the lifetime of such coatings is diffusion-limited . Diffusion barriers can extend the lifetime of a coating, but care is required to ensure good adhesion. Laser-remelting has also been shown to improve the oxidation resistance by reducing the grain size in the near-

surface region,[90] but the oxidation resistance of such a coating is limited by its initial thickness.

Recent publications have attempted to address the combined necessity of a large α-Mo for damage tolerance and fine grain size for oxidation resistance.[14, 15, 119-122, 136] That the oxidation resistance of these materials is superior has been previously established, but no study of the fracture behavior of these materials at ambient or elevated temperatures has been published. The following chapter will address the fracture behavior of these materials and discuss why they exhibited the reported behavior.

3.6 References

1. D. M. Dimiduk and J. H. Perepezko: 'Mo-Si-B alloys: Developing a revolutionary turbine-engine material', *MRS Bulletin*, 2003, **28**(9), 639-645.
2. J. H. Perepezko, R. Sakidja, and K. S. Kumar: 'Mo-Si-B alloys for ultrahigh temperature applications', in 'Advanced Structural Materials: Properties, Design Optimization, and Applications', (ed. W. Soboyejo), 437-473; 2007, Boca Raton, FL, CRC Press.
3. S. Drawin: 'The European ULTMAT project: Properties of new Mo- and Nb-silicide based materials', *Mater. Res. Soc. Symp. Proc.*, 2009, **1128**, 1128-U1107-1111.
4. M. Heilmaier, M. Krüger, H. Saage, J. Rösler, D. Mukherji, U. Glatzel, R. Völkl, R. Huttner, G. Eggler, C. Somsen, T. Depka, H.-J. Christ, B. Gorr, and S. Burk: 'Metallic materials for structural applications beyond nickel-based superalloys', *JOM*, 2009, **61**(7), 61-67.
5. J. H. Perepezko: 'The hotter the engine, the better', *Science*, 2009, **326**, 1068-1069.
6. A. K. Vasudévan and J. J. Petrovic: 'A comparative overview of molybdenum disilicide composites', *Materials Science and Engineering*, 1992, **A155**, 1-17.
7. J.-C. Zhao and J. H. Westbrook: 'Ultra-high temperature materials for jet engines', *MRS Bulletin*, 2003, **28**(9), 622-630.
8. J. H. Perepezko and R. Sakidja: 'Research Summary: Oxidation-resistant Coatings for Ultra-high-temperature Refractory Mo-based Alloys', *JOM*, 2010, **62**(10), 13-19.
9. M. Heilmaier, M. Krüger, and H. Saage: 'Recent advances in the development of mechanically alloyed Mo silicide alloys', *Materials Science Forum*, 2010, **633-634**, 549-558.
10. M. Heilmaier, H. Saage, M. Krüger, P. Jéhanno, M. Böning, and H. Kestler: 'Current Status of Mo-Si-B silicide alloys for ultra-high temperature applications', *Mater. Res. Soc. Symp. Proc.*, 2009, **1128, 1128-U07-07**.

11. P. Jéhanno, M. Böning, H. Kestler, M. Heilmaier, H. Saage, and M. Krüger: 'Molybdenum alloys for high temperature applications in air', *Powder Metallurgy*, 2008, **51**(2), 99-102.
12. M. Yamaguchi, H. Inui, and K. Ito: 'High temperature structural intermetallics', *Acta Materialia*, 2000, **48**, 307-322.
13. H. Nowotny, E. Dimakopoulou, and H. Kudielka: 'Untersuchungen in den Dreistoffsystemen: Molybdän-Silizium-Bor, Wolfram-Silizium-Bor und in dem System: VSi2-TaSi2', *Mh. Chem*, 1957, **88**, 180-192.
14. M. Krüger, S. Franz, H. Saage, M. Heilmaier, J. H. Schneibel, P. Jéhanno, M. Böning, and H. Kestler: 'Mechanically alloyed Mo-Si-B alloys with a continuous α-Mo matrix and improved mechanical properties', *Intermetallics*, 2008, **16**, 933-941.
15. M. R. Middlemas, J. K. Cochran, P. Jain, and K. S. Kumar: 'Strength and oxidation resistance of Mo-Si-B alloys produced by reaction synthesis', *TMS 2010 139th Annual Meeting & Exhibition - Supplemental Proceedings, Vol 1: Materials Processing and Properties*, 2010, 859-866.
16. C. A. Nunes, R. Sakidja, Z. Dong, and J. H. Perepezko: 'Liquidus projection for the Mo-rich portion of the Mo-Si-B ternary system', *Intermetallics*, 2000, **8**, 327-337.
17. N. Floquet, O. Bertrand, and J. J. Heizmann: 'Structural and morphological studies of the growth of MoO_3 scales during high-temperature oxidation of molybdenum', *Oxidation of Metals*, 1992, **37**(3), 253-280.
18. P. Jain and K. S. Kumar: 'Tensile creep of Mo-Si-B alloys', *Acta Materialia*, 2010, **58**(2124-2142).
19. P. Jain and K. S. Kumar: 'Dissolved Si in Mo and its effects on the properties of Mo-Si-B alloys', *Scripta Materialia*, 2010, **62**(1), 1-4.
20. D. Sturm, M. Heilmaier, J. H. Schneibel, P. Jéhanno, B. Skrotzki, and H. Saage: 'The influence of silicon on the strength and fracture toughness of molybdenum', *Materials Science and Engineering A*, 2007, **463**, 107-114.
21. M. K. Miller, E. A. Kenik, M. S. Mousa, K. F. Russell, and A. J. Bryhan: 'Improvement in the ductility of molybdenum alloys due to grain boundary segregation', *Scripta Materialia*, 2002, **46**, 299-303.
22. M. K. Miller and A. J. Bryhan: 'Effect of Zr, B and C additions on the ductility of molybdenum', *Materials Science and Engineering*, 2002, **A327**, 80-83.
23. H. Saage, M. Krüger, D. Sturm, M. Heilmaier, J. H. Schneibel, E. George, L. Heatherly, C. Somsen, G. Eggeler, and Y. Yang: 'Ductilization of Mo-Si solid solutions manufactured by powder metallurgy', *Acta Materialia*, 2009, **57**(13), 3895-3901.
24. S. R. Agnew and T. Leonhardt: 'The low-temperature mechanical behavior of molybdenum-rhenium', *JOM*, 2003(10).

25. D. Sun: 'Thermomechanical properties of molybdenum alloys with dispersing $MgAl_2O_4$ (spinel) and MgO particles', Master's thesis, University of West Virginia, Morgantown, WV, 2003.
26. C. K. Lee: 'Microstructure evaluations and thermomechanical properties of spinel ($MgAl_2O_4$) dispersed molybdenum alloys', Master's thesis, University of West Virginia, Morgantown, WV, 2005.
27. D. M. Scruggs: 'Ductile molybdenum composition containing a spinel dispersion', Patent 3,320,036, United States, 1967.
28. J. H. Schneibel, M. P. Brady, J. J. Kruzic, and R. O. Ritchie: 'On the improvement of the ductility of molybdenum by spinel ($MgAl_2O_4$) particles', *Zeitschrift fur Metallkunde*, 2005, **96**(6), 632-637.
29. I. M. Gunter, J. H. Schneibel, and J. J. Kruzic: 'Ductility and fracture toughness of molybdenum with $MgAl_2O_4$ additions', *Materials Science and Engineering*, 2007, **A458**, 275-280.
30. M. P. Brady, I. M. Anderson, M. L. Weaver, H. M. Meyer, L. R. Walker, M. K. Miller, D. J. Larson, I. G. Wright, V. K. Sikka, A. Rar, G. M. Pharr, J. R. Keiser, and C. A. Walls: 'Nitrogen impurity gettering in oxide dispersion ductilized chromium', *Materials Science and Engineering*, 2003, **A358**, 243-254.
31. A. Kumar and B. L. Eyre: 'Grain boundary segregation and intergranular fracture in molybdenum', *Proc. R. Soc. Lond.*, 1980, **A 370**, 431-458.
32. P. Jain, A. P. Alur, and K. S. Kumar: 'High temperature compressive flow behavior of a Mo-Si-B solid solution alloy', *Scripta Materialia*, 2006, **54**, 13-17.
33. N. A. Christensen: 'Preparation and Characterization of Mo3Si and Mo5Si3', *Acta Chemica Scandinavica*, 1983, **A37**, 519-522.
34. I. Rosales and J. H. Schneibel: 'Stoichiometry and mechanical properties of Mo_3Si', *Intermetallics*, 2000, **8**, 885-889.
35. I. Rosales: 'Synthesis and characterization of Mo3Si single crystal', *Journal of Crystal Growth*, 2008, **310**(16), 3833-3836.
36. J. G. Swadener, I. Rosales, and J. H. Schneibel.: 'Elastic and plastic properties of Mo_3Si measured by nanoindentation', *Mater. Res. Soc. Symp. Proc.*, 2001, **646**, N4.2.1-N4.2.6.
37. I. Rosales, J. H. Schneibel, L. Heatherly, J. A. Horton, L. Martinez, and B. Campillo: 'High temperature deformation of A15 Mo3Si single crystals', *Scripta Materialia*, 2003, **48**(2), 185-190.
38. I. Rosales and H. Martinez: 'High temperature solid solution strengthening by Nb additions on Mo_3Si matrix', *Materials Science and Engineering*, 2004, **A379**, 245-250.
39. S. Ochiai: 'Influence of the addition of Cr and Al elements to the Mo_3Si intermetallic alloy on the phase construction and the oxidation behavior', *Materials Science Forums*, 2003, **426-432**, 1771-1776.

40. I. Rosales, H. Martinez, D. Bahena, J. A. Ruiz, R. Guardian, and J. Colin: 'Oxidation performance of Mo3Si with Al additions', *Corrosion Science*, 2009, **51**(3), 534-538.
41. C. L. Fu and J. H. Schneibel: 'Reducing the thermal expansion anisotropy in Mo_5Si_3 by Nb and V additions: theory and experiment', *Acta Materialia*, 2003, **51**, 5083-5092.
42. J. H. Schneibel, C. J. Rawn, T. R. Watkins, and E. A. Payzant: 'Thermal expansion anisotropy of ternary molybdenum silicides based on Mo_5Si_3', *Physical Review B*, 2002, **65**, 134112.
43. H. L. Zhao, M. J. Kramer, and M. Akinc: 'Thermal expansion behavior of intermetallic compounds in the Mo-Si-B system', *Intermetallics*, 2004, **12**, 493-498.
44. J. B. Berkowitz-Mattuck and R. R. Dils: 'High-Temperature Oxidation', *Journal of The Electrochemical Society*, 1965, **112**(6), 583-589.
45. M. K. Meyer, A. J. Thom, and M. Akinc: 'Oxide scale formation and isothermal oxidation behavior of Mo-Si-B intermetallics at 600-1000°C', *Intermetallics*, 1999, **7**, 153-162.
46. M. K. Meyer and M. Akinc: 'Isothermal oxidation behavior of Mo-Si-B intermetallics at 1450°C', *Journal of the American Ceramics Society*, 1996, **79**(10), 2763-2766.
47. M. K. Meyer and M. Akinc: 'Oxidation behavior of boron-modified Mo_5Si_3 at 800°–1300°C', *Journal of the American Ceramic Society*, 1996, **79**(4), 938-944.
48. M. Meyer, M. Kramer, and M. Akinc: 'Boron-doped molybdenum silicides', *Advanced Materials*, 1996, **8**(1), 85-88.
49. K. Natesan and S. C. Deevi: 'Oxidation behavior of molybdenum silicides and their composites', *Intermetallics*, 2000, **8**, 1147-1158.
50. E. F. Riebling: 'Structure of borosilicate and borogermanate melts at 1300°C; a viscosity and density study', *Journal of the American Ceramic Society*, 1964, **47**(10), 478-483.
51. J. Schlichting: 'Oxygen transport through glass layers formed by a gel process', *Journal of Non-Crystalline Solids*, 1984, **63**(1-2), 173-181.
52. E. Ström: 'Mechanical properties of Mo_5Si_3 intermetallics as a function of composition', *Materials Characterization*, 2005, **55**, 402-411.
53. M. Akinc, M. K. Meyer, M. J. Kramer, A. J. Thom, J. J. Huebsch, and B. Cook: 'Boron-doped molybdenum silicides for structural applications', *Materials Science and Engineering*, 1999, **A261**, 16-23.
54. M. K. Meyer, M. J. Kramer, and M. Akinca (sic): 'Compressive creep behavior of Mo_5Si_3 with the addition of boron', *Intermetallics*, 1996, **4**, 273-281.
55. K. Yoshimi, M. H. Yoo, A. A. Wereszczak, S. M. Borowicz, E. P. George, E. Miura, and S. Hanada: 'Deformation behavior of Mo_5Si_3 single crystal at high temperatures', *Materials Science and Engineering*, 2002, **A329-331**, 228-234.

56. C. J. Rawn, J. H. Schneibel, C. M. Hoffman, and C. R. Hubbard: 'The crystal structure and thermal expansion of Mo_5SiB_2', *Intermetallics*, 2001, **9**, 209-216.
57. R. Sakidja, J. H. Perepezko, S. Kim, and N. Sekido: 'Phase stability and structural defects in high-temperature Mo-Si-B alloys', *Acta Materialia*, 2008, **56**(18), 5223-5244.
58. K. Ito, K. Ihara, K. Tanaka, M. Fujikura, and M. Yamaguchi: 'Physical and mechanical properties of single crystals of the T2 phase in the Mo-Si-B system', *Intermetallics*, 2001, **9**, 591-602.
59. R. D. Field, D. J. Thoma, J. C. Cooley, F. Chu, C. L. Fu, M. H. Yoo, W. L. Hults, and C. M. Cady: 'Dislocations in Mo_5SiB_2 T2 phase', *Intermetallics*, 2001, **9**, 863-868.
60. R. Sakidja, H. Sieber, and J. H. Perepezko: 'The formation of Mo precipitates in a supersaturated Mo_5SiB_2 intermetallic phase', *Philosophical Magazine Letters*, 1999, **79**(6), 351-357.
61. R. Sakidja and J. H. Perepezko: 'Phase stability and alloying behavior in the Mo-Si-B system', *Metallurgical and Materials Transactions A*, 2005, **36A**, 507-514.
62. Y. Yang, H. Bei, S. Chen, E. P. George, J. Tiley, and Y. A. Chang: 'Effects of Ti, Zr and Hf on the phase stability of Mo_{ss} + Mo_3Si + Mo_5SiB_2 alloys at 1600°C', *Acta Materialia*, 2010, **58**, 541-548.
63. R. Sakidja, J. Myers, S. Kim, and J. H. Perepezko: 'The effect of refractory metal substitution on the stability of $Mo_{(ss)}$ + T2 two-phase field in the Mo-Si-B system', *International Journal of Refractory Metals & Hard Materials*, 2000, **18**, 193-204.
64. T. Hayashi, K. Ito, K. Ihara, M. Fujikura, and M. Yamaguchi: 'Creep of single crystalline and polycrystalline T2 phase in the Mo-Si-B system', *Intermetallics*, 2004, **12**, 699-704.
65. K. Ihara, K. Ito, K. Tanaka, and M. Yamaguchi: 'Mechanical properties of Mo_5SiB_2 single crystals', *Materials Science and Engineering*, 2002, **A329-331**, 222-227.
66. K. Yoshimi, S. Nakatani, T. Suda, S. Hanada, and H. Habazaki: 'Oxidation behavior of Mo_5SiB_2-based alloy at elevated temperatures', *Intermetallics*, 2002, **10**(407-414).
67. T. A. Parthasarathy, M. G. Mendiratta, and D. M. Dimiduk: 'Oxidation mechanisms in Mo-reinforced Mo_5SiB_2 (T2)-Mo_3Si alloys', *Acta Materialia*, 2002, **50**, 1857-1868.
68. M. G. Mendiratta, T. A. Parthasarathy, and D. M. Dimiduk: 'Oxidation behavior of αMo-Mo_3Si-Mo_5SiB_2 (T2) three phase system', *Intermetallics*, 2002, **10**, 225-232.
69. F. Rioult, N. Sekido, R. Sakidja, and J. H. Perepezko: 'Aluminum pack cementation on Mo-Si-B alloys: Kinetics and lifetime prediction', *Journal of the Electrochemical Society*, 2007, **154**(11), C692-C701.

70. F. A. Rioult, S. D. Imhoff, R. Sakidja, and J. H. Perepezko: 'Transient oxidation of Mo-Si-B alloys: Effect of the microstructure size scale', *Acta Materialia*, 2009, **57**, 4600-4613.
71. V. Supatarawanich, D. R. Johnson, and C. T. Liu: 'Effects of microstructure on the oxidation behavior of multiphase Mo-Si-B alloys', *Materials Science and Engineering*, 2003, **A344**, 328-339.
72. V. Supatarawanich, D. R. Johnson, and C. T. Liu: 'Oxidation behavior of multiphase Mo-Si-B alloys', *Intermetallics*, 2004, **12**, 721-725.
73. J. Das, R. Mitra, and S. K. Roy: 'Oxidation behavior of Mo-Si-B-(Al, Ce) ultrafine-eutectic dendrite composites in the temperature range of 500-700 degrees C', *Intermetallics*, 2011, **19**(1), 1-8.
74. J. Das, R. Mitra, and S. K. Roy: 'Effect of Ce addition on the oxidation behavior of Mo-Si-B-Al ultrafine composites at 1100 degrees C', *Scripta Materialia*, 2011, **64**(6), 486-489.
75. J. S. Park, R. Sakidja, and J. H. Perepezko: 'Coating designs for oxidation control of Mo-Si-B alloys', *Scripta Materialia*, 2002, **46**, 765-770.
76. V. S. Dheeradhada, D. R. Johnson, and M. A. Dayananda: 'Diffusional analysis of a multiphase oxide scale formed on Mo-Mo_3Si-Mo_5SiB_2 alloy', *Journal of Phase Equilibria and Diffusion*, 2006, **27**(6), 582-589.
77. J. H. Schneibel, J. J. Kruzic, and R. O. Ritchie: 'Mo-Si-B alloy development', Proceedings of the 17th Annual Conference on Fossil Energy Materials, Knoxville, TN, 2003, National Energy Technology Laboratory.
78. H. Choe, D. Chen, J. H. Schneibel, and R. O. Ritchie: 'Fracture and fatigue-crack growth behavior in Mo-12Si-8.5B intermetallics at ambient and elevated temperatures', in 'Fatigue and Fracture Behavior of High Temperature Materials', (ed. P. K. Liaw), 17-24; 2000, Warrendale, PA, TMS.
79. H. Choe, D. Chen, J. Schneibel, and R. O. Ritchie: 'Ambient to high temperature fracture toughness and fatigue-crack propagation behavior in a Mo-12Si-8.5B (at.%) intermetallic', *Intermetallics*, 2001, **9**, 319-329.
80. J. H. Schneibel, C. T. Liu, D. S. Easton, and C. A. Carmichael: 'Microstructure and mechanical properties of Mo-Mo_3Si-Mo_5SiB_2 silicides', *Materials Science and Engineering*, 1999, **A261**, 78-83.
81. J. H. Schneibel, C. T. Liu, L. Heatherly, and M. J. Kramer: 'Assessment of processing routes and strength of a 3-phase molybdenum boron silicide (Mo_5Si_3-Mo_5SiB_2-Mo_3Si)', *Scripta Materialia*, 1998, **38**(7), 1169-1176.
82. D. A. Helmick, G. H. Meier, and F. S. Pettit: 'The development of protective borosilicate layers on a Mo-3Si-1B (weight percent) alloy', *Metallurgical and Materials Transactions A*, 2005, **36A**(12), 3371-3383.

83. Z. Tang, A. J. Thom, M. J. Kramer, and M. Akinc: 'Characterization and oxidation behavior of silicide coating on multiphase Mo-Si-B alloy', *Intermetallics*, 2008, **16**, 1125-1133.
84. J. H. Schneibel, M. J. Kramer, Ö. Ünal, and R. N. Wright: 'Processing and mechanical properties of a molybdenum silicide with the composition Mo-12Si-8.5B (at.%)', *Intermetallics*, 2001, **9**, 25-31.
85. H. Choe, J. H. Schneibel, and R. O. Ritchie: 'On the fracture and fatigue properties of Mo-Mo_3Si-Mo_5SiB_2 refractory intermetallic alloys at ambient to elevated temperatures (25°C-1300°C)', *Metallurgical and Materials Transactions A*, 2003, **34A**(2), 225-239.
86. V. Behrani, A. J. Thom, M. J. Kramer, and M. Akinc: 'Microstructure and oxidation behavior of Nb-Mo-Si-B alloys', *Intermetallics*, 2006, **14**, 24-32.
87. V. Behrani, A. J. Thom, M. J. Kramer, and M. Akinc: 'Chlorination treatment to improve the oxidation resistance of Nb-Mo-Si-B', *Metallurgical and Materials Transactions A*, 2005, **36A**, 609-615.
88. K. Ito, M. Kumagai, T. Hayashi, and M. Yamaguchi: 'Room temperature fracture toughness and high temperature strength of T2/Mo_{ss} and $(Mo,Nb)_{ss}$/T1/T2 eutectic alloys in the Mo-Si-B system', *Scripta Materialia*, 2003, **49**, 285-290.
89. K. Ito, T. Murakami, K. Adachi, and M. Yamaguchi: 'Oxidation behavior of Mo-9Si-18B alloy pack-cemented in a Si-based pack mixture', *Intermetallics*, 2003, **11**, 763-772.
90. F. Wang, A. Shan, X. Dong, and J. Wu: 'Microstructure and oxidation resistance of laser-remelted Mo-Si-B alloy', *Scripta Materialia*, 2007, **56**, 737-740.
91. F. Wang, A. Shan, X. Dong, and J. Wu: 'Microstructure and oxidation behavior of directionally solidified Mo-Mo_5SiB_2 (T2)-Mo_3Si alloys', *Journal of Alloys & Compounds*, 2008, **462**, 436-441.
92. S. M. Koohpayeh, D. Fort, and J. S. Abell: 'The optical floating zone technique: A review of experimental procedures with special reference to oxides', *Progress in Crystal Growth and Characterization of Materials*, **54**(3-4), 121-137.
93. P. Jéhanno, M. Heilmaier, and H. Kestler: 'Characterization of an industrially processed Mo-based silicide alloy', *Intermetallics*, 2004, **12**, 1005-1009.
94. P. Jéhanno, M. Heilmaier, H. Kestler, M. Böning, A. Venskutonis, B. Belway, and M. Jackson: 'Assessment of a powder metallurgical processing route for refractory metal silicide alloys', *Metallurgical and Materials Transactions A*, 2005, **36A**(3), 515-523.
95. D. Berczik: 'Method for enhancing the oxidation resistance of a molybdenum alloy, and a method of making a molybdenum alloy', Patent 5,595,616, United States, 1997.
96. D. Berczik: 'Oxidation resistant molybdenum alloy', Patent 5,693,156, United States, 1997.

97. S. R. Woodward, R. Raban, J. F. Myers, and D. M. Berczik: 'Oxidation resistant molybdenum', Patent 6,652,674, United States, 2003.
98. A. P. Alur, N. Chollacoop, and K. S. Kumar: 'High-temperature compression behavior of Mo-Si-B alloys', *Acta Materialia*, 2004, **52**, 5571-5587.
99. A. P. Alur and K. S. Kumar: 'Monotonic and cyclic crack growth response of a Mo-Si-B alloy', *Acta Materialia*, 2006, **54**, 385-400.
100. A. P. Alur, N. Chollacoop, and K. S. Kumar: 'Creep effects on crack growth in a Mo-Si-B alloy', *Acta Materialia*, 2007, **55**, 961-974.
101. K. S. Kumar and A. P. Alur: 'Deformation behavior of a two-phase Mo-Si-B alloy', *Intermetallics*, 2007, **15**, 687-693.
102. M. J. Kramer, S. C. Okumus, M. F. Besser, Ö. Ünal, and M. Akinc: 'Microstructure of a plasma-sprayed Mo-Si-B alloy', *Journal of Spray Technology*, 2000, **9**(1), 90-94.
103. S. C. Okumus, M. J. Kramer, A. J. Thom, and M. Akinc: 'Microstructure and oxidation behavior of plasma sprayed Mo-Si-B intermetallic coatings', *Key Eng. Mater.*, 2004, **264-268**, 509-512.
104. S. C. Okumus, Ö. Ünal, M. J. Kramer, and M. Akinc: 'Mechanical properties of plasma-sprayed Mo_5Si_3-MoB-$MoSi_2$ system', in 'Innovative Processing and Synthesis of Ceramics, Glasses, and Composites II', (eds. N. P. Bansal, et al.), 347-360; 1999, Westerville, Ohio, The American Ceramic Society.
105. N. Nomura, T. Suzuki, K. Yoshimi, and S. Hanada: 'Microstructure and oxidation resistance of a plasma sprayed Mo-Si-B multiphase alloy coating', *Intermetallics*, 2003, **11**, 735-742.
106. A. C. D. Chaklader: 'Reactive Hot Pressing: a New Ceramic Process', *Nature*, 1965, **206**(4982), 392-393.
107. R. Mitra, A. K. Srivastava, N. E. Prasad, and S. Kumari: 'Microstructure and mechanical behavior of reaction hot pressed multiphase Mo-Si-B and Mo-Si-B-Al intermetallic alloys', *Intermetallics*, 2006, **14**, 1461-1471.
108. R. Mitra, K. Chattopadhyay, A. K. Srivastava, K. K. Ray, and N. E. Prasad: 'Effect of ductile and brittle phases on deformation and fracture behavior of molybdenum and niobium silicide based composites', *Key Eng. Mater.*, 2009, **395**, 179-192.
109. S. Paswan, R. Mitra, and S. K. Roy: 'Isothermal oxidation behavior of Mo-Si-B and Mo-Si-B-Al alloys in the temperature range of 400-800C', *Materials Science and Engineering*, 2006, **A424**, 251-265.
110. S. Paswan, R. Mitra, and S. K. Roy: 'Oxidation behavior of the Mo-Si-B and Mo-Si-B-Al alloys in the temperature range of 700-1300C', *Intermetallics*, 2007, **15**, 1217-1227.
111. S. Paswan, R. Mitra, and S. K. Roy: 'Nonisothermal and cyclic oxidation behavior of Mo-Si-B and Mo-Si-B-Al alloys', *Metallurgical and Materials Transactions A*, 2009, **40A**(11), 2644-2658.

112. Z. Li and L. M. Peng: 'Ultra-high temperature Mo-Si-B alloys -- Synthesis, microstructural and mechanical characterization', *Materials Letters*, 2008, **62**, 2229-2232.
113. V. Supatarawanich, D. R. Johnson, M. A. Dayananda, and C. T. Liu: 'Processing and properties of multiphase Mo-Si-B alloys', *Materials Science Forums*, 2003, **426-432**, 4301-4306.
114. T. G. Nieh, J. G. Wang, and C. T. Liu: 'Deformation of a multiphase Mo-9.4Si-13.8B alloy at elevated temperatures', *Intermetallics*, 2001, **9**, 73-79.
115. J. H. Schneibel, M. J. Kramer, and D. S. Easton: 'A Mo-Si-B intermetallic alloy with a continuous α-Mo matrix', *Scripta Materialia*, 2002, **46**, 217-221.
116. J. J. Kruzic, J. H. Schneibel, and R. O. Ritchie: 'Fracture and fatigue resistance of Mo-Si-B alloys for ultrahigh temperature structural applications', *Scripta Materialia*, 2004, **50**, 459-464.
117. J. J. Kruzic, J. H. Schneibel, and R. O. Ritchie: 'Ambient to elevated temperature fracture and fatigue properties of Mo-Si-B alloys: Role of microstructure', *Metallurgical and Materials Transactions A*, 2005, **36A**(9), 2293-2402.
118. J. J. Kruzic, J. H. Schneibel, and R. O. Ritchie: 'Role of microstructure in promoting fracture and fatigue resistance in Mo-Si-B alloys', *Materials Research Society Symposium Proceedings*, 2005, **842**, S2.9.1-S2.9.6.
119. M. R. Middlemas and J. K. Cochran: 'Dense, fine-grain Mo-Si-B alloys from nitride-based reactions', *JOM*, 2008, **28**(7), 19-24.
120. M. R. Middlemas and J. K. Cochran: 'Oxidation behavior of Mo-Si-B alloys produced by reaction synthesis', *TMS 2008 Annual Meeting Supplemental Proceedings, Vol 3: General Paper Selections*, 2008, 177-183.
121. M. R. Middlemas and J. K. Cochran: 'The microstructural engineering of Mo-Si-B alloys produced by reaction synthesis', *JOM Journal of the Minerals, Metals and Materials Society*, 2010, **62**(10), 20-24.
122. M. R. Middlemas, J. K. Cochran, and A. M. Gokhale: 'Microstructural engineering of Mo-Si-B alloys produced using nitride-based reactions', *TMS 2009 138th Annual Meeting & Exhibition - Supplemental Proceedings, Vol 1: Materials Processing and Properties*, 2009, 177-184.
123. O. Hassomeris, G. Schumacher, M. Kruger, M. Heilmaier, and J. Banhart: 'Phase continuity in high temperature Mo-Si-B alloys: A FIB-Tomography Study', *Intermetallics*, 2011, **19**(4), 470-475.
124. A. R. Abbasi and M. Shamanian: 'Synthesis of Mo_5SiB_2 based nanocomposites by mechanical alloying and subsequent heat treatment', *Materials Science and Engineering A*, 2011, **A528**, 3295-3301.
125. A. R. Abbasi and M. Shamanian: 'Characterization of *in situ* α-Mo/Mo_5SiB_2 nanocomposite produced by mechanical alloying', *J. Alloys and Compounds*, 2010, **508**, 152-157.

126. A. R. Abbasi and M. Shamanian: 'Synthesis of α-Mo-Mo5SiB2-Mo3Si nanocomposite powders by two-step mechanical alloying and subsequent heat treatment', *Journal of Alloys and Compounds*, 2011, **doi:10.1016/j.jallcom.2011.05.066**.
127. A. Yamauchi, K. Yoshimi, K. Kurokawa, and S. Hanada: 'Synthesis of Mo-Si-B in-situ composites by mechanical alloying', *Journal of Alloys & Compounds*, 2007, **434-435**, 420-423.
128. S. R. Bakhshi, M. Salehi, H. Edris, and G. H. Borhani: 'Structural evaluation of Mo-Si-B multiphase alloy during mechanical alloying and heat treatment', *Powder Metallurgy*, 2008, **51**(2), 119-124.
129. S. R. Bakhshi, M. Salehi, H. Edris, and G. H. Borhani: 'Preparation of Mo-Si-B nanocomposite powders by mechanical alloying and heat treating', *Powder Metallurgy*, 2011, **54**(2), 108-112.
130. S. Burk, B. Gorr, and H.-J. Christ: 'High temperature oxidation of Mo-Si-B alloys: Effect of low and very low oxygen partial pressures', *Acta Materialia*, 2010, **58**, 6154-6165.
131. S. Burk, B. Gorr, V. B. Trindade, U. Krupp, and H.-J. Christ: 'High temperature oxidation of mechanically alloyed Mo-Si-B alloys', *Corrosion Engineering, Science and Technology*, 2009, **44**(3), 168-175.
132. S. Burk, B. Gorr, V. B. Trindade, and H.-J. Christ: 'Effect of Zr addition on the high temperature oxidation behavior of Mo-Si-B alloys', *Oxid. Met.*, 2010, **73**, 163-181.
133. P. G. Biragoni and M. Heilmaier: 'FEM-simulation of real and artificial microstructures of Mo-Si-B alloys for elastic properties', *Advanced Engineering Materials*, 2007, **9**(10), 882-887.
134. P. Jéhanno, M. Heilmaier, H. Saage, M. Böning, H. Kestler, J. Freudenberger, and S. Drawin: 'Assessment of the high temperature deformation behavior of molybdenum silicide alloys', *Materials Science and Engineering*, 2007, **A463**, 216-223.
135. P. Jéhanno, M. Heilmaier, H. Saage, H. Heyse, M. Böning, H. Kestler, and J. H. Schneibel: 'Superplasticity of a multiphase refractory Mo-Si-B alloy', *Scripta Materialia*, 2006, **55**, 525-528.
136. M. Krüger, H. Saage, M. Heilmaier, M. Böning, and H. Kestler: 'Influence of processing on the microstructure and mechanical behavior of Mo-Si-B alloys', *Journal of Physics: Conference Series*, 2010, **240**(1), 012087.
137. P. S. Gilman and J. S. Benjamin: 'Mechanical alloying', *Annual Review of Materials Science*, 1983, **13**(1), 279-300.
138. J. E. Gardner, M. Hilton, and M. R. Carroll: 'Bubble growth in highly viscous silicate melts during continuous decompression from high pressure', *Geochimica et Cosmochimica Acta*, 2000, **64**, 1473-1483.

139. N. P. Bansal and R. H. Doremus: 'Handbook of Glass Properties'; 1986, Orlando, FL, Academic Press.
140. J. H. Schneibel, R. O. Ritchie, J. J. Kruzic, and P. F. Tortorelli: 'Optimization of Mo-Si-B intermetallic alloys', *Metallurgical and Materials Transactions A*, 2005, **36A**(3), 525-531.
141. J. H. Schneibel, P. F. Tortorelli, M. J. Kramer, A. J. Thom, J. J. Kruzic, and R. O. Ritchie: 'Optimization of Mo-Si-B intermetallics', *Mater. Res. Soc. Symp. Proc.*, 2003, **753**, BB2.2.1-BB2.2.6.
142. P. Mandal, A. J. Thom, M. J. Kramer, V. Behrani, and M. Akinc: 'Oxidation behavior of Mo-Si-B alloys in wet air', *Materials Science and Engineering*, 2004, **A371**, 335-342.
143. A. J. Thom, M. J. Kramer, P. Mandal, and M. Akinc: 'Wet air and simulated combustion gas exposures of Mo-Si-B alloys', *Scripta Materialia*, 2005, **53**, 915-919.
144. P. F. Tortorelli, J. H. Schneibel, K. L. More, and B. A. Pint: 'Oxidation-sulfidation behavior of multiphase Mo-Si-B Alloys', *Materials Science Forums*, 2004, **461-464**, 1063-1070.
145. S. Mrowec: 'The problem of sulfur in high-temperature corrosion', *Oxidation of Metals*, 1995, **44**(1-2), 177-209.
146. J. H. Schneibel, J. J. Kruzic, and R. O. Ritchie: 'Development of Ultra-High Temperature Molybdenum Borosilicides', Proceedings of the 20th Annual Conference on Fossil Energy Materials, Knoxville, TN, 2006, National Energy Technology Laboratory.
147. A. Yamauchi, K. Yoshimi, Y. Murakami, K. Kurokawa, and S. Hanada: 'Oxidation behavior of Mo-Si-B *in situ* composites', *Solid State Phenomena*, 2007, **127**, 215-220.
148. M. G. Mendiratta, J. J. Lewandowski, and D. M. Dimiduk: 'Strength and ductile-phase toughening in the 2-phase Nb/Nb_5Si_3 alloys', *Metallurgical Transactions A*, 1991, **22**(7), 1573-1583.
149. V. Behrani: 'Oxidation behavior and chlorination treatment to improve oxidation resistance of Nb-Mo-Si-B alloys', Master's thesis, Iowa State University, Ames, IA, 2004.
150. C. T. Lynch, F. W. Vahldiek, and L. B. Robinson: 'Monoclinic-Tetragonal Transition of Zirconia', *Journal of the American Ceramic Society*, 1961, **44**(3), 147-148.
151. J. E. Jackson, D. L. Olson, B. Mishra, and A. N. Lasseigne-Jackson: 'Deposition and characterization of Al-Si metallic TBC precursor on Mo-Si-B turbine materials', *International Journal of Hydrogen Energy*, 2007, **32**, 3789-3796.
152. R. Sakidja, F. Rioult, J. Werner, and J. H. Perepezko: 'Aluminum pack cementation of Mo-Si-B alloys', *Scripta Mater.*, 2006, **55**, 903-906.

153. K. Ito, T. Hayashi, M. Yokobayashi, T. Murakami, and H. Numakura: 'Oxidation protective silicide coating on Mo-Si-B alloys', *Metallurgical and Materials Transactions A*, 2005, **36A**(3), 627-636.
154. R. Sakidja, J. S. Park, J. Hamann, and J. H. Perepezko: 'Synthesis of oxidation resistant silicide coatings on Mo-Si-B alloys', *Scripta Materialia*, 2005, **53**, 723-728.
155. T. Hayashi, K. Ito, and H. Numakura: 'Reaction diffusion of $MoSi_2$ and Mo_5SIB_2', *Intermetallics*, 2005, **13**, 93-100.
156. O. D. Sherby and J. Wadsworth: 'Superplasticity--Recent advances and future directions', *Progress in Materials Science*, 1989, **33**(3), 169-221.
157. H. J. Frost and M. F. Ashby: 'Deformation Mechanism Maps'; 1982, New York, NY, Pergamon Press.
158. J. H. Schneibel: 'High temperature strength of Mo-Mo_3Si-Mo_5SiB_2 molybdenum silicides', *Intermetallics*, 2003, **11**, 625-632.
159. J. H. Schneibel and H. T. Lin: 'Creep properties of molybdenum silicide intermetallics containing boron', *Materials at High Temperature*, 2002, **19**(1), 25-28.
160. A. G. Evans: 'Perspective on the development of high-toughness ceramics', *J. Am. Ceram. Soc.*, 1990, **73**, 187-206.
161. M. E. Launey and R. O. Ritchie: 'On the fracture toughness of advanced materials', *Adv. Mater.*, 2009, **21**, 2103-2110.
162. R. O. Ritchie: 'Mechanisms of fatigue crack-propagation in metals, ceramics and composites: role of crack tip shielding', *Mater. Sci. Eng., A*, 1988, **103**, 15-28.
163. R. O. Ritchie: 'Mechanisms of fatigue-crack propagation in ductile and brittle solids', *International Journal of Fracture*, 1999, **100**, 55-83.
164. M.-Y. He and J. W. Hutchinson: 'Crack deflection at an interface between dissimilar elastic materials', *International Journal of Solids Structures*, 1989, **25**(9), 1053-1067.
165. J. W. Foulk III, R. M. Cannon, G. C. Johnson, P. A. Klein, and R.O.Ritchie: 'A micromechanical basis for partitioning the evolution of grain bridging in brittle materials', *J. Mech. Phys. Solids*, 2007, **55**, 719-743.
166. Anon: 'ASTM E561-98. Annual Book of ASTM Standards, Vol. 03.01: Metals-Mechanical Testing; Elevated and Low-temperature Tests; Metallography', 534-546; 1998, West Conshohocken, Pennsylvania, USA, ASTM.
167. C. F. Shih: 'Relationships between the J-integral and the crack opening displacement for stationary and extending cracks', *J. Mech. Phys. Solids*, 1981, **29**(4), 205-326.
168. Anon: 'ASTM E647-00. Annual Book of ASTM Standards, Vol. 03.01: Metals - Mechanical Testing; Elevated and Low-temperature Tests; Metallography'; 2000, West Conshohocken, Pennsylvania, USA:, ASTM International.

169. R. O. Ritchie and R. H. Dauskardt: 'Cyclic fatigue of ceramics: A fracture mechanics approach to subcritical crack growth and life prediction', *Journal of the Ceramic Society of Japan*, 1991, **99**, 1047–1062.
170. Anon: 'ASTM E446-76. Annual Book of ASTM Standards, Vol. 03.01: Metals - Mechanical Testing; Elevated and Low-temperature Tests; Metallography'; 1976, West Conshohocken, Pennsylvania, USA:, ASTM International.

3.7 Figures

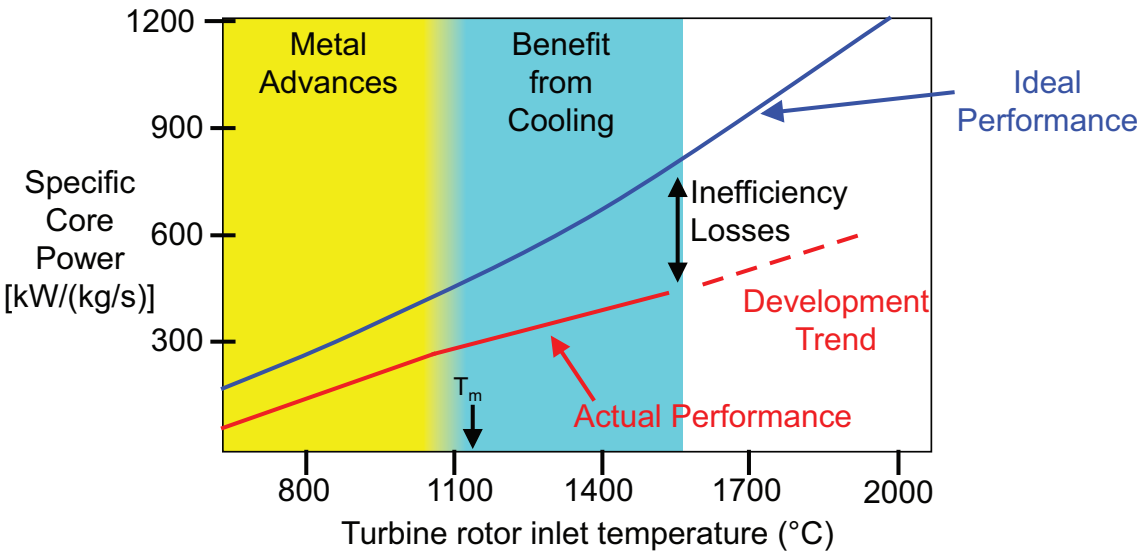

Fig. 3.1: Specific core power versus turbine inlet temperature for gas turbine engines. Current engines operate above the melting temperature of the Ni-based superalloys used within the hottest regions of the engine. As a result of complex cooling schemes and thermal barrier coatings, these turbine blade materials operate at ~1150°C, nearly 0.9 T_m. As the operating temperature has increased, an increasing large amount of the power generated is required to cool the turbine blades, drastically reducing the actual engine performance. New materials must be developed that can operate at high (>1300°C) temperatures without the need for cooling. Refractory metal silicides, such as Mo-Si-B are potential replacements for Ni-based superalloys. After Dimiduk and Perepezko.[1]

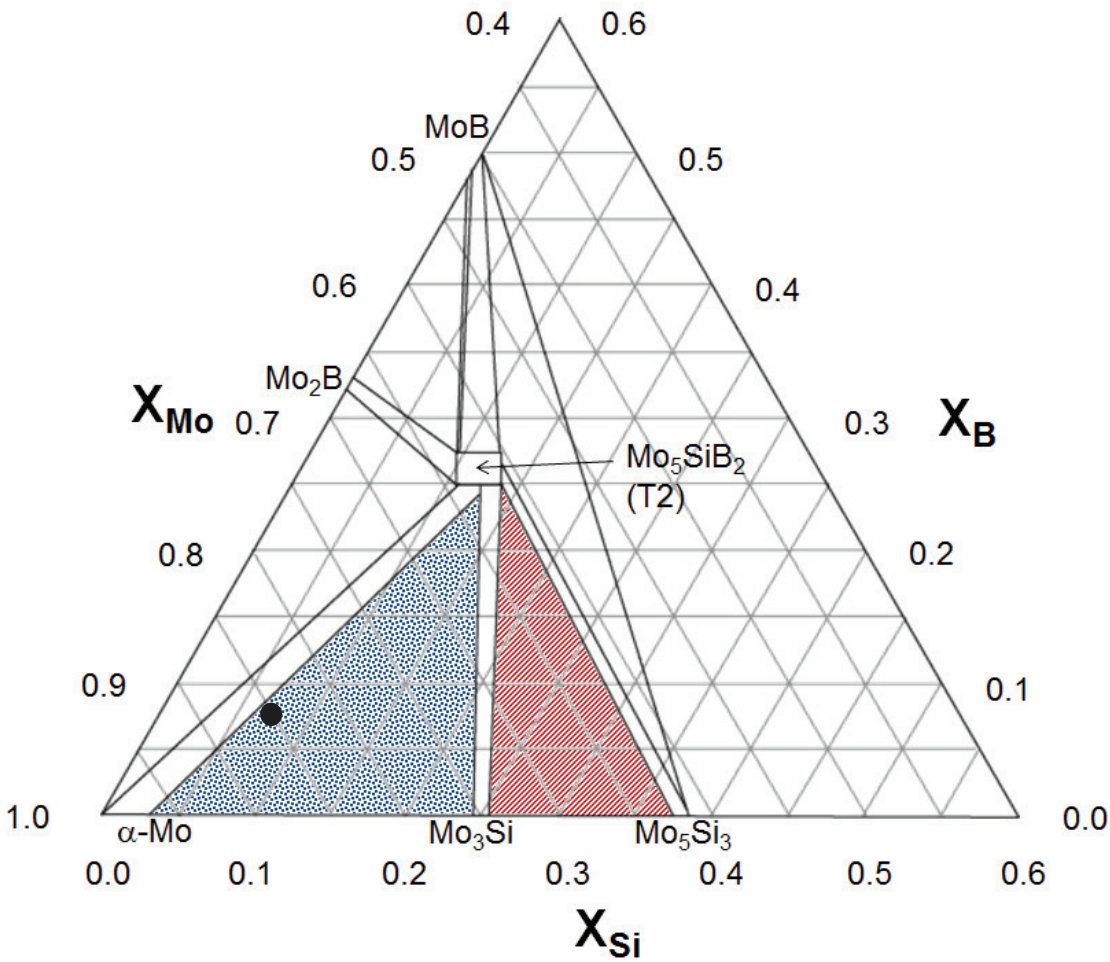

Fig. 3.2: Mo-rich portion of the 1600°C isotherm of the Mo-Si-B phase diagram. Two phase fields have received a lot of attention: Mo_3Si-Mo_5Si_3-Mo_5SiB_2 (red) and α-Mo-Mo_3Si-Mo_5SiB_2 (blue). The alloy composition studied in Chapter 4 (Mo-3Si-1B wt.%) is shown.

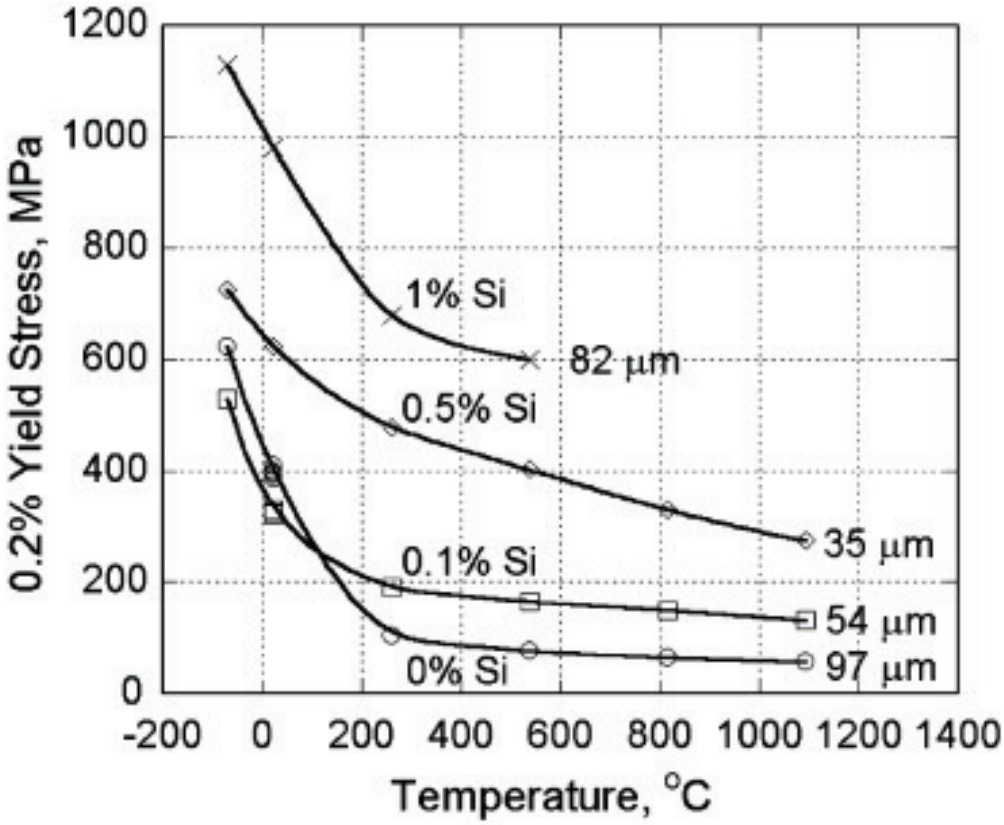

Fig. 3.3: Yield strength of Mo as a function of Si content and temperature.[20] Addition of only 0.1 wt.% Si can significantly increase the yield strength of Mo. Silicon segregates to dislocation cores[19] and acts as a potent solid-solution strengthener.

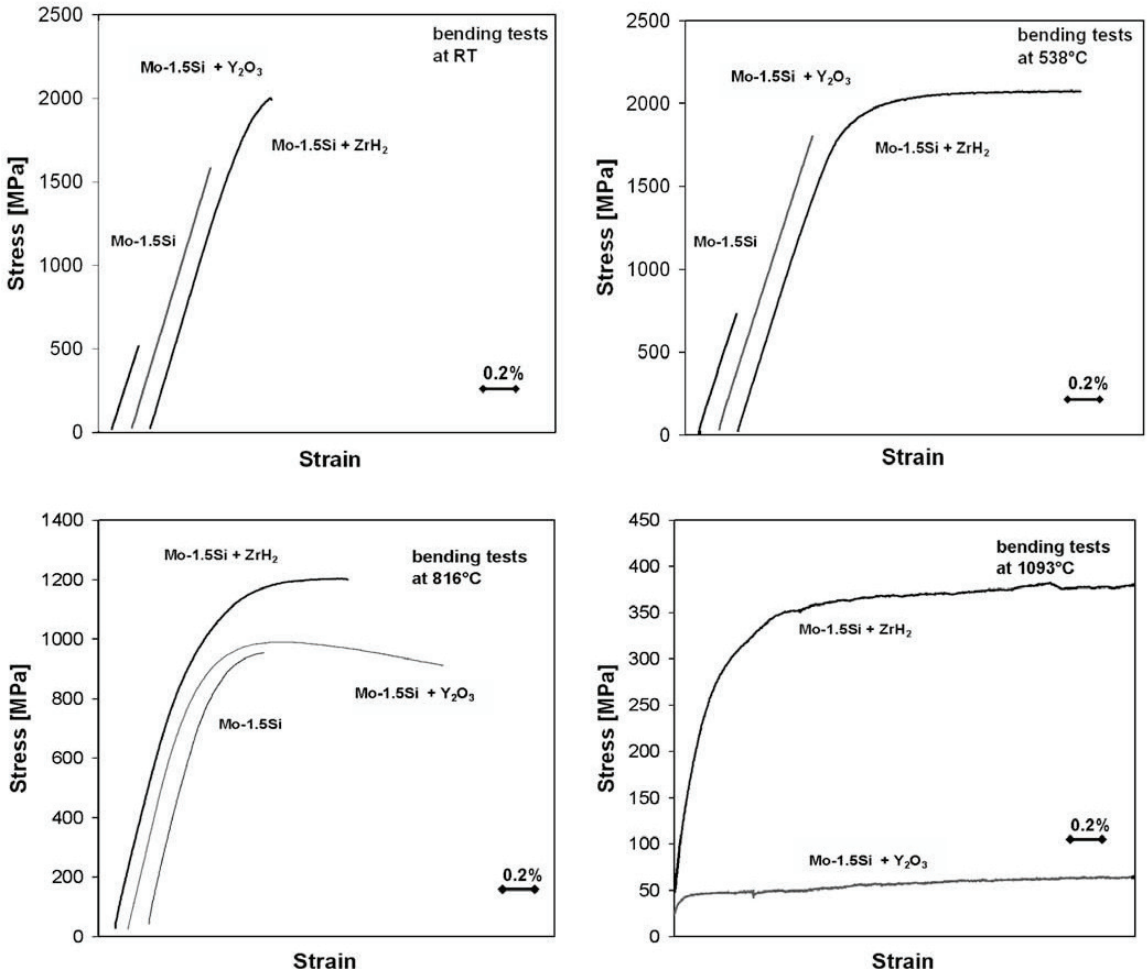

Fig. 3.4: Influence of Zr and Y_2O_3 on the stress-strain behavior of Mo-1.5 Si at various temperatures.[10] Y_2O_3, by reducing the grain size, is an effective ductilizing agent above 800°C. Small additions of Zr can increase the ductility of Mo-1.5Si and can even impart marginal room temperature ductility. Zr competes with Si for grain boundary sites, thus reducing Si segregation and increasing grain boundary adhesion.

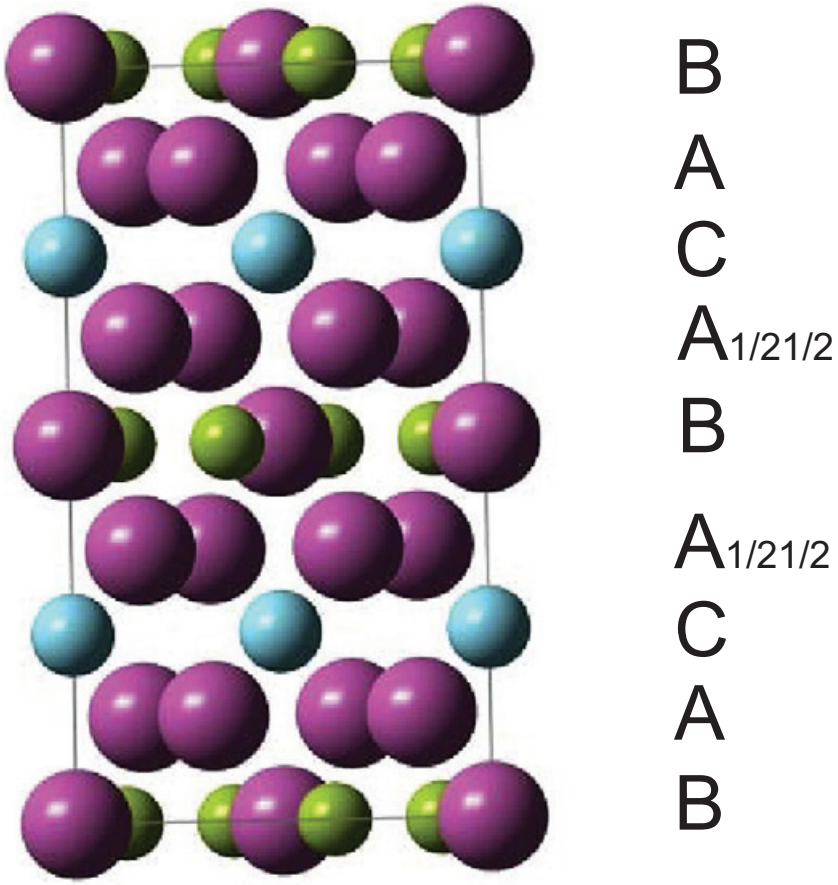

Fig. 3.5: Crystal structure of Mo_5SiB_2.[2] The unit cell contains 32 atoms (20 Mo, 4 Si and 8B) arranged in a body-centered tetragonal $D8_l$ structure. Atoms arrange in three layer types: A and $A_{1/21/2}$ containing only Mo atoms, B containing Mo and B atoms and C containing only Si atoms. Atoms on the $A_{1/21/2}$ layers are translated by one half of the basal plane diagonal in relation to A layers.

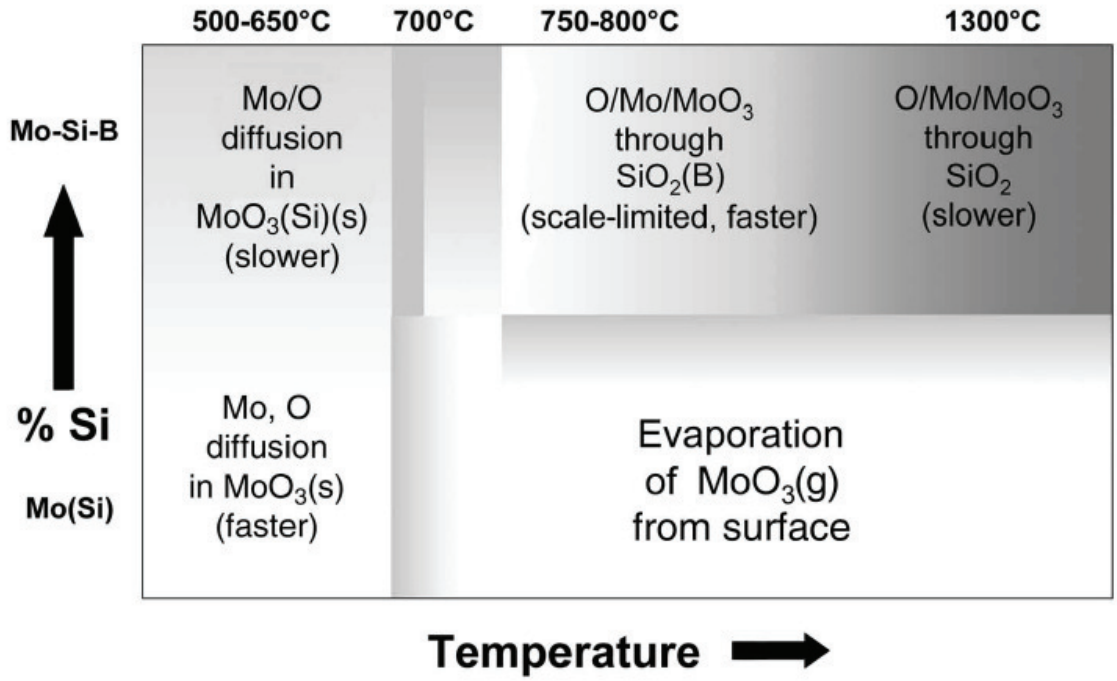

Fig. 3.6: Oxidation mechanism map for Mo-Si-B alloys.[1] At low temperature $MoO_{3(s)}$ forms, leading to parabolic weight gain. Above ~ 700°C MoO_3 sublimates. The viscosity of SiO_2 at this temperature is too high to form a protective layer. As a result linear weight loss dominates until ~ 750°C. Above this temperature regime a borosilicate layer forms and parabolic weight loss kinetics are active. However, the weight loss at 800°C is much greater than at 1300°C. Enhanced oxygen diffusion through the B-rich scale and low scale viscosity lead to rapid weight loss and incomplete fining of the scale. As the temperature increases, B_2O_3 begins to evaporate, raising the viscosity of the scale, thus closing any bubbles that might form, and slowing oxygen transport through the scale. As a result of the higher scale viscosity and lower B content within the scale, parabolic weight loss slows.

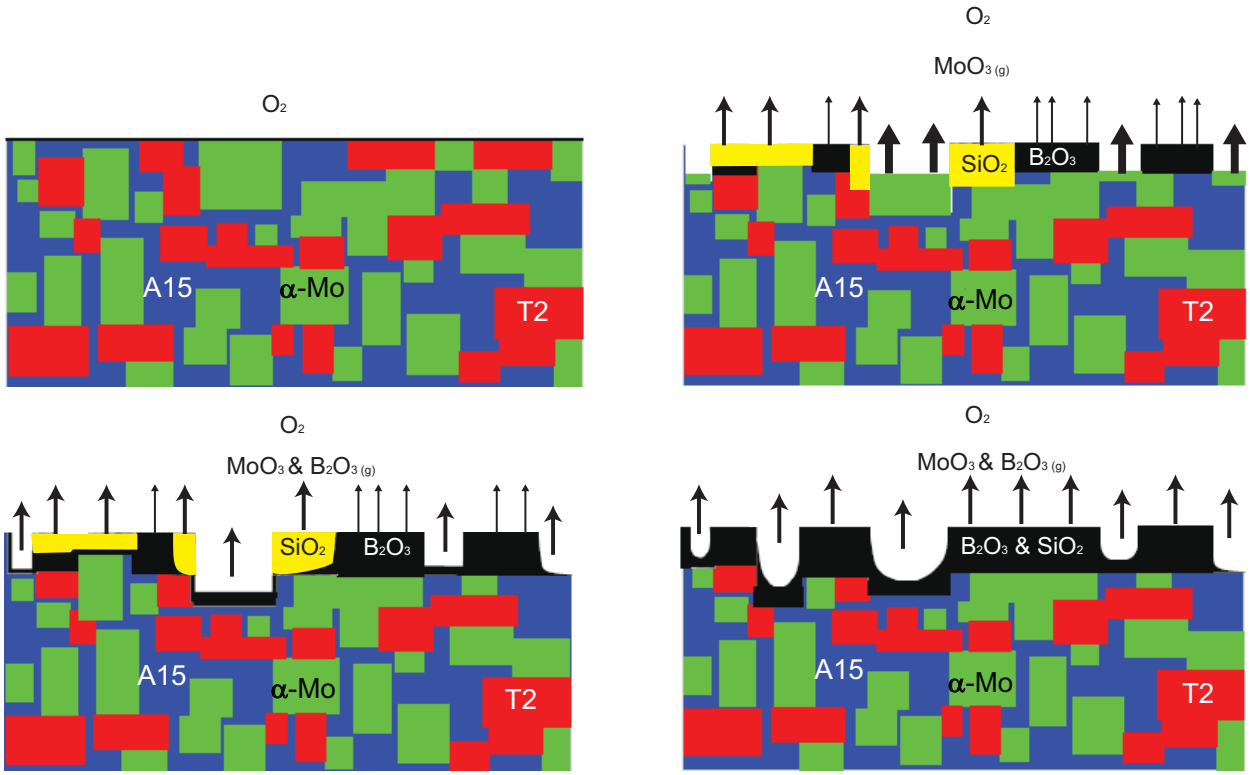

Fig. 3.7: Transient oxidation in an α-Mo-Mo_3Si-Mo_5SiB_2 alloy at 1300°C.[70] The unoxidized microstructure is shown in (a). In the initial stage, each phase oxidizes independently. α-Mo forms MoO_3 vapor, the Mo_3Si (A15) forms a nanoporous SiO_2 scale and the Mo_5SiB_2 (T2) phase forms a borosilicate scale. After some time (c) B_2O_3 flows to cover α-Mo and diffuses into SiO_2, lowering its viscosity. The lowered viscosity afforded by B_2O_3 additions speeds sintering of SiO_2 and thus passivation. A transition to steady-state oxidation occurs once the entire surface is covered in borosilicate (d).

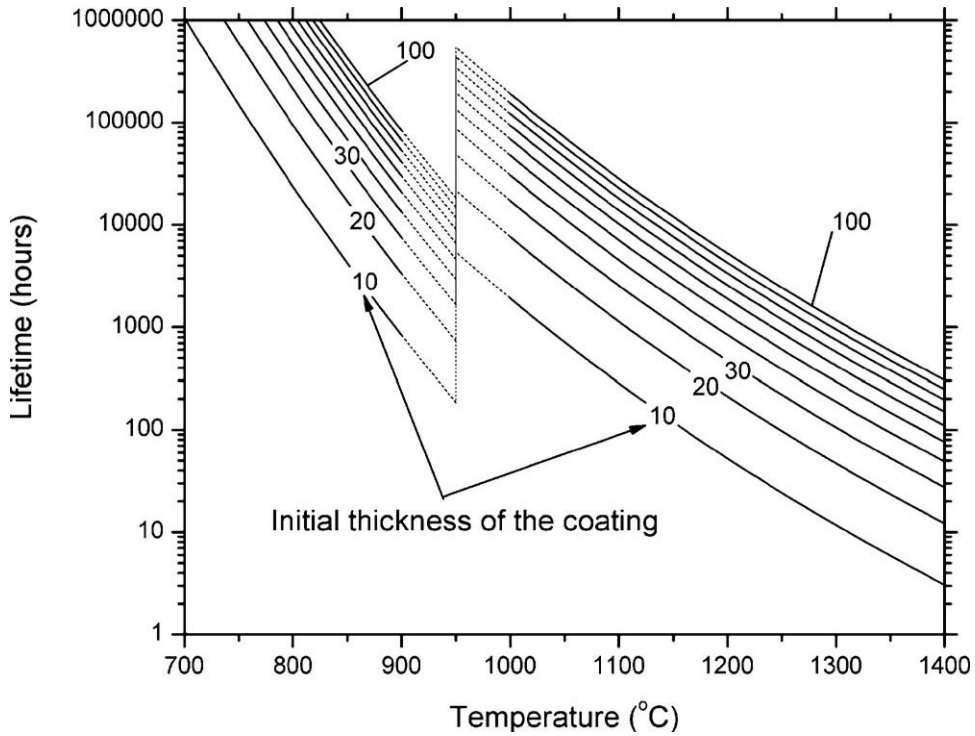

Fig. 3.8: Lifetime of an aluminum pack cemented coating on Mo-Si-B versus temperature for various initial coating thicknesses.[69] The lifetime of these coatings is dictated by depletion of Al by the formation of an $Mo_3(Si,Al)$ interlayer between the base material and the Al_2O_3 scale. Relatively thick initial coatings are required to provide long lives at elevated temperatures.

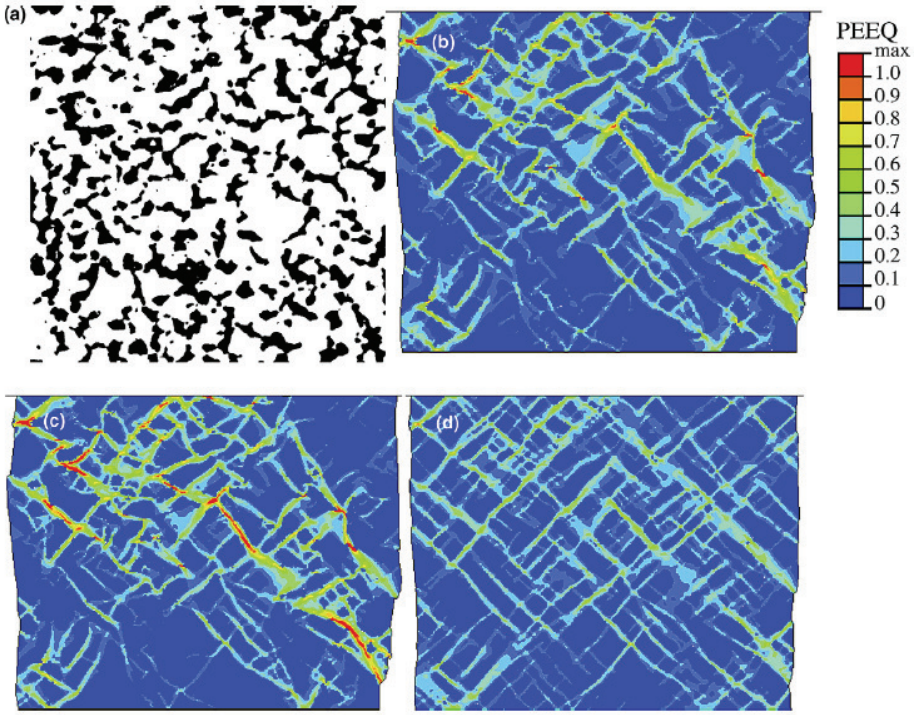

Fig. 3.9: FEM simulation of the strain localization at a global strain of 10% in a Mo-2Si-1B two phase alloy.[98] The microstructure from which a mesh was created is shown in (a). The material consisted of Mo_5SiB_2 (black) within a continuous α-Mo matrix (white). To simplify calculation, the α-Mo matrix was treated as pure Mo and modeled as an elastic-plastic material. (b) At room temperature, the strain is highly localized in the much softer and more ductile α-Mo phase. (c) At intermediate temperatures (~750°C), the localization of strain in the matrix phase increases. Alur, *et al.*[98] attributed this localization to decreased work hardening in the matrix. In this temperature regime, Mo_5SiB_2 does not plastically deform, so it was modeled as an elastic material. (d) At even higher temperatures (1550°C), where Mo_5SiB_2 can plastically deform (and was modeled as an elastic-plastic material), a much more homogeneous distribution of strain is observed. It should be noted that the properties of the α-Mo phase represent the intermediate temperature regime as the authors were unable to find mechanical property data for Mo at the highest temperature regime (1550°C).

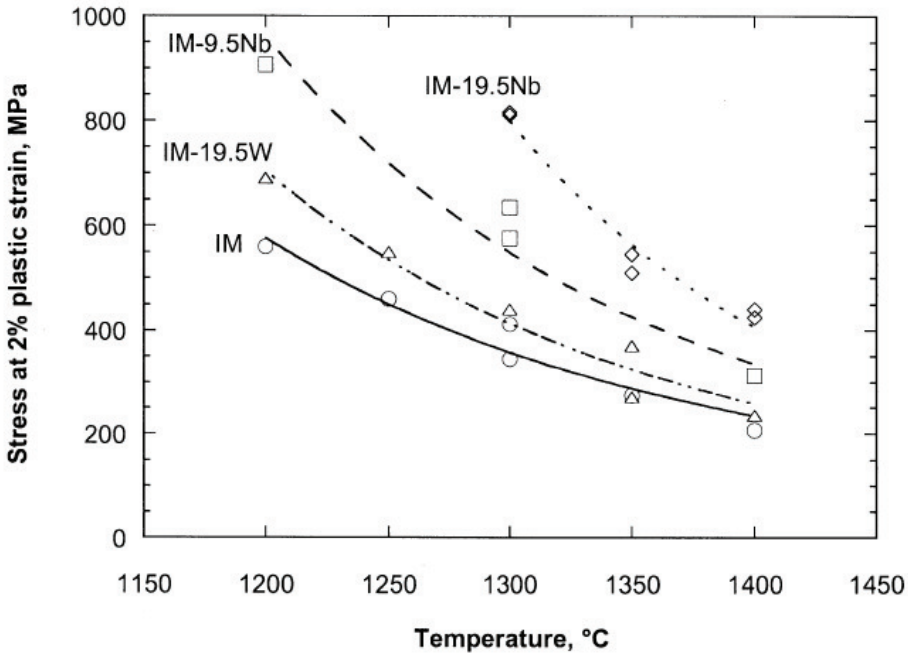

Fig. 3.10: Influence of W and Nb on the creep behavior of Mo-Si-B.[157] While the effects of W additions are slight, significant gains in creep resistance can be realized by alloying Mo-Si-B with Nb. Substitution of Mo by the larger Nb atoms is thought to slow diffusion and dislocation motion, improving the creep response of these alloys.

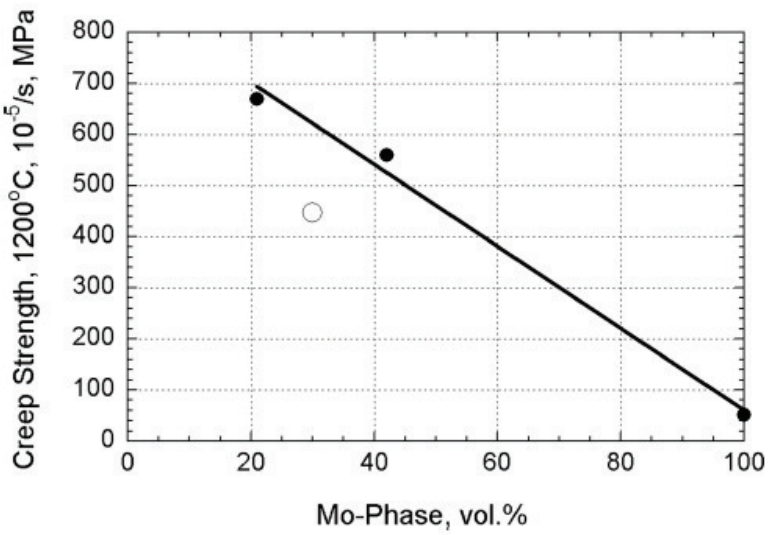

Fig. 3.11: Influence of α-Mo volume fraction on the creep strength of Mo-Si-B.[139] As the weakest and most ductile phase, increasing the volume fraction of α-Mo will severely decrease the creep strength. This effect is even greater for a continuous α-Mo matrix (open circle), as the α-Mo is not as plastically constrained by the intermetallic grains, as is the case for discontinuous α-Mo grains within an intermetallic matrix (closed circles).

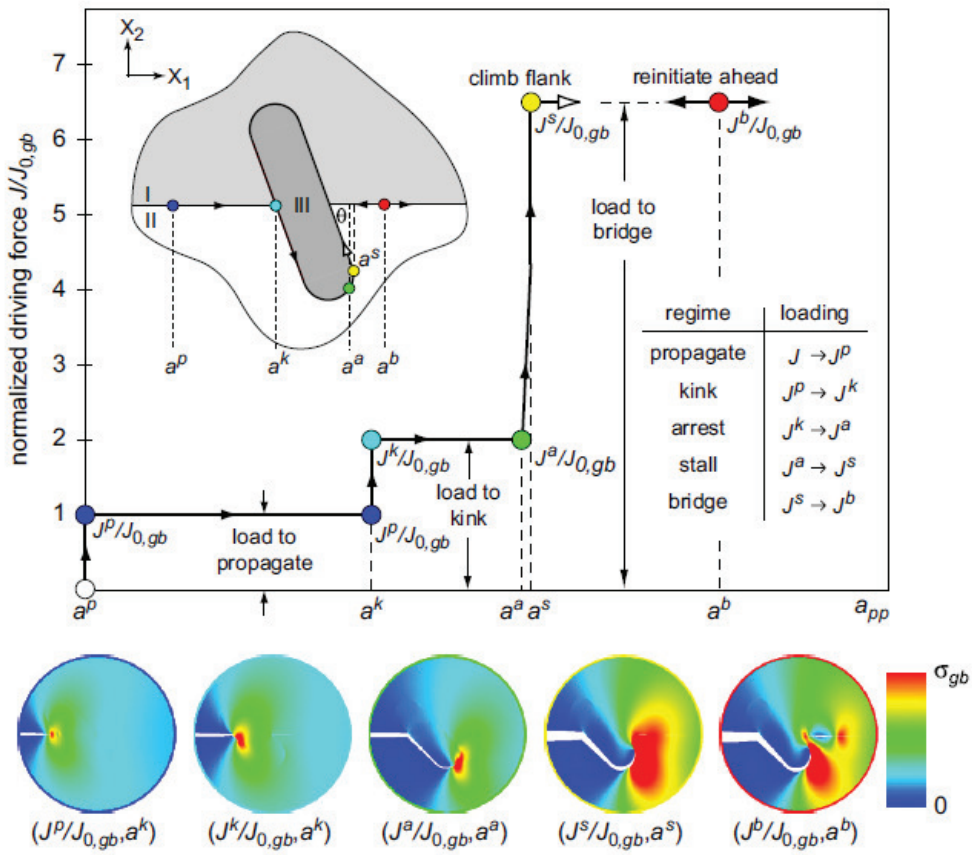

Fig. 3.12: Schematic of uncracked grain bridge formation.[164] A crack traveling within the boundary between two grains (I & II) requires a certain driving force to propagate, J^p. Upon interacting with a more ductile grain (III), the crack can kink and deflect along the preferred path of a grain boundary (depending on the ratio of grain boundary toughness to grain toughness, angle of incidence of the crack and the elastic moduli of the boundary and the grain). This preferred microstructural path is not aligned with the direction of maximum driving force, so additional driving force, J^k, is necessary to propagate the crack. Eventually, the crack will arrest at a driving force, J^a. The crack can either climb backwards up the flank of the grain, a process known as "stalling." This process is highly energetically unfavorable and a large driving force is required, J^s. The stresses that build during the stall phase can be large enough to reinitiate a crack in the boundary ahead of the ductile grain (III). The crack will proceed, leaving behind an uncracked ligament. This ligament carries some load, and shields the crack tip from the full extent of the remotely applied load. A new driving force, J^b, is required to continue crack propagation. In this way, a ductile-phase toughened material like Mo-Si-B can develop rising R-curve behavior. As the crack grows, more bridges are left in the crack wake, increasing the shielding effect.

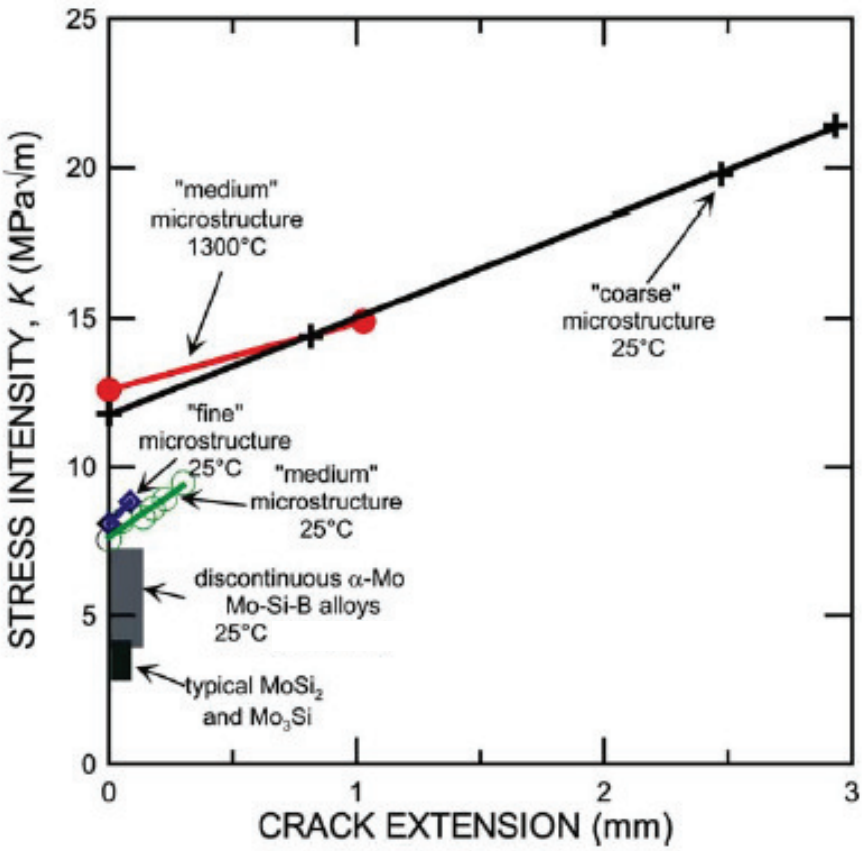

Fig. 3.13: Room Temperature R-curve for continuous α-Mo-matrixed Mo-Si-B alloys.[115] A higher volume fraction of α-Mo (~ 49 vol.% in the coarse alloy, ~34 vol.% in the fine and medium alloys) leads to more intrinsic toughening, as the α-Mo can plastically deform and raise the initiation toughness of the alloy. Extrinsic toughening, afforded by uncracked ligament bridging, is more potent for coarser grained materials. A room temperature toughness greater than 20 MPa√m has been achieved after 3 mm of crack extension. A continuous α-Mo phase forces the crack to interact with this ductile phase, where it can become blunted and trapped, raising the toughness of the material (note the higher initiation toughness for the fine and medium microstructures as compared to the reported values for discontinuous α-Mo alloys containing roughly the same volume fraction of α-Mo). In fact, a continuous α-Mo matrix allows for extrinsic toughening, while discontinuous α-Mo does not. At 1300°C the toughness of this alloy is increased, highlighting the contribution of α-Mo ductility to toughness. If the room temperature ductility of α-Mo can be increased, less α-Mo can be utilized to achieve the same degree of damage tolerance while improving the oxidation resistance.

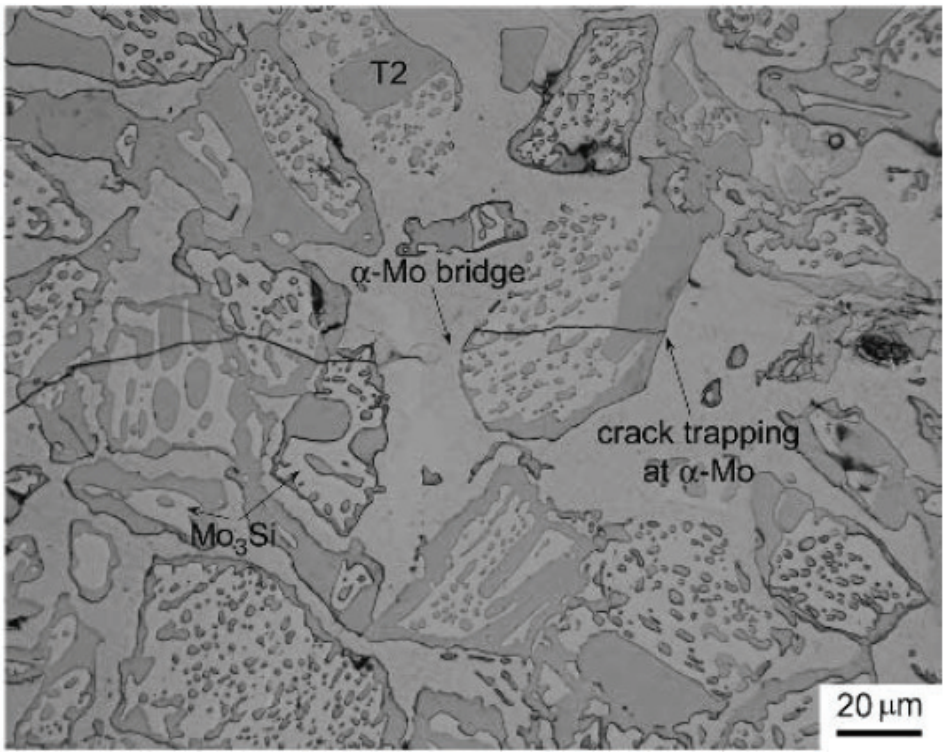

Fig. 3.14: Crack trapping and bridging in a continuous α-Mo matrixed Mo-Si-B alloy.[116] Cracks cannot avoid the continuous α-Mo phase. Uncracked ligaments can form, raising the extrinsic toughness of the material by shielding the crack tip. Cracks blunt at the plastically-deformable α-Mo phase and must reinitiate to continue propagating. This process serves to raise the intrinsic toughness of the material.

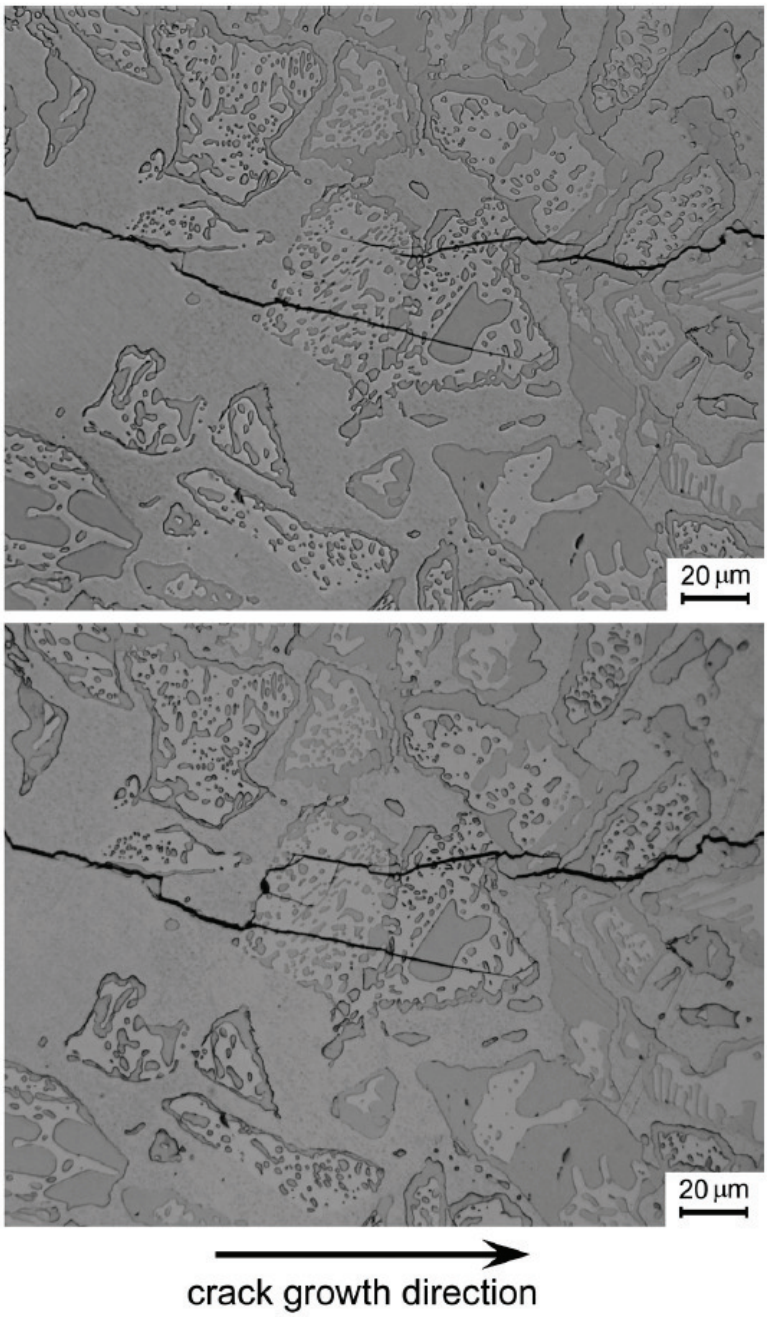

Fig. 3.15: Formation (a) and subsequent destruction (b) of an uncracked ligament bridge during cyclic loading.[117] Fatigue in these brittle materials occurs as a result of the failure of these bridges, a mechanism very different than fatigue in a ductile metal. As a result, these materials exhibit high fatigue thresholds and low susceptibility to fatigue. However, when a fatigue crack is initiated, it very quickly propagates to critical size. These materials display very large room temperature Paris law exponents (>75) unlike the Paris law exponents found in ductile materials (2-4).

Chapter 4 : On the Fracture Toughness of Fine-Grained Mo-3Si-1B (wt.%) Alloys at Ambient to Elevated (1300°C) Temperatures

4.1 Introduction

One of the most difficult problems in materials engineering today is the development of higher temperature structural materials for use in applications such as gas-turbine engines. The current material of choice, single-crystal nickel-based superalloys, has reached its technological limit; indeed, as these alloys melt at temperatures between 1200°-1400°C, they are unsuitable for structural use above ~1100°C.[1] High melting-point (>2000°C) materials, based on refractory metals such as Mo, represent a higher-temperature alternative but have been plagued by oxidation and brittleness problems. Additions of Si and B to Mo to form silicides and borosilicides have shown promise in improving the oxidation resistance; however, the silicide compounds are quite brittle and will provide little fracture resistance for most structural applications without significant active toughening mechanisms. While several alloys have been produced containing the more ductile α-Mo phase in addition the hard but brittle intermetallic phases Mo_3Si and Mo_5SiB_2 (the T2 phase), many of these show only marginal improvements in toughness relative to the monolithic intermetallic phases which have fracture toughnesses of ~ 3- 4 MPa√m.[2] This suggests that the key to achieving high fracture resistance in these materials may lie in making more effective use of the "ductile" α-Mo phase, in a manner not unlike the way that nickel-based (γ-γ') superalloys obtain high fracture toughness with a similarly high fraction of intermetallic (γ') precipitates.

Based on the early work of Nowotny, *et al.*,[3] there have been a number of studies that have explored processing routes and properties of purely intermetallic alloys[4-8] and alloys containing α-Mo solid solution as developed by Berczik;[9,10] compositions of interest are highlighted in Fig. 4.1. While the purely intermetallic alloys, which were originally studied by Akinc, *et al.*,[4-7] exhibit excellent oxidation and creep resistance, their microstructures exhibit minimal toughness as they consist solely of brittle phases (Mo_5SiB_2, Mo_3Si, Mo_5Si_3) which severely limits their utility as structural materials.

Alloys comprising the α-Mo solid solution with one or more intermetallic phases (Mo_5SiB_2 (T2), Mo_3Si), conversely, show more promise as structural materials, owing to

the measure of damage tolerance[a] afforded by the presence of the more ductile α-Mo phase. Indeed, there have now been several studies on two-phase (α-Mo, Mo_5SiB_2)[11-13] and three-phase (α-Mo, Mo_3Si, Mo_5SiB_2)[2, 14-28] versions of these alloys, with both a discontinuous[11-16] and a continuous α-Mo phase,[2,17-21] which have indicated that the three-phase systems are generally preferable as the extra silicon provided by Mo_3Si grains serves to speed passivation and improve oxidation resistance.[29,30] However, as will be discussed here, the difficulty with these alloys, as with most high-temperature materials, is that the primary mechanical property requirements, that of creep resistance, oxidation resistance and damage tolerance, tend to be mutually exclusive, leading to competing desirable microstructural morphologies: in simple terms, discontinuous, small α-Mo grains are better for oxidation resistance,[31] intermetallic grains and a discontinuous coarse α-Mo phase are better for creep resistance[18] and a continuous, large-grained α-Mo phase is better for damage tolerance.[18,19]

Faced with this difficulty, Jéhanno, *et al.*[22-26] and Middlemas, *et al.*[27,28] have developed alloys employing a finer-grained "triplex" microstructure consisting of ~50 vol.% continuous α-Mo phase intermixed with ~50 vol.% intermetallic grains in an effort to combine the oxidation resistance provided by a fine microstructure with sufficient damage tolerance provided by the more ductile α-Mo phase. In this work, we examine the fracture behavior of these fine-grained Mo-3Si-1B (wt.%) alloys, specifically to compare their ambient- and elevated-temperature (1300°C) fracture toughness properties to that of the high-toughness, coarse-grained, continuous α-Mo, alloys of the same composition, reported earlier by Kruzic, *et al.*[21]

4.2 Experimental

4.2.1 Materials

Two molybdenum borosilicide alloys with the nominal composition of Mo-3Si-1B in wt.% (Mo-9Si-8B in at.%) were examined with ~55 vol.% α-Mo and ~45 vol.% intermetallic phases. One alloy (hereafter referred to as the ULTMAT alloy) was produced and supplied by Plansee (Reutte, Tirol, Austria) following the mechanical alloying procedures put forth by Jéhanno, *et al.*[24] and modified by Krüger, *et al.*[25] The second alloy (hereafter referred to as the Middlemas alloy) was produced via the reaction synthesis method described by Middlemas and Cochran.[27]

---

[a] As in Chapter 3, damage-tolerance here represents resistance to crack propagation or more generally a tolerance to the presence of cracks. An essential requirement of almost all structural materials, it is afforded by the often mutually exclusive mechanical properties of strength combined with ductility and toughness.

4.2.1.1 ULTMAT alloy

The Plansee processing procedures involved mixing powders of elemental Mo, Si, and B (99.95, 99.6 and 98% pure, respectively) in the nominal ratio of Mo-3Si-1B by weight. Approximately 0.7 vol.% (~0.1 wt.%) of nanocrystalline Y_2O_3 powder was added before mechanical alloying to pin grain boundaries and limit further grain growth during subsequent processing. Mechanical alloying of the powders was performed under argon gas to limit the introduction of oxygen. After mechanical alloying, the powders were consolidated via cold isostatic pressing at 200 MPa, then sintered in hydrogen at 1500°C. Further consolidation was obtained by hot isostatic pressing at 1500°C with 200 MPa pressure, resulting in 500 mm long, 50-mm diameter round bars. Further details on the processing of this alloy are described by Krüger, *et al.*[25] The contiguity of the α-Mo phase has recently been confirmed by tomography.[32] The resulting microstructure is shown in Fig. 4.2a.

4.2.1.2 Middlemas alloy

Powders of elemental Mo (99.95% pure), Si_3N_4 (99% pure) and BN (99.55 pure) were dispersed in acetone with 3 wt.% Elvacite 2008 added as a binder. The slurries were milled with Al_2O_3 media on a commercial paint shaker, in order to de-agglomerate the powders, and then spray dried. Rectangular bars (15 x 15 x 60 mm) or square plates (22 x 22 x 5 mm) were cold-isostatically pressed at 345 MPa and sintered at 1600°C in an Ar/10% H_2 atmosphere. Samples were then hot-isostatically pressed at 1500°C with 207 MPa pressure to complete densification. The microstructure for this alloy is shown in Figure 4.2b.

4.2.1.3 Kruzic alloy

As noted above, data for these two fine-grained Mo-3Si-1B alloys were compared with a much coarser-grained alloy[20] of similar composition. This latter alloy, hereafter referred to as the Kruzic alloy, was manufactured at Oak Ridge National Laboratory by hot-isostatic pressing of surface-modified, 90 to 180 μm sized, powders ground from as-cast ingots of Mo-20Si-10B (at.%). The microstructure of this alloy, shown in Fig. 4.2c, contained a continuous α-Mo phase and was optimized for toughness with a coarse grain size of ~100 μm, *i.e.*, roughly an order of magnitude larger than that of either the ULTMAT or the Middlemas alloys.[20]

4.2.2 Methods

As a result of the highly brittle nature of these materials at ambient temperatures, fracture toughness properties were assessed using a variety of different specimens. Specifically, micro-notched four-point bend SEN(B) beams (38 mm long, with 6 x 3 mm

cross-section), 3-mm thick compact-tension C(T) (19 x 20 mm) and 3-mm thick disk-shaped compact-tension DC(T) (25.4 mm in diameter) specimens were electro-discharge machined from the slugs of material, with the original geometry of the slug dictating the sample geometry. The samples were ground flat on SiC papers and polished to a 1 μm finish using diamond suspensions. As described below, fracture toughness values were measured in terms of the critical value of the stress-intensity factor at the onset of crack instability using linear-elastic fracture mechanics, in accordance with ASTM Standard E-1820.[33] At 1300°C, however, small-scale yielding conditions were no longer applicable for these sample geometries; accordingly, nonlinear elastic fracture mechanics using the *J*-integral approach was used to calculate the plane-stress fracture toughness at these temperatures.[b] With this approach it is possible to overcome the size constraints of meeting small-scale yielding conditions while still properly accounting for the extension of the crack.[c] Specifically, the crack-tip opening displacement (CTOD) values at crack initiation were optically measured. Once crack initiation occurred, the samples were unloaded and cooled to room temperature at 15°C/min. *J* values were then estimated by utilizing Shih's expression to relate the CTOD, δ_t, to the *J*-integral:[34]

$$J = d_n \sigma_{flow} \delta_t, \tag{4.1}$$

where σ_{flow} is the flow stress (the average of the yield and ultimate stresses), and d_n is a dimensionless parameter varying from 0.3 to 1 dependent upon the strain-hardening exponent, *n*, the yield strain, and whether a state of plane stress or plane strain prevails. Assuming plane stress conditions (the samples were too narrow to satisfy the requirements for plane strain conditions at 1300°C) and reported yield strengths for these alloys at 1300°C,[20,24,28] with a strain-hardening coefficient of n ~0.12,[35] crack initiation δ_t values were optically measured (using the 45° intercept method) to give estimates of the crack initiation toughness, J_{iC}, which are listed in Table 4.III in the Results section. From these J_{iC} values, it is possible to estimate the equivalent stress

---

[b] *J* is the nonlinear strain-energy release rate, *i.e.*, the rate of change in potential energy for a unit increase in crack area in a nonlinear elastic solid. It is the nonlinear elastic equivalent of the strain energy release rate *G*. It characterizes the stress and displacement fields at a crack tip in such a solid, and as such can be used to define the onset of fracture there.

[c] As documented in ASTM Standard E-1820 [33], for linear-elastic K_{IC} measurements, the crack-tip plastic-zone size must be typically an order of magnitude smaller than (i) the in-plane dimensions of crack length *a* and remaining uncracked ligament *b* (small-scale yielding condition), and (ii) the out-of-plane thickness dimension *B* (a condition of plane strain); *i.e.*, $a, b, B \geq 2.5\,(K_{IC}/\sigma_y)^2$, where σ_y is the yield (or flow) strength. For nonlinear elastic *J* measurements, similar validity criteria exist although the size requirements are much less restrictive; specifically $b, B \geq 10\,(J_C/\sigma_y)$.

intensity fracture toughness values, K_{JC}, by utilizing the equivalence of K and J under linear-elastic mode I conditions:

$$K = (JE')^{1/2}, \tag{4.2}$$

where $E' = E$, the elastic (Young's) modulus) in plane stress and $E/(1 - \nu^2)$ in plane strain (ν is Poisson's modulus). Such K_{JC} values represent the plane stress fracture toughnesses that would have been obtained if a sample large enough to maintain small-scale yielding could have been used. The elastic modulus at 1300°C for these materials was estimated as 260 GPa, based on the experimental and finite element simulations performed by Biragoni and Heilmaier.[36] It should be noted that Kruzic, *et al.*[21] did not test an alloy with ~50 vol.% α-Mo at 1300°C, but the results for their 46 vol.% α-Mo material should be reasonably comparable to the present alloys.[d]

At room temperature, fracture toughness testing was performed on an MTS 810 servo-hydraulic load frame (MTS Systems, Eden Prairie, MN) with a displacement rate of 0.01 mm/min, in general accordance with ASTM Standard E-1820.[33] Any stable crack growth was monitored *in-situ* using back-face strain gauges. Samples were loaded monotonically, with periodic unloads (~10% of peak load) used to measure any changes in compliance, and thus calculate change in crack length.[33] Difficulties in fatigue pre-cracking these brittle materials necessitated the use of radiused micro-notches, where the machined notched in the test samples were subsequently sharpened with a razor blade in a 1-μm diamond suspension. Sharp micro-notches with a root radius of less than 20 μm were reliably achieved with this method.[e]

For high-temperature tests in argon, an MTS 810 servo-hydraulic load frame equipped with a Centorr Testorr vacuum/inert atmosphere furnace (Centorr Vacuum Industries, Nashua, NH) was used. Fracture toughness tests at elevated temperatures were performed in flowing argon gas to prevent oxidation of the samples. Crack length was monitored in real time using the DC potential-drop technique as calibrated for

---

[d] The toughness value reported by Kruzic, *et al.*[21] for their alloy was an overestimate as it was based on a "rule of mixtures" calculation using the room temperature elastic modulus values. Moreover, the authors assumed a d_n of unity in Eq. 4.1, corresponding to plane stress loading of a perfectly plastic material, whereas a more accurate value for their material is 0.586. Accordingly, we have recalculated their toughness values here.

[e] This technique is commonly used for ceramic materials where similarly generating fatigue pre-cracks can be very difficult. The presence of a stress concentrator with a micron-sized root radius, rather than a fatigue crack with a root radius closer to atomic dimensions, has the effect of truncating the early portion of the crack-resistance curve (R-curve) and thereby slightly elevating the crack-initiation toughness.

elevated temperatures.[37] All high-temperature test samples were held at 1300°C for 20 minutes prior to testing to allow the sample temperature to equilibrate.

Scanning electron microscopy (SEM), and Auger electron spectroscopy (AES) were used to analyze the microstructure, fracture path and fracture surface of each alloy. Samples used for microstructural and crack path analysis were etched in modified Murakami's reagent (15 g potassium ferricyanide, 2 g NaOH in 100 mL water) to reveal the grain structure. Oxygen and silicon levels in the grain boundaries and the interior of α-Mo grains were studied using notched beam-like specimens. The beams were notched with a diamond saw followed by sharpening with a razor blade. The specimens were fractured at room temperature in an ultra-high vacuum (UHV) chamber of a field emission Auger microprobe (PHI 680 Auger Nanoprobe, Physical Electronics, Inc., Chanhassen, MN). The samples fractured in a highly intergranular manner, allowing for the study of impurities in the grain boundaries. α-Mo grains which fractured transgranularly were used to study the impurity levels within α-Mo grains. Fracture surface impurities were analyzed by Auger spectrometry at 10 kV / 20 nA immediately after fracturing the specimens at a vacuum between 10^{-9} and 10^{-10} torr. Impurity maps were created by overlaying the Auger data on images of the fracture surfaces taken by the same machine.

4.3 Results

4.3.1 Uniaxial tension/compression properties

Very little basic tensile data have been reported for any of these alloys, especially at room temperature. All three alloys display negligible ductility and fracture in a brittle manner; no room temperature yield or tensile strength data are available. Based on Rockwell C hardness indentation, the respective UTS values of the ULTMAT and Middlemas alloys at room temperature are estimated as approximately 2100 and 2200 MPa.[f] At elevated temperature, some data has been published, but the test method used (as well as the testing temperatures) varies, so it is somewhat difficult to make a direct comparison for some properties. Large differences in the coefficients of thermal expansion between the intermetallic phases and α-Mo lead to tensile thermal stresses after HIPping and vastly different yield strengths for these alloys in tension and compression.[26] At 1300°C, *in vacuo*, the Middlemas alloy had yield and tensile strengths of 419 and 436 MPa, respectively, and an elongation to fracture of 10%.[28] At 1200°C, *in vacuo*, the Kruzic alloy had yield and tensile strengths of 336 and 354 MPa, respectively,

[f] These alloys are extremely brittle at room temperature. As the UTS values are estimated from hardness indentations, they are undoubtedly representative of the compressive (rather than tensile) strengths.

and an elongation at fracture of 1.8%.[20] The only tensile yield and ductility data published for the ULTMAT alloy at 1300°C is for an alloy formed via gas-atomization.[22] Data from Jéhanno, *et al.*[26] for compression of the mechanically alloyed material studied here and gas-atomized Mo-Si-B alloys shows a convergence of strengths as the testing temperature approaches 1300°C. As a result, comparisons can be drawn between the reported yield strength for the ULTMAT alloy and the Middlemas and Kruzic alloys, even though the microstructures for the gas-atomized alloy and the mechanically alloyed Mo-Si-B used in this study are slightly different. The alloy studied by Jéhanno, *et al.*[22] had a yield strength of 275 MPa, a tensile strength of 315 MPa and an elongation to fracture of 20%. These results are summarized in Table 4.I.

Table 4.I: Summary of the high temperature tensile properties of several Mo-3Si-1B (wt.%) alloys

Alloy	Test Condition	σ_y (MPa)	σ_{UTS} (MPa)	Ductility (ε_f)
ULTMAT[22]	1300°C, *in vacuo*	275	315	20.2%
Middlemas[28]	1300°C, *in vacuo*	419	436	10.0%
Kruzic[20]	1200°C, *in vacuo*	336	354	1.8%

4.3.2 Fracture Toughness Behavior

4.3.2.1 Room Temperature

During fracture toughness testing at room temperature, no subcritical (stable) crack growth was observed prior to outright fracture in either of the fine-grained (ULTMAT and Middlemas) alloys; instead, samples fractured immediately at the onset of crack initiation. Crack-initiation toughnesses, K_{IC}, for each alloy are shown in Table 4.II where they are compared with initiation toughness data for the Kruzic alloy of comparable composition, but containing an order of magnitude larger α-Mo grains. Also shown are data for a fine-grained Mo-Si-B alloy (termed the Choe alloy) with α-Mo alloy phase that is both lower in content (38 vol.%) and discontinuous (as isolated islands) within an intermetallic (Mo_5SiB_2 + Mo_3Si) matrix.[2,15] It can be seen that the ULTMAT and Middlemas alloys have nearly identical crack-initiation toughnesses as the Choe alloy. All the finer-grained alloys, however, have a much lower (~36%) room temperature fracture toughness than that the coarse-grained Kruzic alloy.

Table 4.II: Summary of the measured crack-initiation fracture toughness data for several Mo-Si-B alloys at ambient temperatures

Alloy	Grain Size (μm)	Grain Morphology	Crack-Initiation Toughness K_{IC} (MPa√m)	Standard Deviation (MPa√m)
ULTMAT[25]	~ 20	Continuous α-Mo	7.80	0.92
Middlemas[28]	5-20	Continuous α-Mo	7.13	0.53
Kruzic[21]	> 100	Continuous α-Mo	11.75	N/A
Choe[2]	10	Discontinuous α-Mo	7.15	N/A

Scanning electron microscopy of the fracture surfaces showed intergranular fracture to be the dominant failure mechanism. Compared to the Kruzic alloy (Fig. 4.3c), both the ULTMAT (Fig. 4.3a) and Middlemas (Fig. 4.3b) alloys exhibited a far higher proportion of intergranular failure consistent with their negligible ductility. They both failed catastrophically as soon as cracks initiated with no evidence of a rising R-curve, though the lack of subcritical crack growth in these alloys was likely an effect of the relative bluntness of the radiused notch as compared to a fatigue pre-crack.[g] In contrast, the coarse-grained Kruzic alloy displayed ~3 mm or so of subcritical cracking prior to failure, consistent with limited rising R-curve toughening behavior. Note that even the Choe alloy exhibited a small degree of rising R-curve toughness behavior with ~ 1 mm of stable crack extension.[2,15] The room temperature toughness of these materials, as well as any rising R-curve behavior with stable crack extension is shown in Fig. 4.4.

4.3.2.2 Elevated Temperature

At 1300°C, both the ULTMAT and Middlemas alloys displayed significant ductility, such that significant subcritical cracking was observed (Figs. 4.5a&b). However, the alloys displayed so much plasticity that tests had to be stopped prematurely as the bend samples came into contact with the loading fixture; therefore only limited subcritical crack growth was observed (Note the vastly different scale markers in Figs. 4.5a-c). Measured and calculated values of these high-temperature

[g] The crack resistance- or R-curve provides an assessment of the fracture toughness in the presence of subcritical crack growth. It involves measurements of the crack-driving force, *e.g.*, the linear-elastic stress intensity K, the strain energy release rate G or nonlinear elastic J-integral, as a function of crack extension (Δa). The value of the driving force at $\Delta a \rightarrow 0$ provides a measure of the crack-initiation toughness whereas the slope and/or the maximum value of the R-curve can be used to characterize the crack-growth toughness.

crack-initiation fracture toughnesses for the ULTMAT, Middlemas and Kruzic alloys at 1300°C are listed in Table 4.III.

Table 4.III: Summary of the crack-initiation fracture toughness data for several Mo-Si-B alloys at elevated temperatures (1300°C)

Alloy	σ_{flow} (MPa)	E (GPa)	d_n	CTOD, δ_t (μm)	J_{iC} (J/m^2)	K_{JC} (MPa√m)
ULTMAT[25]	295	260	0.577	11	1872	22
Middlemas[28]	428	260	0.600	10	2565	26
Kruzic[21]	345	260	0.586	10	2022	23

The combined fracture toughness data from Tables 4.II and 4.III are plotted in Fig. 4.6 for the current fine-grained ULTMAT and Middlemas alloys, as compared to the coarse-grained (continuous α-Mo) Kruzic alloy and the fine-grained (lower volume fraction, discontinuous α-Mo) Choe alloy. Initiation toughness are represented by closed symbols, while any observed rise in toughness as the result of stable crack growth is plotted using open symbols. Although the room temperature toughness behavior of the ULTMAT and Middlemas alloys is poor and resembles that of alloys with significantly lower volume fractions of α-Mo, at elevated temperature these alloys significantly outperform the Mo-Si-B materials studied by Choe, *et al.*[2,15] and match the response exhibited by the much coarser-grained Kruzic alloy.[21] Tests on the ULTMAT alloy at intermediate temperatures showed minimal ductility and no stable crack growth, even though slight gains in the initiation toughness were realized (Fig. 4.6).

4.3.3 Auger Electron Spectroscopy: Oxygen and Silicon Impurities

Fracture surfaces of samples broken *in-situ* and the corresponding Auger electron spectra are shown in Fig. 4.7a-c. Spectra were taken from both grain boundary (A1) and α-Mo grain interior (A2) material. The concentrations of Si and O on the grain boundaries and in the grain interiors are given in Table 4.IV. It should be noted that these values do not represent the true impurity levels and while the determination of exact concentrations of impurities was precluded by standardless analysis, qualitative statements about impurity levels can still be made. Three other factors make precise chemical analysis of these alloys by AES more difficult. Firstly, oxygen adsorbs readily onto the fresh fracture surfaces from the ultra-high vacuum (>10^{-9} torr) atmosphere,[38] making precise determination of oxygen levels on the fracture surface difficult without Monte Carlo simulations of oxygen attachment to allow for the subtraction of the ever-

increasing background oxygen.[39] Secondly, the peaks for Mo and B overlap, so B levels cannot be determined via this technique without using standards. Lastly, slight overlap of the Si and Mo peaks artificially lowers the reported silicon levels in the transgranular regions. Though standardless AES analysis cannot provide exact impurity levels, it is a useful technique for mapping locations of higher and lower impurity concentrations, as shown in Fig. 4.8a-f.

Only slight differences in the oxygen levels in both the grain boundaries and grain interiors were observed for all three alloys. While adsorption of oxygen onto the surface throughout the duration of the experiment prevents exact determination of oxygen levels, each sample was exposed to the atmosphere for the same amount of time (~10 minutes), thereby implying similar amounts of adsorbed oxygen. The oxygen maps do not show much difference between the oxygen distributions in the three alloys, but individual scans of the grain interiors and grain boundaries for all three alloys do reveal differences. Since the adsorbed oxygen level is assumed to be similar for all three alloys, it is possible to use the difference in oxygen peak intensity for the grain boundaries and grain interiors to qualitatively describe oxygen segregation in these alloys. As shown in Fig. 4.6a, the oxygen peak intensities are nearly identical for the ULTMAT alloy, implying little oxygen segregation in this alloy. By contrast, as shown in Figs. 4.6b and 4.6c, the Middlemas and Kruzic alloys display marked differences in the oxygen peak intensities for the grain boundaries and grain interiors. The higher peak intensities for the grain boundaries of these alloys imply a higher degree of oxygen segregation.

Table 4.IV: Impurity Si and O Levels as measured via Auger Electron Spectroscopy

Material	Location	Si (at. %)	O (at. %)
ULTMAT	Grain Boundary	35.5	7.7
	Grain Interior	7.2	8.7
Middlemas	Grain Boundary	31.0	8.8
	Grain Interior	4.3	13.7
Kruzic	Grain Boundary	10.3	11.7
	Grain Interior	4.7	17.7

Unlike the oxygen impurities, which displayed small, but nontrivial grain boundary segregation, large variations in the silicon levels existed both between the grain boundaries and grain interiors and between alloys. For each alloy, the interior of a transgranularly-fractured α-Mo grain was analyzed, revealing a similar amount of silicon for all three alloys. In each case, the level of Si within the grain was much lower

than that of the grain boundaries. Areas of high silicon content correspond to regions of intergranular fracture. The grain boundaries of the ULTMAT and Middlemas alloys both contained similar concentrations of Si, although both of these alloys contained significantly more Si than the Kruzic alloy.

4.4 Discussion

4.4.1 Microstructural Optimization

The design and development of new materials for ultrahigh temperature applications is invariably a competition between achieving excellent oxidation resistance and creep strength at service temperatures and maintaining adequate ductility and toughness at both low and high temperatures. Unfortunately, the microstructural requirements to achieve acceptable behavior in all three categories are generally mutually exclusive. This is a particularly difficult problem in Mo-Si-B alloys where the microstructures for optimal oxidation resistance, creep strength and damage tolerance (strength and toughness) are so contradictory. Specifically, for oxidation resistance, the three-phase alloys with very small discontinuous grains are best as the small grains limit the probability that an α-Mo grain will be exposed to oxygen; likewise, the small grains provide a short diffusion pathway allowing for faster passivation than in coarser-grained alloys.[31] In direct contrast, optimal room-temperature damage tolerance is afforded by large, continuous α-Mo grains that promote *extrinsic* toughening[h] by the generation of ductile ligament bridges that act to "shield" a crack tip from the full force of an applied stress, thereby inhibiting crack advance.[2,20,21] Corresponding high-temperature toughness is also promoted by a high volume fraction of α-Mo as the ductility of this phase generates extensive plasticity which toughens the alloy intrinsically. In further contrast, optimal creep response is provided by alloys with large intermetallic grains surrounding small islands of α-Mo, which limits the number of high-diffusivity pathways such as grain boundaries;[18] a low volume fraction of α-Mo is also desirable, as the relative ease of deformation of α-Mo at high temperatures allows individual intermetallic particles to rearrange easily. Fig. 4.9 shows schematic illustrations of the microstructural morphologies necessary to maximize material response for each property.

---

[h] Toughening in materials can be considered as a mutual competition between intrinsic and extrinsic mechanisms. *Intrinsic* toughening mechanisms dominate in ductile materials; they operate ahead of the crack tip to generate resistance to microstructural damage, with the most prominent mechanism being that of plastic deformation. *Extrinsic* toughening mechanisms, conversely, operate primarily in the wake of the crack tip to inhibit cracking by "shielding" the crack from the applied driving force.[40-43] Whereas intrinsic toughening mechanisms are effective in inhibiting both the initiation and growth of cracks, extrinsic mechanisms, such as crack bridging, are only effective in inhibiting crack growth.[41-43]

The alloys developed by Jéhanno, *et al.*[22-25] and Middlemas, *et al.*[27,28] attempt to address the needed improvement in oxidation resistance while having a negligible impact on damage tolerance. However, as shown in this paper, the "triplex" microstructures of continuous α-Mo intermixed with intermetallic grains actually significantly decrease room-temperature toughness compared to the coarser-grained microstructures such as the Kruzic alloy,[21] even though the volume content of α-Mo is the same (~55 vol.%). The critical point here is that at low temperatures, Mo-Si-B alloys are truly brittle materials as the α-Mo phase can only provide for very limited ductility. *Brittle materials can only be toughened extrinsically*, and as such the coarser microstructures are able to generate toughness (more precisely crack-growth resistance) through such shielding processes as crack deflection and ductile-ligament bridging. The much smaller grains in the ULTMAT and Middlemas alloys do not act as such impediments to crack propagation. Though a large volume fraction of α-Mo would imply a very high probability of the more ductile grains interacting with a moving crack and trapping it, the extremely small grain size provides a pathway by which a crack can avoid the more ductile grains without a large increase in energy. Correspondingly, the room-temperature fracture profile for the ULTMAT alloy shows a very flat crack trajectory (Fig. 4.10a); though not shown, the Middlemas alloy exhibited similar behavior. Although cracks can deflect at α-Mo grain boundaries, the small deviation in crack path requires very little additional energy, and thus is limited in its efficacy as an extrinsic toughening mechanism. Since the crack can easily avoid the small ductile grains, this also restricts what little plasticity may be present. An important observation in the present work is that embrittlement of the grain boundaries further serves to weaken the material, and can reduce the crack-initiation toughness. The coarser-grained Kruzic alloy, conversely, readily forms uncracked regions across the α-Mo grains at room temperature (Fig. 4.10b). The resulting uncracked ligaments then act to bridge the crack, thereby carrying load that would otherwise be used to further crack extension, and as such extrinsically toughen the material. As the crack extends subcritically, more uncracked ligaments are left in the crack wake, leading to the rising R-curve behavior.[21] Previous work has shown that coarse equiaxed microstructures are more effective than fine equiaxed microstructures at increasing the crack growth toughness of intermetallic alloys through bridge formation.[21,44]

4.4.2 Plastic Constraint

Another factor lowering the room-temperature toughness of these alloys is the high degree of plastic constraint imposed on the ductile α-Mo grains by the hard intermetallic phases. The presence of hard particles limits the ductility of α-Mo grains, and thus lowers their effectiveness as crack traps and bridges. Chan and Davidson[45] developed a model to account for the decrease in toughness caused by plastically-

constrained ductile particles. In the case of constrained ductile particles, they proposed that the toughness of a ductile-phase toughened brittle material is given by:

$$K_C = K_C^{Brittle}\sqrt{\left(1+\sqrt{1-f}\left[\left(\frac{K_C^{Ductile}}{K_C^{Brittle}}\right)^2 \exp\left(-\frac{8q}{3}\left(\frac{f}{1-f}\right)\right)-1\right]\right)} \tag{4.3}$$

where $K_C^{Brittle}$ and $K_C^{Ductile}$ are the toughnesses of the brittle and ductile phases, f is the volume fraction of brittle phase and q is a geometric factor here taken to be unity (representative of spheroidal particles). For an unconstrained ductile phase, the corresponding toughness is given by:[45]

$$K_C = K_C^{Brittle}\sqrt{\left(1+\frac{2}{\sqrt{\pi}}\sqrt{1-f}\left[\left(\frac{K_C^{Ductile}}{K_C^{Brittle}}\right)^2 -1\right]\right)} \tag{4.4}$$

Using toughness values of ~3 MPa√m for the brittle (intermetallic) phase(s)[46,47] and ~15 MPa√m for the ductile (α-Mo) phase, these models predict that the toughness of the alloy would be reduced from ~13.8 MPa√m for an unconstrained ductile phase to ~4.8 MPa√m for a constrained ductile phase. While not particularly predictive of the absolute toughness values of the current alloys (Eqs. 4.3-4 are especially sensitive to the volume fraction at which hard particles begin to contact the ductile phase as the strengthening contribution afforded by hard particles is constant once contact is established[45]), these models do serve to illustrate the loss in extrinsic toughening, by a factor of ~3, associated with the constraint imposed by the hard intermetallic grains on the more ductile α-Mo phase. In fact, in the terminology adopted by Chan and Davidson,[45] both the ULTMAT and Middlemas alloys suffer from "brittle-phase embrittlement" where the high degree of plastic constraint imposed by the high volume fraction of intermetallic (Mo_3Si and Mo_5SiB_2) grains acts to counteract the potential ductile-phase toughening afforded by the α-Mo grains. As a result, any α-Mo grains that interact with a crack will break, or cause deflection of the crack into the grain boundaries, rather than exhibit the crack trapping-reinitiation mechanism necessary to form a ductile ligament bridge. This issue is exacerbated by small grain sizes, as the mean free path between two intermetallic grains is shorter increasing the amount of constraint on each α-Mo grain. Lin and Chan[48] showed that the maximum effective plastic strain occurs within the interface between a strengthening particle and the surrounding matrix (here the grain boundaries between the harder intermetallic phases and the α-Mo matrix). As a result, grain boundaries fail prematurely, lowering the toughness of the material.

4.4.3 Influence of Impurities

While some degree of grain boundary weakness (and thus intergranular fracture) is advantageous to the toughness of these alloys (and is in fact necessary for the formation of interlocking grain bridging ligaments), a purely intergranular fracture of severely weakened grain boundaries would severely limit any such (extrinsic) crack-growth resistance. In such a situation, the toughness of the alloy is governed by the toughness of the grain boundary, and not the toughnesses of the constituent phases. Conversely, increased interfacial strength can lead to premature failure of uncracked ligaments[48] or crack penetration and transgranular cleavage instead of deflection,[49] again limiting the ability of the material to be toughened extrinsically. As a result, akin to many ceramic materials,[50] precise control of the concentration of grain-boundary impurities, such oxygen and silicon which lower grain boundary strength, is vitally important for insuring enhanced damage tolerance in these alloys.

Another consideration limiting the effectiveness of α-Mo as a ductile phase is solid-solution strengthening of molybdenum by silicon. The α-Mo phase in these alloys can contain as much as 4 at.% Si[i] greatly increasing the strength of this phase, at the cost of reduced ductility and toughness.[51,52] The dearth of plasticity afforded by the solid solution phase magnifies the effects of plastic constraint, as the contact stresses caused by the intermetallic grains cannot be alleviated by plastic deformation. As a result, the values used for the toughness of the "ductile" phase in Eqs. 4.3 and 4.4 are likely overestimated. Sturm, *et al.*[52] showed a drop in room temperature toughness from 24 MPa√m for pure molybdenum to ~5 MPa√m for a solid solution containing 2 at.% Si.

Scanning Auger electron spectroscopy was performed in an effort to locate any oxygen or silicon impurities in both the fine-grained alloys, as well as the coarse-grained Kruzic alloy. Oxygen is known[53] to have has a deleterious effect on the strength of grain boundaries in molybdenum alloys. Free oxygen has a greater potential to weaken the grain boundaries than oxygen tied up in silica or other glassy inclusions, so the location of any oxygen impurities is vitally important to these alloys' structural performance. Silicon is also well known[54] as a solid solution strengthener of Mo at the expense of toughness; however, it can segregate to grain boundaries, greatly reducing their cohesive strength.

Though some degree of oxygen segregation was apparent in the Middlemas and Kruzic alloys, it is difficult to comment on the severity of this segregation based on these results. The presence of Si on the grain boundaries of these materials, as shown in

[i] This implies that the α-Mo phase remains supersaturated with Si after precipitation of the intermetallic phases, which is not uncommon for mechanically alloyed materials.[51]

Figs. 4.6a-c, is problematic, especially in the case of the fine-grained ULTMAT and Middlemas alloys, which have a much larger grain boundary volume than the Kruzic material.

The disparity in Si levels is a result of the processing method used to manufacture each alloy. The powders used to make the Kruzic alloy are vacuum annealed to enrich the powder particle surfaces in Mo by driving off Si as volatile SiO.[17,21] Hot-isostatic pressing these surface modified powders created a continuous α-Mo microstructure with very low Si content in the grain boundaries, as the particle interfaces (which become grain boundaries upon sintering) were silicon-depleted.

The processing methods used to create the ULTMAT and Middlemas alloys can result in excess Si in the α-Mo phase. Specifically, supersaturation of the α-Mo phase during mechanical alloying can lead to segregation of Si to grain boundaries during precipitation of the intermetallic phases. Likewise, incomplete reaction of Mo and Si_3N_4 to form Mo_3Si and Mo_5SiB_2 can lead to excess free silicon, which then segregates to grain boundaries, lowering their cohesive strength.

4.4.4 Microalloying with Zr to improve the ductility of α-Mo

Microalloying elements such as Zr have been shown to increase the room temperature ductility of Mo-Si-B alloys[54] by gettering oxygen and competing with Si for grain-boundary atomic sites. Zirconium increases grain-boundary adhesion in Mo-Si alloys and thus increases strength, while at the same time allowing for some plastic deformation, even at room temperature.[54] The "ductilizing" effect of Zr additions is even greater at elevated temperatures. Although the exact effects of Zr on the toughness of Mo-Si-B alloys have not been studied in depth, initial results are promising. Schneibel, *et al.*[18] showed a 50% increase in initiation toughness for a Mo-12Si-8.5B (at.%) alloy with the addition of 1.5 at.% Zr. However, some of these toughness gains were lost when the Zr content was raised to 3 at.%, behavior that the authors were unable to explain.

The increased ductility afforded by Zr comes at a heavy price, however. Burk, *et al.*[55] demonstrated that Zr additions as small as 0.5 at.% accelerate the formation of a borosilicate layer, which is not protective at 1300°C. The damaging effects of Zr additions arise from two phenomena: (i) increased oxygen diffusion and gas permeation possibly caused by a viscosity change, and (ii) the formation of voids resulting from a phase change in the ZrO_2 which causes shrinkage.[55] At temperatures above 1100°C, ZrO_2 can undergo a phase transformation from a monoclinic structure to a tetragonal structure, accompanied by a decrease in volume. This shrinkage leaves pores within the SiO_2 layer which act as pipes to the base alloy underneath the SiO_2

layer. As a result of the high oxygen pressure that develops, volatile MoO_3 forms readily and leaves behind additional porosity, exacerbating the speedy oxidation of the base material. Pre-oxidation of these materials at oxygen partial pressures in the range 10^{-12}-10^{-19} bar are required to alleviate this problem.[56]

4.4.5 Fracture at Elevated Temperatures

The fracture behavior of the fine-grained alloys is quite different at elevated temperatures; above the ductile-brittle transition temperature for these materials (at ~1150°C[25,28]) the enhanced ductility of the α-Mo phase now allows for significant plastic deformation. In fact, Jéhanno, *et al.* showed that Mo-2.7Nb-8.9Si-7.7B (at.%) alloys can exhibit superplastic behavior at 1300°C at strain rates as high as 10^{-3} s^{-1}.[24,57] Alloys tested under these conditions exhibited strains to failure in excess of 400%.[24,57] As the alloys can now be considered as ductile, intrinsic toughening associated with plasticity provides the dominant contribution to the toughness. This is primarily governed by the volume fraction of the ductile α-Mo phase, rather than the grain morphology, with the result that at 1300°C, the fine-grained ULTMAT and Middlemas alloys, with their high volume fraction of α-Mo, now display comparable toughness to the coarse-grained materials (Fig. 4.5). At temperatures as low as 300°C, pure molybdenum can have an initiation toughness greater than 60 MPa$\sqrt{m}$[58] with the toughness at 1300°C expected to be much higher. The toughness of the silicon-containing α-Mo phase will not be as high as that for pure Mo (owing to the effects of solid solution strengthening), but it should be clear that the adverse effects of plastic constraint can be overcome once the ductile-brittle transition temperature is surpassed. At elevated temperatures, uncracked grain ligaments are much easier to form, even for such fine-grained materials as the ULTMAT and Middlemas alloys. The reduced strength of α-Mo at elevated temperatures lowers the barriers to plastic deformation, allowing for significant crack blunting. As a result of this blunting, crack reinitiation must occur, leaving behind an uncracked grain ligament. It is unclear at this time how the contribution to toughening by uncracked ductile ligaments will differ between the fine-grained and coarser-grained materials. The additional toughness afforded by uncracked ductile ligaments can be understood by an examination of the strain-energy release rate, *G*.[j] Sigl, *et al.*[59] described the toughening contribution of uncracked ligaments, in terms of the strain energy release rate $G = K^2/E$, by:

$$\Delta G = V_f \sigma_y t \chi, \tag{4.5}$$

[j] The strain-energy release rate, *G*, is another measure of toughness, which describes the amount of strain-energy dissipated by an advancing crack. *G* is related to the linear-elastic fracture toughness, *K*, by $G = K_I^2/E' + K_{II}^2/E' + K_{III}^2/2\mu$, where E' is E (plane stress) or $E/(1-\nu)^2$ (plane strain, ν is Poisson's ratio) and μ is the shear modulus.

where V_f is the volume fraction of bridges, σ_y is the yield strength, t is the size of the bridges and χ is a work of rupture, dependent on the ductility, plastic constraint and strain hardening of the ductile phase. At elevated temperatures, the ductility of these alloys is significantly increased, but the yield strength is much lower. As a result, the crack-growth toughness (*i.e.*, the slope of the R-curve) will not be affected as greatly as the initiation toughness, although some gains are expected.[21] While the smaller grains of the ULTMAT and Middlemas alloys would imply smaller bridges (as are observed in Figs. 4.4a & b), a larger number of grains can act as bridges. Campbell, *et al*.[44] demonstrated that a large volume of many small bridges may be nearly as effective at producing crack growth toughness in γ-TiAl as a smaller volume of fewer large bridges. Campbell, *et al*.[44] observed the largest toughness increase in materials containing high-aspect ratio lamellae, while the increase toughness caused by bridging was more limited in material containing equiaxed grains. The potential attractiveness of ultra-fine grained Mo-3Si-1B (wt.%) alloys as structural materials is due, in part, to the possibility of producing a large number of small bridges in these alloys. However, further study is needed to quantify the additional crack-growth toughness afforded by uncracked ductile ligaments in these finer-grained, equiaxed materials.

Note that for a similar loads and plastic strains in Figs. 4.5a & b, the damage around the crack tip is much more widespread for the ULTMAT alloy than the Middlemas alloy. It is likely that higher concentration of oxygen impurities, arising from oxygen entrainment during mechanical alloying leads to a degradation of the effectiveness of the extrinsic toughening mechanisms. Few SiO_x particles were observed, so it is unlikely that the entrained oxygen reacted with free silicon to form oxide particles, which have much less effect on the fracture toughness of these inherently brittle alloys. Instead, the oxygen remains free to embrittle the grain boundaries, reducing the effectiveness of any extrinsic toughening mechanisms. As a result, the ULTMAT alloy, with its much higher bulk oxygen impurity level,[25,27] will likely have a shallower R-curve, *i.e.*, the crack-growth toughness of the ULTMAT alloy will be lower than the Middlemas alloy, though further experimentation is necessary to confirm this behavior.

4.4.6 Environmental Effects

As these materials are unlikely to see service in inert atmospheres, the fracture behavior of Mo-Si-B alloys under the combined effects of temperature and oxidative atmospheres is of critical importance, although this has received scant attention in the literature. Only two studies have probed the effect of oxidation on the high temperature fracture behavior of Mo-Si-B alloys; both examined materials with discontinuous α-Mo, where the oxidation response was superior yet their toughness behavior was inferior to those in the current study.

Schneibel, *et al.*[16] showed a moderate increase in the initiation toughness of their Mo-12Si-8.5B (at.%) alloy when tested in air at 1200°C (20 MPa√m, as compared to ~10 MPa√m at room temperature), but they did not report any toughness values for samples in inert atmosphere. The alloy that they tested was identical to the material studied by Choe, *et al.*[2,15] who reported an initiation toughness of ~10 MPa√m at 1300°C in Ar. Few details are provided by Schneibel, *et al.*[16] regarding their testing procedure, except that they used chevron-notched samples, so their toughness values would be elevated, as explained in Footnote d. Even accounting for the effects of the chevron notch, Schneibel, *et al.*[16] reported an initiation toughness value for their alloy tested in air at 1200°C that is 50% larger than that reported for the same alloy by Choe, *et al.*[2,15] tested in Ar at 1300°C. The origin of this discrepancy is unknown, and difficult to explain without more information regarding the test methods used by Schneibel, *et al.*[16]

Alur and Kumar[11] have provided the only rigorous study of effect of the interplay of oxidation and elevated temperature on the fracture toughness of Mo-Si-B alloys to date, but they only tested in air up to 600°C owing to the relatively poor oxidation performance of their two-phase alloys; their exposure times to air at elevated temperature were also very short. Their work showed that in the regime 20°-600°C, the presence of an air atmosphere has little effect on the fracture toughness of Mo-Si-B alloys;[11] this follows because their toughness tests only lasted tens of minutes and this was not long enough for significant oxidation to occur. The oxidation effect is naturally much more important for longer term fatigue testing; in fact Alur and Kumar[11] showed an increase with temperature in the Paris exponent for fatigue-crack growth of their material when cycled in air, whereas this exponent decreased significantly for tests *in vacuo* over the same temperature range, behavior which is indicative of the embrittling capabilities of oxygen at elevated temperatures. Accordingly, in order to properly assess the effects of oxidation on fracture behavior, it is necessary to allow steady-state oxidation to develop before toughness testing begins. Transient oxidation (the initial mass loss caused by the evaporation of MoO_3) transitions to steady-state oxidation in approximately 2 hours at 1100°C for these alloys.[26,28] To date, a comprehensive study on the effects of oxidation on the fracture behavior of these alloys has not been performed.

4.4.7 Influence of Processing Method

Finally, it is of note that the ULTMAT and Middlemas alloys achieve nominally identical microstructures via very different processing routes. Both mechanical alloying and reaction synthesis have the advantage of industrial scalability, a property that was noticeably lacking in previously-studied processing methods such as those described by Berczik,[9,10] Jéhanno, *et al.*[22,23] or Schneibel, *et al.*[17] Each process can yield sub-micron equiaxed grains (if sub-micron powders are initially used in the case of the Middlemas

alloy), allowing for superplastic deformation and thus much easier forming. Mechanical alloying will necessarily lead to higher impurity levels, especially oxygen, as it is impossible to handle the materials under an inert atmosphere throughout the entire process. Reaction synthesis can lead to much lower impurity levels, as no foreign media, such as milling media, need to be introduced. Reaction synthesis also affords much greater microstructural flexibility. Precipitation of the intermetallic phases from a mechanically alloyed matrix leads to the creation of an equiaxed grain structure. Further microstructural changes require post-processing steps such as extrusion. By altering the morphology or chemical composition[60-62] of the starting powders, it is possible to create a greater range of microstructural morphologies with reaction synthesis, though some post-processing may still be necessary. At 1300°C, the strength of the Middlemas alloy is ~30% greater than that of the ULTMAT alloy, while its ductility is only half as much. This effect is likely the result of the smaller grain size of the ULTMAT alloy, which allows for superplastic deformation at the reported strain rate.[24,57] The paucity of reported mechanical properties for Mo-Si-B makes a precise comparison difficult.

4.5 Conclusions

An experimental study of the ambient- and elevated-temperature (1300°C) fracture behavior of two fine-grained, ~55 vol.% continuous α-Mo, Mo-3Si-1B (wt.%) alloys (the ULTMAT and Middlemas alloys) was conducted, and the results were compared to a similar alloy (the Kruzic) with a much coarser grain structure tested previously. From these experiments, the following conclusions can be made:

1. Although the fine grain size of both the ULTMAT and Middlemas alloys allows for quick passivation and minimal mass loss during oxidation, poor low-temperature fracture toughness results from a lack of *extrinsic* toughening.
2. The low toughness of the fine-grained materials is exacerbated by their weak grain boundaries and high levels of plastic constraint caused by the fine-grained intermetallic phases which further inhibit bridge formation at room temperature.
3. While Auger electron spectroscopy of oxygen levels was inconclusive, much larger silicon levels were found in the grain boundaries of the ULTMAT and Middlemas alloys than in the grain boundaries of the Kruzic alloy. The processing method used to manufacture the Kruzic alloy creates powders whose surfaces (and thus the resulting grain boundaries) have been depleted of silicon.
4. Since silicon segregation is known to lead to a preponderance of intergranular fracture in these alloys, alloying additives must be found to prevent limit this segregation.

5. Zirconium at first seems promising as a ductilizing agent, as small amounts have been shown to greatly increase the room temperature toughness of Mo-Si-B alloys, but the adverse effect of Zr on the oxidation resistance of these alloys limits its usefulness. Pre-oxidation at very low oxygen partial pressures is required to prevent catastrophic oxidation of Zr-containing alloys.
6. At elevated temperatures the increased ductility of α-Mo generates significant plasticity (and hence intrinsic toughening), resulting in an almost four-fold increase in the (crack-initiation) fracture toughness, approaching that of the coarse-grained alloys.
7. Above the ductile-brittle transition temperature the morphology and distribution of α-Mo grains becomes a less important factor in the development of toughness; instead, the volume fraction of the highly-ductile α-Mo phase determines the fracture toughness.
8. Further optimization of these alloys is still required to tailor their microstructures for the mutually-exclusive requirements of oxidation resistance, creep resistance and damage tolerance. Specifically, for optimum oxidation resistance, three-phase alloys with very small, discontinuous grains are required, whereas for creep resistance, small, discontinuous islands of α-Mo within a large-grained intermetallic matrix are superior. The most damage-tolerant microstructure, conversely, consists of large, continuous α-Mo grains as the matrix phase.

4.6 References

1. D. M. Dimiduk and J. H. Perepezko: 'Mo-Si-B alloys: Developing a revolutionary turbine-engine material', *MRS Bulletin*, 2003, **28**(9), 639-645.
2. H. Choe, J. H. Schneibel, and R. O. Ritchie: 'On the fracture and fatigue properties of Mo-Mo_3Si-Mo_5SiB_2 refractory intermetallic alloys at ambient to elevated temperatures (25°C-1300°C)', *Metallurgical and Materials Transactions A*, 2003, **34A**(2), 225-239.
3. H. Nowotny, E. Dimakopoulou, and H. Kudielka: 'Untersuchungen in den Dreistoffsystemen: Molybdän-Silizium-Bor, Wolfram-Silizium-Bor und in dem System: VSi2-TaSi2', *Mh. Chem*, 1957, **88**, 180-192.
4. M. Akinc, M. K. Meyer, M. J. Kramer, A. J. Thom, J. J. Huebsch, and B. Cook: 'Boron-doped molybdenum silicides for structural applications', *Materials Science and Engineering*, 1999, **A261**, 16-23.
5. M. Meyer, M. Kramer, and M. Akinc: 'Boron-doped molybdenum silicides', *Advanced Materials*, 1996, **8**(1), 85-88.
6. M. K. Meyer and M. Akinc: 'Isothermal oxidation behavior of Mo-Si-B intermetallics at 1450°C', *Journal of the American Ceramics Society*, 1996, **79**(10), 2763-2766.

7. M. K. Meyer, A. J. Thom, and M. Akinc: 'Oxide scale formation and isothermal oxidation behavior of Mo-Si-B intermetallics at 600-1000°C', *Intermetallics*, 1999, **7**, 153-162.
8. J. H. Schneibel, C. T. Liu, L. Heatherly, and M. J. Kramer: 'Assessment of processing routes and strength of a 3-phase molybdenum boron silicide (Mo_5Si_3-Mo_5SiB_2-Mo_3Si)', *Scripta Materialia*, 1998, **38**(7), 1169-1176.
9. D. Berczik: 'Method for enhancing the oxidation resistance of a molybdenum alloy, and a method of making a molybdenum alloy', Patent 5,595,616, United States, 1997.
10. D. Berczik: 'Oxidation resistant molybdenum alloy', Patent 5,693,156, United States, 1997.
11. A. P. Alur and K. S. Kumar: 'Monotonic and cyclic crack growth response of a Mo-Si-B alloy', *Acta Materialia*, 2006, **54**, 385-400.
12. P. Jain, A. P. Alur, and K. S. Kumar: 'High temperature compressive flow behavior of a Mo-Si-B solid solution alloy', *Scripta Materialia*, 2006, **54**, 13-17.
13. K. S. Kumar and A. P. Alur: 'Deformation behavior of a two-phase Mo-Si-B alloy', *Intermetallics*, 2007, **15**, 687-693.
14. T. G. Nieh, J. G. Wang, and C. T. Liu: 'Deformation of a multiphase Mo-9.4Si-13.8B alloy at elevated temperatures', *Intermetallics*, 2001, **9**, 73-79.
15. H. Choe, D. Chen, J. Schneibel, and R. O. Ritchie: 'Ambient to high temperature fracture toughness and fatigue-crack propagation behavior in a Mo-12Si-8.5B (at.%) intermetallic', *Intermetallics*, 2001, **9**, 319-329.
16. J. H. Schneibel, M. J. Kramer, Ö. Ünal, and R. N. Wright: 'Processing and mechanical properties of a molybdenum silicide with the composition Mo-12Si-8.5B (at.%)', *Intermetallics*, 2001, **9**, 25-31.
17. J. H. Schneibel, M. J. Kramer, and D. S. Easton: 'A Mo-Si-B intermetallic alloy with a continuous α-Mo matrix', *Scripta Materialia*, 2002, **46**, 217-221.
18. J. H. Schneibel, R. O. Ritchie, J. J. Kruzic, and P. F. Tortorelli: 'Optimization of Mo-Si-B intermetallic alloys', *Metallurgical and Materials Transactions A*, 2005, **36A**(3), 525-531.
19. J. J. Kruzic, J. H. Schneibel, and R. O. Ritchie: 'Role of microstructure in promoting fracture and fatigue resistance in Mo-Si-B alloys', *Materials Research Society Symposium Proceedings*, 2005, **842**, S2.9.1-S2.9.6.
20. J. J. Kruzic, J. H. Schneibel, and R. O. Ritchie: 'Fracture and fatigue resistance of Mo-Si-B alloys for ultrahigh temperature structural applications', *Scripta Materialia*, 2004, **50**, 459-464.
21. J. J. Kruzic, J. H. Schneibel, and R. O. Ritchie: 'Ambient to elevated temperature fracture and fatigue properties of Mo-Si-B alloys: Role of microstructure', *Metallurgical and Materials Transactions A*, 2005, **36A**(9), 2293-2402.

22. P. Jéhanno, M. Heilmaier, and H. Kestler: 'Characterization of an industrially processed Mo-based silicide alloy', *Intermetallics*, 2004, **12**, 1005-1009.
23. P. Jéhanno, M. Heilmaier, H. Kestler, M. Böning, A. Venskutonis, B. Belway, and M. Jackson: 'Assessment of a powder metallurgical processing route for refractory metal silicide alloys', *Metallurgical and Materials Transactions A*, 2005, **36A**(3), 515-523.
24. P. Jéhanno, M. Heilmaier, H. Saage, M. Böning, H. Kestler, J. Freudenberger, and S. Drawin: 'Assessment of the high temperature deformation behavior of molybdenum silicide alloys', *Materials Science and Engineering*, 2007, **A463**, 216-223.
25. M. Krüger, S. Franz, H. Saage, M. Heilmaier, J. H. Schneibel, P. Jéhanno, M. Böning, and H. Kestler: 'Mechanically alloyed Mo-Si-B alloys with a continuous α-Mo matrix and improved mechanical properties', *Intermetallics*, 2008, **16**, 933-941.
26. P. Jéhanno, M. Böning, H. Kestler, M. Heilmaier, H. Saage, and M. Krüger: 'Molybdenum alloys for high temperature applications in air', *Powder Metallurgy*, 2008, **51**(2), 99-102.
27. M. R. Middlemas and J. K. Cochran: 'Dense, fine-grain Mo-Si-B alloys from nitride-based reactions', *JOM*, 2008, **28**(7), 19-24.
28. M. R. Middlemas, J. K. Cochran, P. Jain, and K. S. Kumar: 'Strength and oxidation resistance of Mo-Si-B alloys produced by reaction synthesis', *TMS 2010 139th Annual Meeting & Exhibition - Supplemental Proceedings, Vol 1: Materials Processing and Properties*, 2010, 859-866.
29. V. Supatarawanich, D. R. Johnson, and C. T. Liu: 'Effects of microstructure on the oxidation behavior of multiphase Mo-Si-B alloys', *Materials Science and Engineering*, 2003, **A344**, 328-339.
30. V. Supatarawanich, D. R. Johnson, and C. T. Liu: 'Oxidation behavior of multiphase Mo-Si-B alloys', *Intermetallics*, 2004, **12**, 721-725.
31. F. A. Rioult, S. D. Imhoff, R. Sakidja, and J. H. Perepezko: 'Transient oxidation of Mo-Si-B alloys: Effect of the microstructure size scale', *Acta Materialia*, 2009, **57**, 4600-4613.
32. O. Hassomeris, G. Schumacher, M. Kruger, M. Heilmaier, and J. Banhart: 'Phase continuity in high temperature Mo-Si-B alloys: A FIB-Tomography Study', *Intermetallics*, 2011, **19**(4), 470-475.
33. 'ASTM E1820-08. Annual Book of ASTM Standards, Vol. 03.01: Metals - Mechanical Testing; Elevated and Low-temperature Tests; Metallography'; 2008, West Conshohocken, Pennsylvania, USA, ASTM International.
34. C. F. Shih: 'Relationships between the J-integral and the crack opening displacement for stationary and extending cracks', *J. Mech. Phys. Solids*, 1981, **29**(4), 205-326.

35. R. Mitra, A. K. Srivastava, N. E. Prasad, and S. Kumari: 'Microstructure and mechanical behavior of reaction hot pressed multiphase Mo-Si-B and Mo-Si-B-Al intermetallic alloys', *Intermetallics*, 2006, **14**, 1461-1471.
36. P. G. Biragoni and M. Heilmaier: 'FEM-simulation of real and artificial microstructures of Mo-Si-B alloys for elastic properties', *Advanced Engineering Materials*, 2007, **9**(10), 882-887.
37. D. Chen, C. J. Gilbert, and R. O. Ritchie: '*In-situ* measurement of fatigue crack growth rates in a silicon carbide ceramic at elevated temperatures using a DC potential system', *Journal of Testing & Evaluation*, 2000, **28**(4), 236-241.
38. J. H. Schneibel, M. P. Brady, J. J. Kruzic, and R. O. Ritchie: 'On the improvement of the ductility of molybdenum by spinel ($MgAl_2O_4$) particles', *Zeitschrift fur Metallkunde*, 2005, **96**(6), 632-637.
39. J. J. Kruzic, R. A. Marks, M. Yoshiya, A. M. Glaeser, R. M. Cannon, and R. O. Ritchie: 'Fracture and fatigue behavior at ambient and elevated temperatures of alumina bonded with copper/niobium/copper interlayers', *Journal of the American Ceramic Society*, 2002, **85**(10), 2531-2541.
40. A. G. Evans: 'Perspective on the development of high-toughness ceramics', *J. Am. Ceram. Soc.*, 1990, **73**, 187-206.
41. M. E. Launey and R. O. Ritchie: 'On the fracture toughness of advanced materials', *Adv. Mater.*, 2009, **21**, 2103-2110.
42. R. O. Ritchie: 'Mechanisms of fatigue crack-propagation in metals, ceramics and composites: role of crack tip shielding', *Materials Science & Engineering A*, 1988, **103**, 15-28.
43. R. O. Ritchie: 'Mechanisms of fatigue-crack propagation in ductile and brittle solids', *International Journal of Fracture*, 1999, **100**, 55-83.
44. J. P. Campbell, R. O. Ritchie, and K. T. Venkateswara Rao: 'The effect of microstructure on fracture toughness and fatigue crack growth behavior in α-titanium aluminide based intermetallics', *Metallurgical and Materials Transactions A*, 1999, **30**(3), 563-577.
45. K. S. Chan and D. L. Davidson: 'Improving the fracture toughness of constituent phases and Nb-based in-situ composites by a computational alloy design approach', *Metallurgical and Materials Transactions A*, 2003, **34A**(9), 1833-1849.
46. I. Rosales and J. H. Schneibel: 'Stoichiometry and mechanical properties of Mo_3Si', *Intermetallics*, 2000, **8**, 885-889.
47. K. Ihara, K. Ito, K. Tanaka, and M. Yamaguchi: 'Mechanical properties of Mo_5SiB_2 single crystals', *Materials Science and Engineering*, 2002, **A329-331**, 222-227.
48. G. Y. Lin and K. S. Chan: 'Finite-element method simulation of effects of microstructure, stress state, and interface strength on flow localization and constraint development in Nb/Cr_2Nb *in situ* composites', *Metallurgical and Materials Transactions A*, 1999, **30**(12), 3239-3251.

49. M.-Y. He and J. W. Hutchinson: 'Crack deflection at an interface between dissimilar elastic materials', *International Journal of Solids Structures*, 1989, **25**(9), 1053-1067.
50. A. Ziegler, J. C. Idrobo, M. K. Cinibulk, C. Kisielowski, N. D. Browning, and R. O. Ritchie: 'Interface structure and atomic bonding characteristics in silicon nitride ceramics', *Science*, 2004, **306**(5702), 1768-1770.
51. P. Jain and K. S. Kumar: 'Dissolved Si in Mo and its effects on the properties of Mo-Si-B alloys', *Scripta Materialia*, 2010, **62**(1), 1-4.
52. D. Sturm, M. Heilmaier, J. H. Schneibel, P. Jéhanno, B. Skrotzki, and H. Saage: 'The influence of silicon on the strength and fracture toughness of molybdenum', *Materials Science and Engineering A*, 2007, **463**, 107-114.
53. M. K. Miller, E. A. Kenik, M. S. Mousa, K. F. Russell, and A. J. Bryhan: 'Improvement in the ductility of molybdenum alloys due to grain boundary segregation', *Scripta Materialia*, 2002, **46**, 299-303.
54. H. Saage, M. Krüger, D. Sturm, M. Heilmaier, J. H. Schneibel, E. George, L. Heatherly, C. Somsen, G. Eggeler, and Y. Yang: 'Ductilization of Mo-Si solid solutions manufactured by powder metallurgy', *Acta Materialia*, 2009, **57**(13), 3895-3901.
55. S. Burk, B. Gorr, V. B. Trindade, and H.-J. Christ: 'Effect of Zr addition on the high temperature oxidation behavior of Mo-Si-B alloys', *Oxid. Met.*, 2010, **73**, 163-181.
56. S. Burk, B. Gorr, and H.-J. Christ: 'High temperature oxidation of Mo-Si-B alloys: Effect of low and very low oxygen partial pressures', *Acta Materialia*, 2010, **58**, 6154-6165.
57. P. Jéhanno, M. Heilmaier, H. Saage, H. Heyse, M. Böning, H. Kestler, and J. H. Schneibel: 'Superplasticity of a multiphase refractory Mo-Si-B alloy', *Scripta Materialia*, 2006, **55**, 525-528.
58. J. A. Shields, P. Lipetzky, and A. J. Mueller: 'Fracture toughness of 6.4 mm (0.25 inch) arc-cast molybdenum and molybdenum-TZM plate at room temperature and 300°C', Proceedings of the 15th International Plansee Seminar, Reutte, Austria, 2001, Plansee Holding AG, 187-197.
59. L. S. Sigl, P. A. Mataga, B. J. Dalgleish, R. M. McMeeking, and A. G. Evans: 'On the toughness of brittle materials reinforced with a ductile phase', *Acta Metallurgica*, 1988, **36**(4), 945-953.
60. M. R. Middlemas and J. K. Cochran: 'The microstructural engineering of Mo-Si-B alloys produced by reaction synthesis', *JOM Journal of the Minerals, Metals and Materials Society*, 2010, **62**(10), 20-24.
61. M. R. Middlemas, J. K. Cochran, and A. M. Gokhale: 'Microstructural engineering of Mo-Si-B alloys produced using nitride-based reactions', *TMS 2009*

138th Annual Meeting & Exhibition - Supplemental Proceedings, Vol 1: Materials Processing and Properties, 2009, 177-184.

62. J. K. Cochran, W. L. Daloz, and P. E. Marshall: 'Novel oxidation resistant Mo-Mo_2B-Silica and Mo-Mo_2B-Silicate composites for high temperature applications', *JOM*, 2011, **63**(12), Submitted.
63. Z. Li and L. M. Peng: 'Ultra-high temperature Mo-Si-B alloys -- Synthesis, microstructural and mechanical characterization', *Materials Letters*, 2008, **62**, 2229-2232.
64. K. Ito, M. Kumagai, T. Hayashi, and M. Yamaguchi: 'Room temperature fracture toughness and high temperature strength of T2/Mo_{ss} and $(Mo,Nb)_{ss}$/T1/T2 eutectic alloys in the Mo-Si-B system', *Scripta Materialia*, 2003, **49**, 285-290.
65. V. Supatarawanich, D. R. Johnson, M. A. Dayananda, and C. T. Liu: 'Processing and properties of multiphase Mo-Si-B alloys', *Materials Science Forums*, 2003, **426-432**, 4301-4306.
66. J. H. Schneibel, J. J. Kruzic, and R. O. Ritchie: 'Mo-Si-B alloy development', Proceedings of the 17th Annual Conference on Fossil Energy Materials, Knoxville, TN, 2003, National Energy Technology Laboratory.
67. S. C. Okumus, Ö. Ünal, M. J. Kramer, and M. Akinc: 'Mechanical properties of plasma-sprayed Mo_5Si_3-MoB-$MoSi_2$ system', in 'Innovative Processing and Synthesis of Ceramics, Glasses, and Composites II', (eds. N. P. Bansal, et al.), 347-360; 1999, Westerville, Ohio, The American Ceramic Society.

4.7 Figures

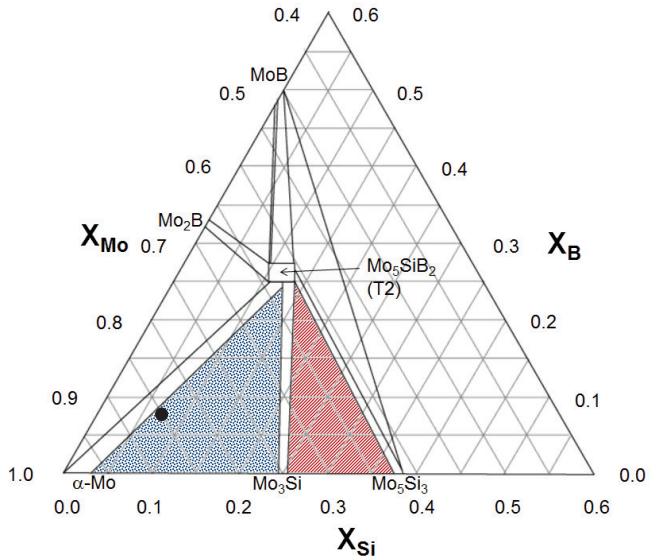

Fig. 4.1: Mo-rich portion of the Mo-Si-B phase diagram. Two alloy families have been studied extensively: Mo3Si-Mo5Si3-Mo5SiB2 (red)[4-7] and α-Mo-Mo_3Si-Mo_5SiB_2 (blue).[8,9] The composition used in this study, Mo-3Si-1B wt.% (Mo-8.9Si-7.7B at.%) is shown.

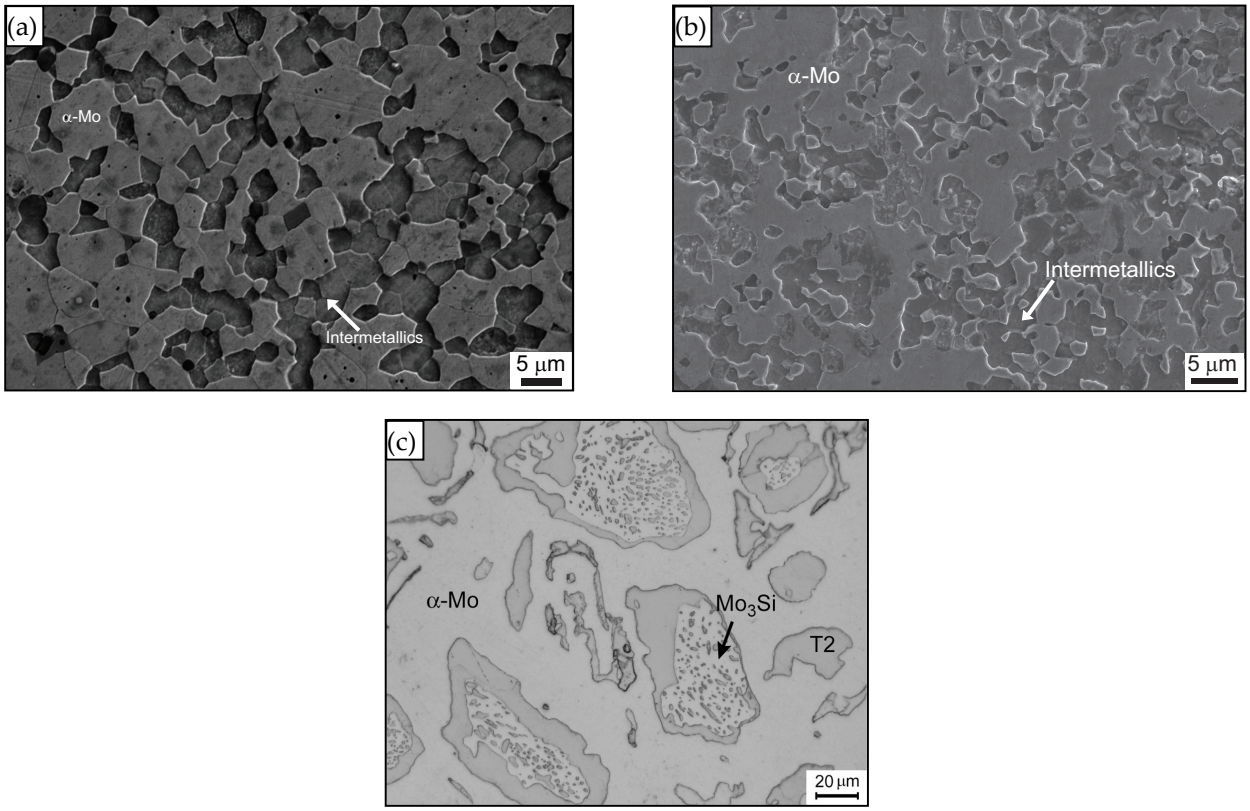

Fig. 4.2: Micrographs of the microstructures of (a) ULTMAT,[25] (b) Middlemas[28] and (c) Kruzic[21] Mo-3Si-1B (wt.%) alloys. The ULTMAT and Middlemas alloys exhibit a continuous α-Mo matrix (50 vol.%, light gray) interspersed with intermetallic grains (~50 vol.% dark gray). The 5-20 μm grains of these alloys are roughly an order of magnitude smaller than those in coarser-grained Kruzic alloy. All samples were etched in Murakami's reagent to reveal the grain morphology.

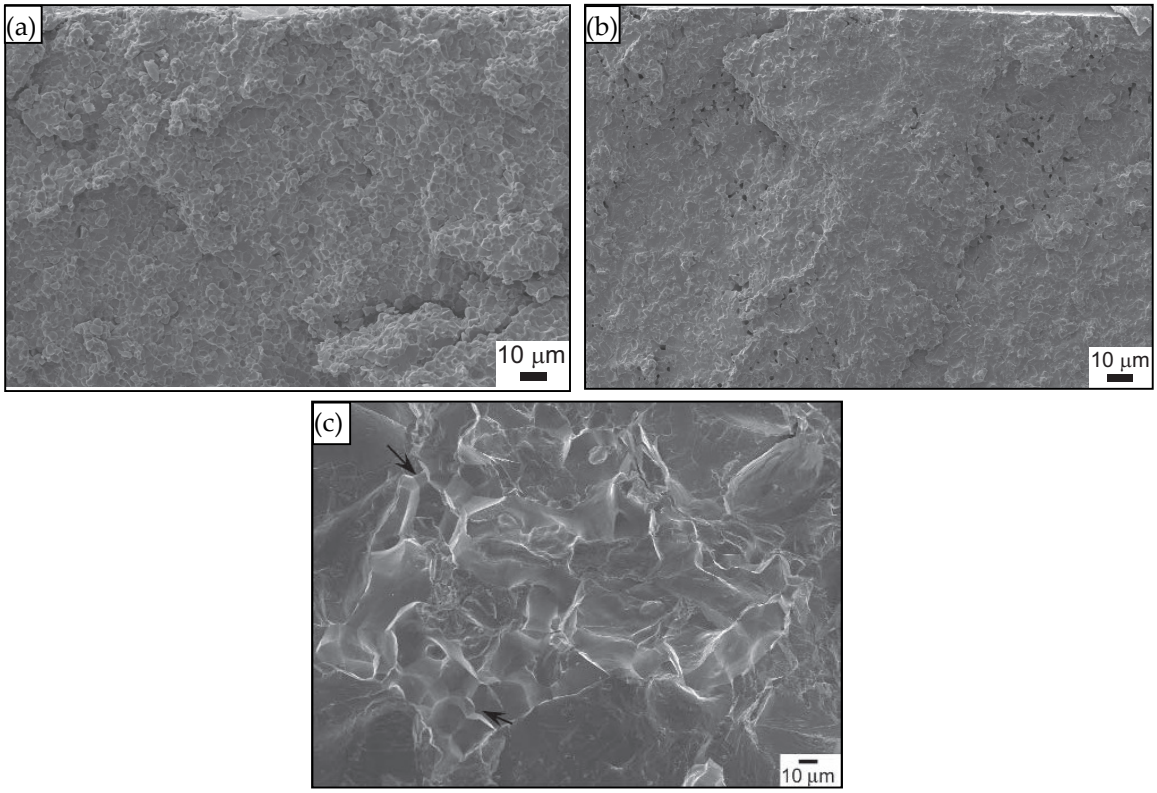

Fig. 4.3: Scanning electron micrographs of room-temperature fracture surface of the (a) ULTMAT,[25] (b) Middlemas[28] and (c) Kruzic alloys.[21] Note the significant increase in the amount of intergranular fracture for the ULTMAT and Middlemas alloys, as compared to the Kruzic alloy (indicated by arrows). At room temperature, the ULTMAT and Middlemas alloys have much lower crack-initiation fracture toughnesses than the Kruzic alloy, and exhibit negligible rising R-curve behavior, *i.e.*, unlike the coarse-grained Kruzic alloy, the fine-grained alloys do not tolerate any subcritical cracking prior to catastrophic failure.

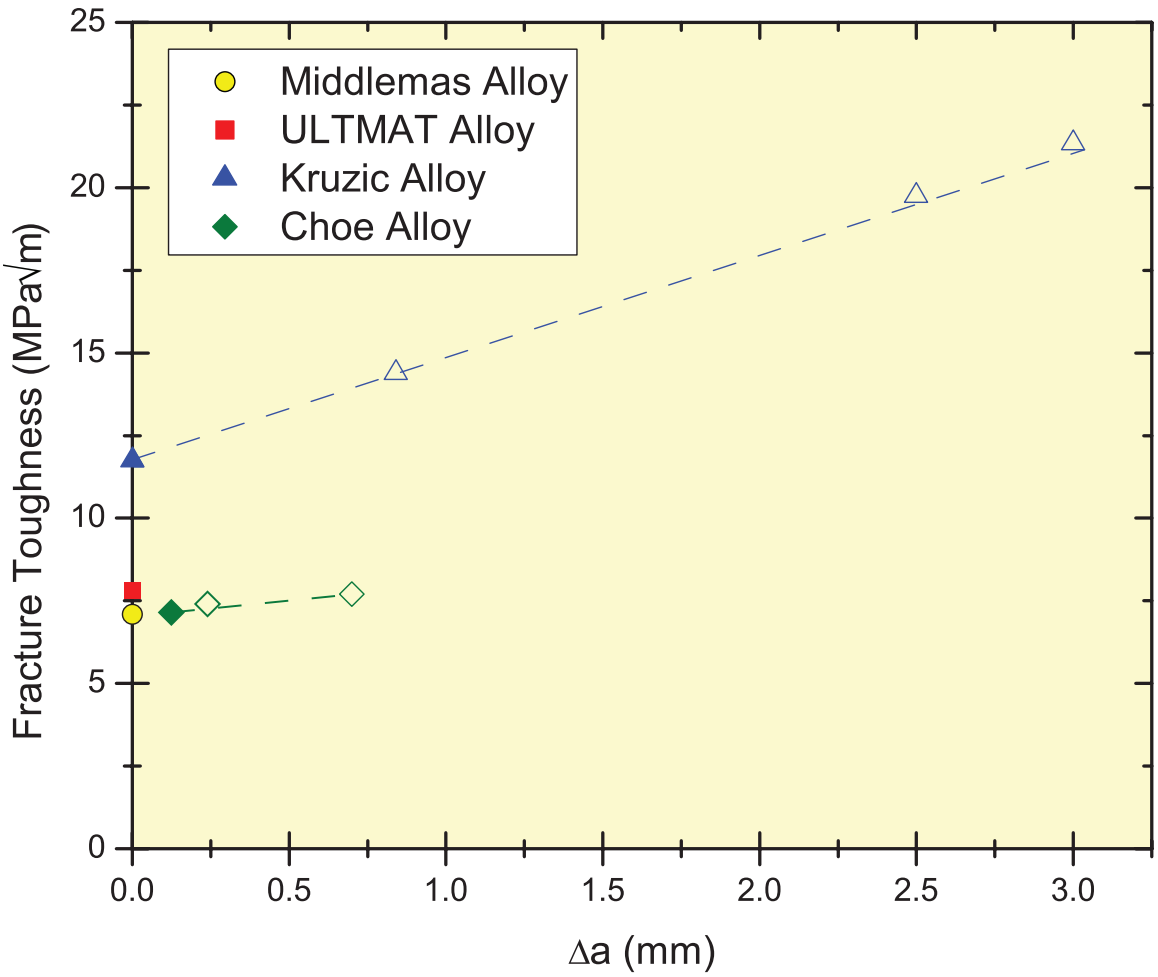

Fig. 4.4: Room temperature fracture toughness versus crack extension for Mo-Si-B alloys. Crack initiation toughnesses are plotted as closed symbols, while crack growth toughnesses are open symbols. The coarse-grained Kruzic alloy[21] displayed rising toughness with crack extension, caused by an accumulation of uncracked ligaments in the crack wake. Similar, but less potent, toughening was observed by Choe, *et al.*[2] for their Mo-12Si-8.5B (at.%) alloy which contained ~21 vol.% discontinuous α-Mo. Neither the ULTMAT nor Middlemas alloys displayed any stable crack growth, even though they contained the same ~55 vol.% continuous α-Mo phase as the Kruzic alloy. *NB*: The tests performed on the ULTMAT and Middlemas alloys utilized radiused micro-notches, while the Kruzic and Choe materials were fatigue pre-cracked.

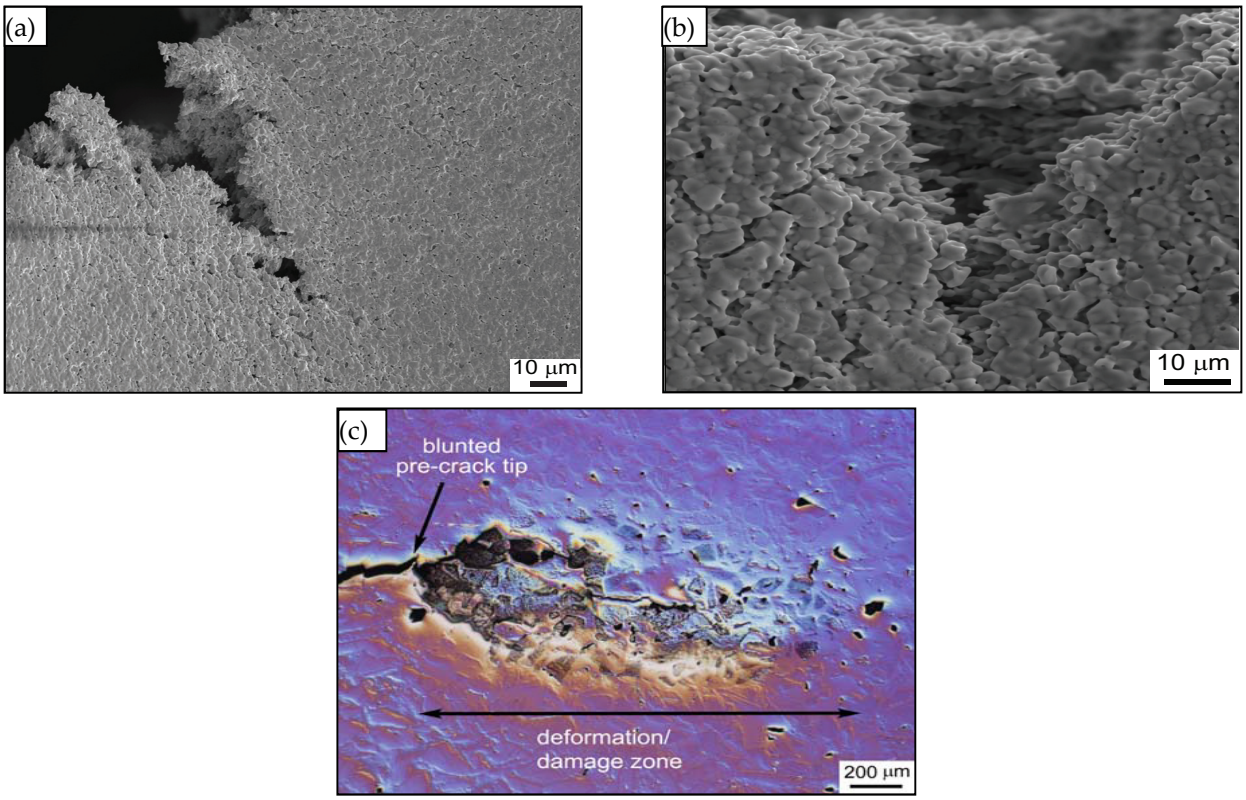

Fig. 4.5: Crack profiles near crack initiation at 1300°C for the (a) ULTMAT and (b) Middlemas alloys, as compared to similar damage in the (c) Kruzic alloy.[21] At 1300°C, the increased ductility of α-Mo phase allows for large-scale plastic deformation and blunting of the crack tip. The initiation toughness values for each alloy, estimated from the crack-tip opening displacements, were approximately the same.

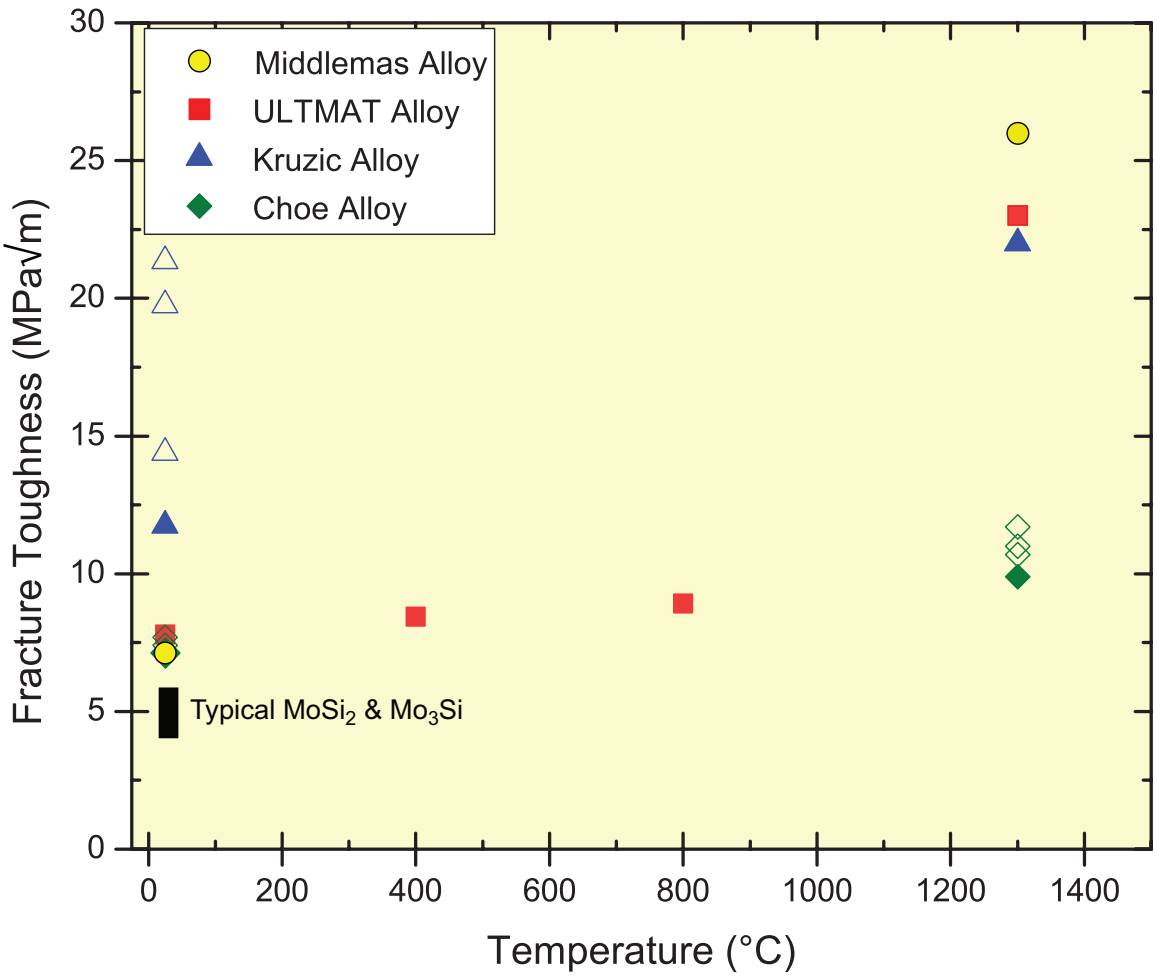

Fig. 4.6: Fracture toughness as a function of temperature for Mo-Si-B alloys. Crack-initiation toughnesses (closed symbols) are plotted along with any increases in toughness with crack extension (open symbols). The highest room temperature toughness value for the Kruzic alloy was obtained after more than 3 mm of stable crack growth.[21] At low temperatures, neither the ULTMAT nor the Middlemas alloy exhibited any stable crack growth prior to unstable fracture. The ductile-brittle transition temperature for these materials is ~1000°C,[25] so only moderate gains in initiation toughness are expected below this temperature, as demonstrated by the ULTMAT alloy. At 1300°C, the enhanced ductility of the α-Mo phase markedly improves the initiation toughness of alloys containing ~50 vol.% α-Mo. At this temperature, the volume fraction of α-Mo becomes a more important factor in developing toughness (*intrinsically* from plasticity) than the distribution and morphology of α-Mo grains (which leads to *extrinsic* toughening from mechanisms such as crack bridging).

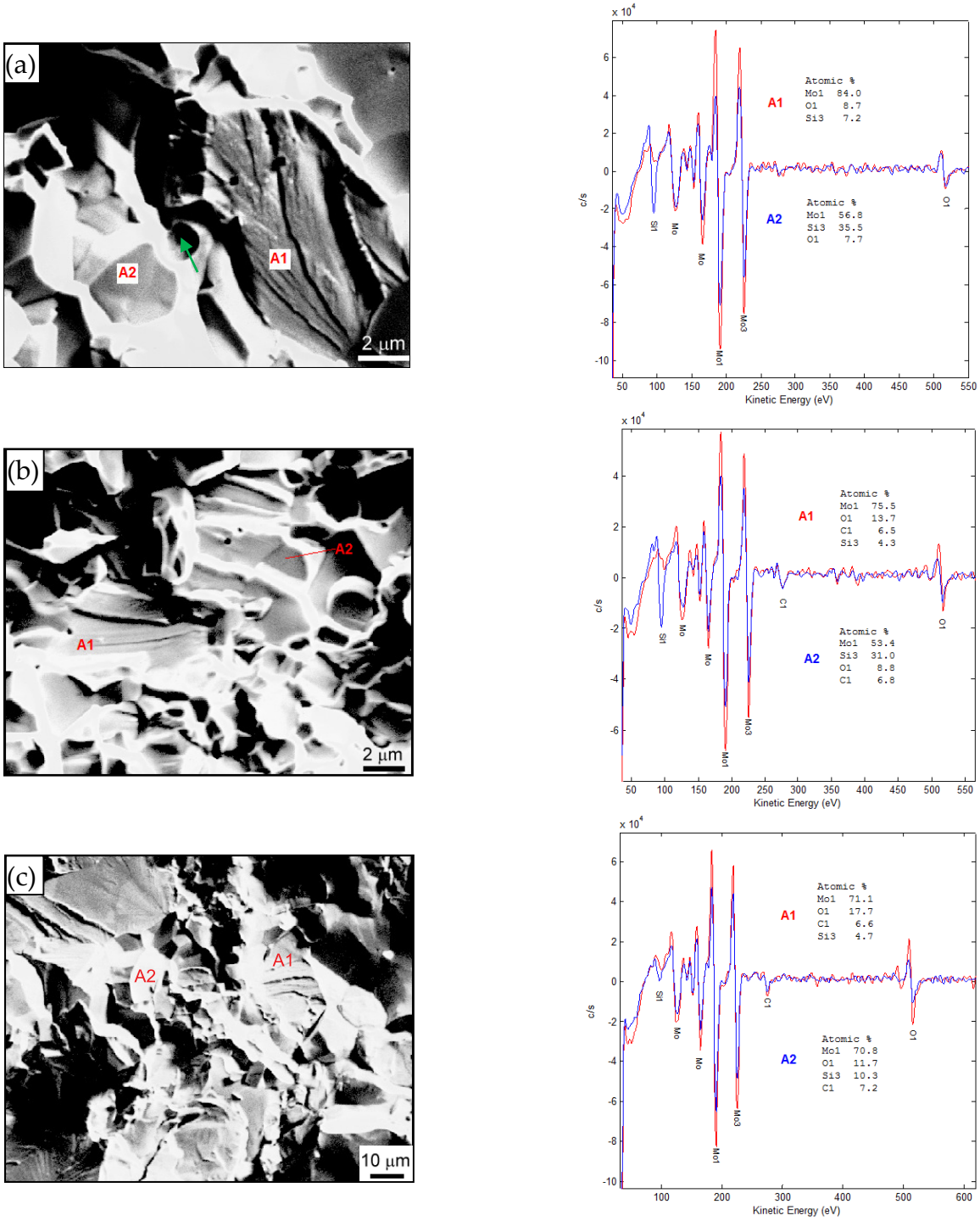

Fig. 4.7: Fracture surface and associated AES spectra for ULTMAT (a), Middlemas (b) and Kruzic (c) alloys. Spectra were collected from both α-Mo grain interior (A1) and grain boundary (A2) material. While the spectra only provide qualitative impurity information, it is important to note the significantly higher silicon levels in the grain boundaries than the α-Mo grain interiors. More telling is the significant difference in grain-boundary silicon levels of the ULTMAT and Middlemas alloys as compared to the Kruzic alloy. Si is known to embrittle Mo and lead to intergranular failure,[54] implying a possible cause for the reduced room-temperature toughness of the ULTMAT and Middlemas alloys. The green arrow in (a) represents a SiO_x oxide particle that has been pulled out. Only a few silicon oxides were found.

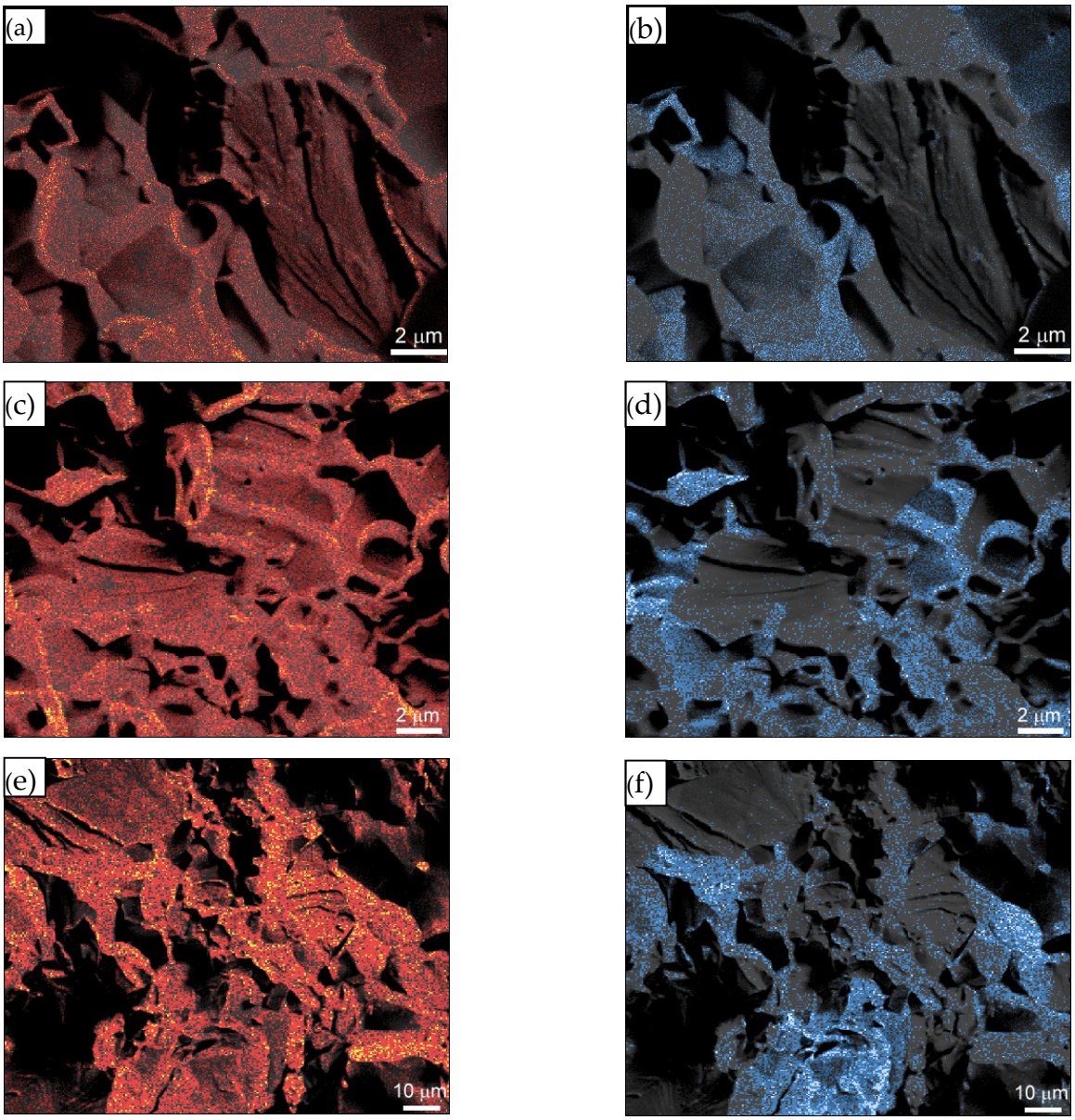

Fig. 4.8: Auger electron spectroscopy maps of impurity content on grain boundaries overlaid on the corresponding room-temperature fracture surfaces for the (a&b) ULTMAT, (c&d) Middlemas and (e&f) Kruzic alloys. Areas of high oxygen concentration (red) and high silicon content (blue) are shown. Both Si and O segregate to grain boundaries, reducing interfacial strength and increasing the occurrence of intergranular fracture. Note the high concentrations of Si in the regions that fractured intergranularly, while almost no Si is found in regions that fractured transgranularly. No effort has been made to account for surface adsorption of oxygen from the surrounding atmosphere (vacuum > 10^{-9} torr) during testing, so the oxygen levels are artificially high. Also note the difference in scale for (e) & (f).

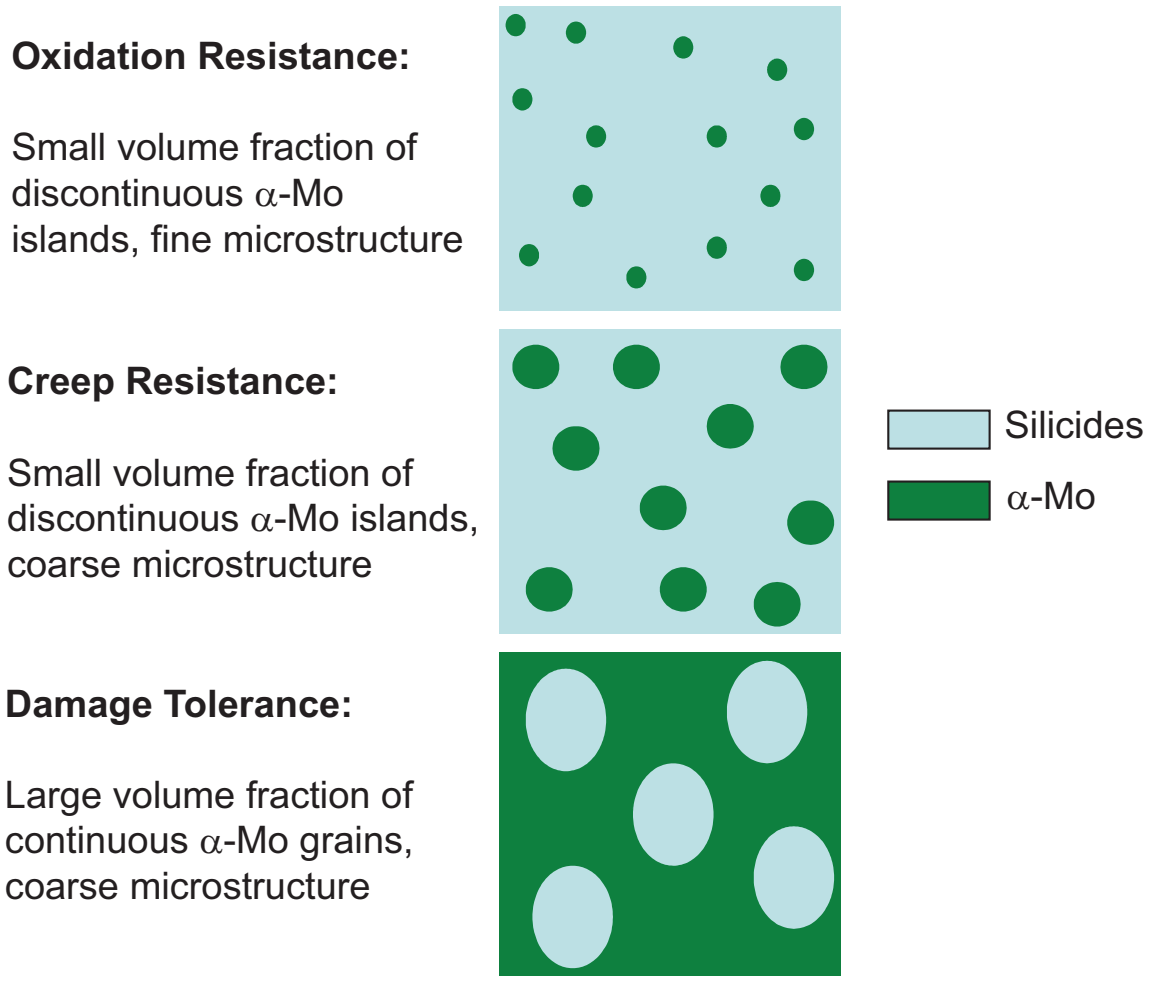

Fig. 4.9: Schematic illustrations of the ideal microstructures to improve oxidation resistance, creep resistance and damage tolerance of Mo-Si-B alloys. The morphological considerations for improvement in each area are mutually exclusive, so optimization of the properties of each phase is necessary.[18]

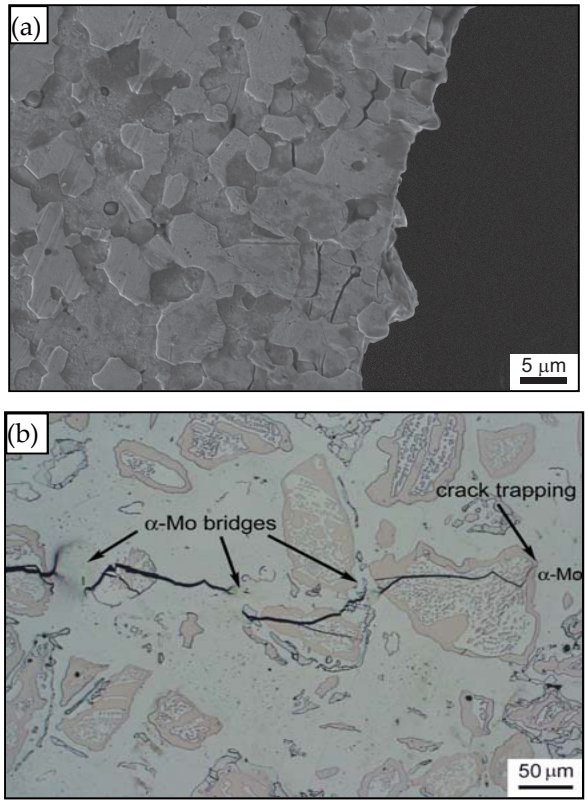

Fig. 4.10: Crack paths during fracture at room temperature in the (a) fine-grained ULTMAT alloy and (b) coarse-grained Kruzic alloy.[21] Note the order of magnitude difference in scale. The coarse grains in (b) trap an advancing crack, requiring re-initiation to continue crack propagation. The resulting uncracked ligaments then act to bridge the crack, thereby carrying load that would otherwise be used to further crack extension; such extrinsic toughening leads to rising R-curve behavior. The fine grains in ULTMAT (and Middlemas) alloys are ineffective in generating substantial crack bridges, and therefore do not act as impediments to crack extension; this leads to a lower toughness at low temperatures, even though the volume fraction of ductile α-Mo grains is the same. Samples have been etched in Murakami's reagent to reveal the grain structure. Crack growth occurred from top to bottom in (a) and left to right in (b).

Chapter 5 : Summary

Ceramic-metal composites (such as the Al_2O_3-Nb constructs discussed in Chapter 1), functionally-graded material joints between dissimilar ceramic materials (Chapter 2) and intermetallic *in-situ* composites like the Mo-Si-B alloys discussed in Chapters 3 & 4 have the potential to serve as structural materials in ultra-high temperature applications, though not without further study.

Nanocrystalline Al_2O_3, especially with the addition of single-walled carbon nanotubes, is not a viable material for highly critical parts or load-bearing applications where damage tolerance is required. While the ultra-fine grain size is advantageous for developing high strength, the very low toughness of these materials hinders their use. Small additions of a more ductile material, for instance a refractory metal like Nb, can improve the toughness of these materials, but the toughness gains for the morphology studied in Chapter 1 are rather limited. Plastic constraint by the hard Al_2O_3 grains prevents plastic deformation of the ductile phase from occurring on a large scale. As a result, the crack blunting (and thus toughness increase) afforded by this phase is rather limited. A ceramic-metal composite composed of micron-grained Al_2O_3 dispersed with elongated Nb (or other refractory metal) grains would be much more damage tolerant than the current morphology.

While carbon nanotubes provide some measure of electrical conductivity (a property that may be desired in some applications), they are highly detrimental to the mechanical properties of Al_2O_3-Nb composites. Since the nanotubes have a tendency to collect on grain boundaries and agglomerate, they act as internal flaws and initiation sites for cracks. The potential for crack bridging by nanotubes was the initial motivation for their addition to the composites, but the method by which the nanotubes were introduced was not conducive to the formation of bridges. To act as effective bridges, the nanotubes must be highly aligned perpendicular to the direction of crack growth. Otherwise, they act as brittle inclusions. No care was taken to align the nanotubes and new processing methods must be developed to produce highly aligned morphologies.

Sialon polytypoids have been successfully used to create strong joinings of Al_2O_3 and Si_3N_4. These joints maintain strength at high temperatures, unlike previous attempts where softening of glassy grain boundary phases severely lowered the high temperature strength of the joint. These functionally-graded materials utilize a gradient of mechanical properties across the joint, thereby minimizing the layer to layer difference in properties. However, the joints described in Chapter 2 are very small.

Further research needs to be performed to optimize the formation of thicker joints. Likewise, no effort was taken to study the thermal cycling response of these materials. Nor was the toughness of these joints studied. Future work needs to concentrate on these properties if viable functionally-graded joints are to be developed.

The bulk of the research relayed here focused on the fracture behavior of two Mo-3Si-1B (wt.%) alloys at ambient and elevated temperature. It was shown that at room temperature, large contiguous grains of ductile phase are required for high toughness and resistance to crack propagation. A high volume fraction of ductile phase is by itself not a sufficient requirement for high toughness. The small grains of the ULTMAT and Middlemas alloys do not provide adequate impediment to crack advance. Plastic constraint of the ductile phase limits its ability to plastically deform and thus blunt any cracks which interact with the ductile phase, a phenomenon also seen in Chapter 1. Grain boundary segregation of Si and O further inhibits toughness by lowering grain boundary adhesion, thus embrittling the grain boundaries.

At elevated temperature (above ~ 1150°C), the ductility of α -Mo is greatly increased, to the point that the distribution of this phase becomes secondary to the volume fraction of ductile phase in the development of toughness. The initiation toughness values for the two fine-grained alloys (ULTMAT and Middlemas) are approximately the same as the much coarser-grained Kruzic alloy. In fact, the alloys were able to plastically deform to such a degree that the underlying assumptions of linear elastic behavior were no longer applicable. It is obvious that Mo-3Si-1B (wt.%) alloys display excellent high temperature toughness, but the room temperature toughness and oxidation resistance of these alloys can be improved.

The microstructure morphology which provides the best mechanical response also provides the worst oxidation resistance. Some variety of pretreatment, be it Si pack cementation, pre-oxidation in low oxygen partial pressures or physical deposition of a silicate layer, will be required to limit the mass loss of these alloys in oxidative environments. Laser re-melting of the surface to form a thin, fine-grained region coating a coarse microstructure would also improve the oxidation resistance, but this coating would not be as effective as a borosilicate coating, since mass would be lost by the re-melted alloy as it formed a borosilicate coating *in-situ* during the initial exposure to an oxidizing environment. Research studying the oxidation resistance of the more damage tolerant morphologies once coated will need to be performed.

Segregation of Si and O to grain boundaries needs to be addressed if damage tolerant Mo-Si-B alloys are to be manufactured on an industrial scale. The most damage-tolerant alloys tested required a very complex processing route involving vacuum annealing of arc-melted and ground Mo-Si-B powders, which produced

material with very little Si in the grain boundaries. But, the complexity and processing steps necessary to create this alloy limits the shapes that can be produced by this method, as well as the quantities that can be manufactured. The mechanical alloying and reaction synthesis methods described in Chapters 3 and 4 provide the path forward, if the segregation of Si and O can be limited. However, the ultra-fine grain sizes used so far are not practical and must be coarsened to create a useful structural material.

One way to reduce the amount of Si segregation is to remove elemental Si as one of the initial alloy constituents. Cochran, *et al.*, in a soon-to-be-published work (J.K. Cochran, W.L. Daloz, P.E. Marshall, JOM, 63 (2011) Submitted), studied the mechanical behavior and oxidation response of Mo-Mo_2B-$2Al_2O_3 \cdot SiO_2$ and Mo-Mo_2B-$SrO \cdot Al_2O_3 \cdot (SiO_2)_2$ alloys. These alloys, which contain no elemental Si, displayed some room temperature ductility, as well as high temperature oxidation resistance, though both properties were not achieved in the same alloy. The most promising results were found for the Mo-Mo_2B-$SrO \cdot Al_2O_3 \cdot (SiO_2)_2$ alloys, but much work is required to optimize this alloys. With further study, these alloys may well prove the most viable ultra-high temperature intermetallic structural alloys.

Appendix: Collected Toughness Values

Ch. 4 Ref.	Material	Processing Technique	α-Mo vol.%	α-Mo Morphology	Test Method	Fracture Toughness, K_Q, MPa√m
63	Mo-5.2Si-0.7B	Reaction Hot-pressed	1.2	Discontinuous	3PB	7.5
63	Mo-5.5Si-1.4B	Reaction Hot-pressed	4.5	Discontinuous	3PB	6.6
63	Mo-5.8Si-2.2B	Reaction Hot-pressed	8.4	Discontinuous	3PB	5.2
64	Mo-3.4Si-2.6B	Directional Solidification (5 mm/hr.)	28	Discontinuous	3PB	11
65	Mo-3Si-1.2B	Hot-pressed powder	50	Discontinuous	4PB	9.5
65	Mo-5.4Si-1.3B	Hot-pressed powder	20	Discontinuous	4PB	6.1
16	Mo-4.2Si-1.1B	Cast and Annealed (1600°C/24 hr.)	38	Discontinuous	3PB, Chevron-notched	9.5
35	Mo-5.1Si-1.4B	Reaction Hot-Pressed	33	Discontinuous	3PB	5.0
35	Mo-1.1Al-4.3Si-1.1B	Reaction Hot-Pressed	35	Discontinuous	3PB	5.8
35	Mo-2.8Al-4.1Si-1.1B	Reaction Hot-pressed	39	Discontinuous	3PB	6.6
18	Mo-4.2Si-1.1B	Cast and Annealed (1600°C/24 hr.)	42	Discontinuous	3PB, Chevron-notched	9.0
18	Mo-4.2Si-1.1B-1.1Zr	Cast and Annealed (1600°C/24 hr.)	42	Discontinuous	3PB, Chevron-notched	12.4
18	Mo-4.2Si-1.1B-1.7Zr	Cast and Annealed (1600°C/24 hr.)	42	Discontinuous	3PB, Chevron-notched	13.5
18	Mo-4.2Si-1.1B-3.5Zr	Cast and Annealed (1600°C/24 hr.)	42	Discontinuous	3PB, Chevron-notched	12.6
66	Mo-4.2Si-1.1B-0.9Ti	Cast and Annealed (1600°C/24	42	Discontinuous	3PB, Chevron-notched	10.0

		hr.)				
2	Mo-4.2Si-1.1B	Arc-cast	38	Discontinuous	DC(T) 25°C	7.2
2	Mo-4.2Si-1.1B	Arc-cast	38	Discontinuous	DC(T) 25°C	7.8[#]
2	Mo-6.1Si-1.2B	HIPped Powder	21	Discontinuous	DC(T) 25°C	4.1
2	Mo-6.1Si-1.2B	HIPped Powder	21	Discontinuous	DC(T) 1300°C	8.1
2	Mo-6.1Si-1.2B	HIPped Powder (Mo & Mo-20Si-10B (at.%))	21	Discontinuous	DC(T) 25°C	5.7
2	Mo-6.1Si-1.2B	HIPped Powder (Mo & Mo-20Si-10B (at.%))	21	Discontinuous	DC(T) 1300°C	7.5
2	Mo-6.1Si-1.2B	HIPped Powder (Mo & Mo-20Si-10B (at.%))	21	Discontinuous	DC(T) 1300°C	7.7[#]
2	Mo-12.1Nb-4.2Si-1.1B	Arc cast	38	Discontinuous	DC(T) 25°C	6.3
2	Mo-12.1Nb-4.2Si-1.1B	Arc cast	38	Discontinuous	DC(T) 25°C	6.7[#]
2	Mo-4.2Si-1.1B	Arc Cast	38	Discontinuous	DC(T) 1300°C	9.7
2	Mo-4.2Si-1.1B	Arc Cast	38	Discontinuous	DC(T) 1300°C	11.7[#]
67	Mo-16.2Si-1.6B	Plasma-Sprayed	0[†]	N/A	4PB, Chevron-notched	4.1
17	Mo-7.6Si-1.5B[*]	Vacuum Annealed Powder	30	Continuous	3PB, Chevron-notched	14
65	Not Reported	Hot-pressed powder	78	Continuous	4PB	13.4
16	Mo-4.2Si-1.1B	Hot-pressed powder	38	Continuous	3PB, Chevron-notched	14.8
11	Mo-2Si-1B	PREP powder, isothermal forged	62	Continuous	3PB, 25°C	8

11	Mo-2Si-1B	PREP powder, annealed (1600°C/48 hr.)	62	Continuous	3PB, 25°C	9
11	Mo-2Si-1B	PREP powder, isothermal forged	62	Continuous	3PB, 600°C	13
11	Mo-2Si-1B	PREP powder, isothermal forged	62	Continuous	3PB, 1200°C	18
11	Mo-2Si-1B	PREP powder, isothermal forged	62	Continuous	3PB, 1400°C	25
21	Mo-4.1Si-1.6B	Vacuum Annealed Powder	37.5	Continuous	DC(T), 25°C	8.0
21	Mo-4.1Si-1.6B	Vacuum Annealed Powder	37.5	Continuous	DC(T), 25°C	~9
21	Mo-4.0Si-1.5B	Vacuum Annealed Powder	37.5	Continuous	DC(T), 25°C	7.5
21	Mo-4.0Si-1.5B	Vacuum Annealed Powder	37.5	Continuous	DC(T), 25°C	~9[#]
21	Mo-4.0Si-1.5B	Vacuum Annealed Powder	37.5	Continuous	DC(T), 1300°C	12.6
21	Mo-4.0Si-1.5B	Vacuum Annealed Powder	37.5	Continuous	DC(T), 1300°C	~15[#]
21	Mo-5.5Si-1.6B	Vacuum Annealed Powder	18.3	Continuous	DC(T), 25°C	5.0
21	Mo-5.5Si-1.6B	Vacuum Annealed Powder	18.3	Continuous	DC(T), 25°C	~8[#]
21	Mo-5.5Si-1.6B	Vacuum Annealed Powder	18.3	Continuous	DC(T), 1300°C	8.3
21	Mo-5.5Si-1.6B	Vacuum Annealed Powder	18.3	Continuous	DC(T), 1300°C	~9[#]

21	Mo-3.3Si-1.3B	Vacuum Annealed Powder	49.1	Continuous	DC(T), 25°C	9.8
21	Mo-3.3Si-1.3B	Vacuum Annealed Powder	49.1	Continuous	DC(T), 1300°C	35 (23)‡
21	Mo-2.2Si-1.0B	Vacuum Annealed Powder	~50	Continuous	DC(T), 25°C	12.0

* The material tested by Schneibel, *et al.*[17] had an initial powder composition of Mo-20Si-10B (at.%). During processing, Si was removed from the powder particles surface by vacuum annealing. No composition after vacuum annealing was reported by the authors.

† The plasma-sprayed Mo-Si-B alloy tested by Okumus, *et al.*[67] did not contain any α-Mo. It was composed instead of Mo_5Si_3, MoB and $MoSi_2$.

‡ The toughness value reported by Kruzic, *et al.*[21] for their alloy was an overestimate as it was based on a "rule of mixtures" calculation using the room temperature elastic modulus values. Moreover, the authors assumed a d_n of unity in Eq. 4.1, corresponding to plane stress loading of a perfectly plastic material, whereas a more accurate value for their material is 0.586. Accordingly, we have recalculated their toughness values here (in parenthesis).

Steady-state or maximum reported toughness after stable crack growth.